

Search for Instanton-Induced Processes
with the H1 Detector
in Deep-Inelastic Electron-Proton
Collisions at HERA

Dissertation
zur Erlangung des Doktorgrades
des Fachbereichs Physik
der Universität Hamburg

vorgelegt von
Birger Koblitz
aus Kiel

Hamburg
2002

Gutachter der Dissertation : Prof. Dr. V. Blobel
Prof. Dr. R. Klanner

Gutachter der Disputation : Prof. Dr. V. Blobel
Prof. Dr. B. Naroska

Datum der Disputation : 13.06.2002

Dekan des Fachbereichs Physik
und Vorsitzender des
Promotionsausschusses : Prof. Dr. F.-W. Büber

Abstract

The first dedicated search for QCD instanton-induced processes is presented. Deep-inelastic scattering (DIS) data collected at the electron-proton collider HERA in a kinematical range defined by the DIS variables $x > 0.001$, $0.1 < y < 0.6$ and $Q^2 < 100 \text{ GeV}^2$, and for a scattering angle of the electron of at least 156° have been analysed. Several observables characterising the instanton hadronic final state are studied and combined to a powerful discriminant with the help of an innovative range searching algorithm. By cutting on the discriminant, a potentially instanton enriched region is found in the observable phase space. Given the accuracy of the standard DIS background models, no significant excess of events in this region is found, and a model independent limit on the instanton-induced cross-section of 221 pb is calculated. A detailed study with different effective instanton sizes and distances can exclude a steep rise of the cross-section towards large instanton-sizes and small distances predicted by a naive extrapolation of instanton perturbation theory and is in accord with recent lattice calculations. Finally, the prospects of a search in the region $Q^2 > 100 \text{ GeV}^2$ are studied.

Zusammenfassung

Die Arbeit beschreibt die erste dedizierte Suche nach QCD Instanton-induzierten Prozessen. Hierzu werden Daten ausgewertet, die mittels tief-unelastischer Streuung (DIS) am Elektron-Proton Beschleuniger HERA in einem kinematischen Bereich gewonnen wurden, der durch die DIS Variablen $x > 0.001$, $0.1 < y < 0.6$ und $Q^2 < 100 \text{ GeV}^2$, sowie durch einen minimalen Streuwinkel des Elektrons von 156° gegeben ist. Verschiedene Observable, die den hadronischen Endzustand des Instanton-induzierten Prozesse charakterisieren, werden untersucht und zu einer aussagekräftigen Diskriminante mittels eines innovativen Algorithmus, der auf Bereichssuche basiert, zusammengefasst. Indem in diese Diskriminante geschnitten wird, ergibt sich eine Region im Phasenraum der Observablen, in der potentielle Instanton-induzierte Ereignisse angereichert sein sollten. Innerhalb der Unsicherheit der Modelle der normalen tief-unelastischen Streuung lässt sich kein signifikanter Überschuss an Ereignissen finden. Deshalb wird in diesem Bereich eine Obergrenze des Streuquerschnittes unabhängig von der Modellierung des Untergrundes berechnet. Sie beträgt 221 pb. Eine detaillierte Studie, bei der nach Instantonen unterschiedlicher effektiver Größe und Abstandsverteilung gesucht wird, kann jedoch zumindest das von der Instanton Störungstheorie vorhergesagte steile Anwachsen des Streuquerschnittes ausschließen, das man durch naive Extrapolation hin zu größeren Instantonen und kleineren Abständen errechnet. Dies ist in Übereinstimmung zu neueren Gitterrechnungen. Schließlich wird das Potential einer Suche bei $Q^2 > 100 \text{ GeV}^2$ herausgearbeitet.

Contents

Introduction	5
1 Instantons in QCD	7
1.1 Quantum Chromodynamics	7
1.2 Tunnelling in Quantum Mechanics	8
1.3 Instantons in Yang-Mills Theory	11
1.4 Deep-Inelastic Scattering	15
1.5 QCD Instanton-Induced Processes in ep Collisions	17
2 The HERA Accelerator and the H1 Detector	23
2.1 The HERA Storage Ring	23
2.2 The H1 Experiment	25
2.2.1 The Tracking Systems	27
2.2.2 The Calorimeters	28
2.2.3 The Luminosity System	31
2.2.4 The Triggering System	32
3 Analysis Techniques	35
3.1 Event Classification	35
3.2 Univariate Classification Methods	36
3.3 Neural Networks	37
3.4 Event Classification Based on Range Searching	40
3.4.1 The Range Searching Algorithm	42
3.4.2 Properties of Range Searching	42
3.5 Conclusions	44
4 Monte Carlo Models	46
4.1 Standard DIS Monte Carlo Models	46
4.2 QCDINS	48
4.3 Hadronization Models	49
4.4 Detector Simulation	50
5 Data Selection	52
5.1 Used Subtriggers	52
5.2 Kinematic Cuts	55
5.3 Data Quality Cuts	57

5.3.1	Selection of Run-Ranges	57
5.3.2	A Cut on the Event Vertex	57
5.3.3	The Energy Balance	58
5.3.4	Cuts on the Properties of the Scattered Electron	58
5.3.5	Track Selection	59
5.4	Description of the Data by Standard DIS-Models	59
5.4.1	Description of the Electron Distributions	59
5.4.2	Description of the Hadronic Final State	62
6	The Experimental Search	64
6.1	Hadronic Final State in Instanton-Induced Processes	64
6.2	Characteristic Instanton Variables	67
6.2.1	Reconstruction of the I-Subprocess Kinematics and the I-Band	67
6.2.2	Definition of the Characteristic Instanton Variables	71
6.2.3	Comparison of the Standard QCD Predictions with the Data	72
6.2.4	Influence of the Hadronization Model on QCDINS Events	75
6.3	Search Strategy	76
6.4	Systematic Uncertainties	77
6.5	Combinatorial Cuts Based Search	83
6.5.1	Results of the Cut-Based Method	83
6.6	A Discriminant Search	86
6.6.1	Definition of the Discriminant	86
6.6.2	Results of the Discriminant Search	88
6.6.3	Observable Distributions of the I-Enriched Sample	89
6.6.4	A Close-Up of the Discriminant	93
6.6.5	Examples of Selected Events	95
6.7	Cross-Section Exclusion Limits	96
6.7.1	Cross-Section Limits in the Fiducial Region	97
6.7.2	Instanton Model Independent Cross-Section Limits	98
6.7.3	Confrontation With Lattice Data	100
6.8	Discussion and Summary	101
7	Reconstruction of Instanton Kinematics	103
7.1	Reconstruction of x' and Q'^2	103
7.2	Improvements in Reconstruction	105
8	Outlook on Searching for Instantons at High Q^2	109
8.1	Screening of Suitable Variables	109
8.1.1	Definition of Observables	110
8.1.2	Screening of the Variables	111
8.2	Results	114
8.3	Study of Discriminant and Comparison with NNs	116
8.4	Conclusions	118
9	Conclusions and Outlook	120

A Implementation of the Range Searching Algorithm	122
B Exclusions Limits	126
Bibliography	128
List of Figures	134
List of Tables	136
Acknowledgements	137

Introduction

With the beginning of the 20th century the understanding of nature was revolutionised by two new theories, the theory of relativity and quantum mechanics. While quantum mechanics introduced the principle of quantised action, the theory of relativity is based on the principle that every inertial system is equivalent and that the speed of light is the same, independent of the reference frame. By applying quantum mechanics and the theory of relativity to the concept of fields, quantum field theories were introduced, which brought along an entirely new idea. Since only the amplitude of the fields but not the phase is observable, they can have an arbitrary gauge. In fact, quantum field theories allow every observer to choose his own local gauge of the quantum fields, and establish invariance under local gauge transformations as a new fundamental principle.

Quantum field theories describe the interaction of force fields with matter, where the force fields are simply introduced by the requirement of invariance under certain gauge transformations. The most successful quantum field theory is without doubt Quantum Electrodynamics (QED), where the gauge field is the electromagnetic field. QED describes electromagnetism as well as the interaction of matter with light. Until today no discrepancy between measurements and theoretical predictions have been found, despite impressive experimental precision.

In the atomic nucleus, a different fundamental force is important. Quantum Chromodynamics (QCD) is the field theory which describes the formation of nucleons out of quarks and thus also the formation of the atomic core. QCD is different from QED in that the strength of the interaction of particles increases with the distance, binding nucleons tightly together and overcoming the repulsion of the electromagnetic force among the protons in the nucleus. In contrast to the photon, the gauge bosons (called gluons) in QCD carry a (colour) charge due to the *non-Abelian* nature of the gauge transformations. This induces new kinds of self-interactions among the gluons, leading to a *confinement* of coloured objects at large distances and *asymptotic freedom* at small distances. The non-Abelian structure of QCD has been indirectly established by measuring the decrease of the coupling constant α_s with increasing energy scale, which can only be explained by triple-gluon interactions.

Non-Abelian field theories also induce a complex topological structure of the vacuum. Two vacuum ground states can be energetically equivalent but topologically different. Topologically different means, that it is not possible to continuously transform one of the ground states into the other by applying a series of infinitesimal gauge transformation. In particular, it is not possible to describe the transition of one of the ground states into another with the help of perturbative fluctuations of the gauge field.

Instantons are tunnelling processes from one vacuum state into another topologically different one. Instantons have not yet been experimentally observed and a search for instanton-

induced processes is the objective of this thesis.

A unique chance to observe instanton transitions in deep-inelastic scattering of electrons on protons, is made possible by the HERA electron-proton accelerator. Instantons should induce additional scattering processes, different from those induced by QED and normal QCD. However, as will be shown, only a tiny fraction of the deep-inelastic scattering events are expected to be instanton-induced. Therefore, it is necessary to establish sophisticated discrimination methods between instanton-induced processes and standard deep-inelastic scattering processes. Developing and studying such techniques is therefore an important aim of the thesis.

In the first chapter, the theoretical foundations will be given. After a brief introduction of QCD, the phenomenon of instantons is explained and deep-inelastic scattering is described as a means to observe instanton-induced processes.

The observation of deep-inelastic scattering events of electrons on protons is made possible by a unique machine, the HERA accelerator colliding highly energetic electrons with protons. The H1 experiment is one of two detectors observing these collisions and was used to collect the data for this analysis. The HERA machine and the H1 detector will be described in chapter 2.

Developing powerful means to discriminate between instanton-induced event and standard deep-inelastic scattering events is necessary to perform a search for instantons. The theory of the classification of events is explained in chapter 3 along with a detailed description of the classification methods employed in this thesis. This includes an algorithm based on range searching, whose eligibility for the classification of events in high energy physics will be studied in depth. After an examination of the basic properties of this algorithm in chapter 3, the algorithm will not only be used for classification, but also to screen a large number of observables to find the ones best suited for classification purposes (chapter 8) and to find a certain kind of jet assuming a model in chapter 7.

The deep-inelastic scattering events recorded in the H1 detector will be classified by comparing them to models of standard deep-inelastic background events and instanton-induced events. The models are provided by so-called “Monte Carlo generators”, computer programs to simulate the complete quantum mechanical final state of these events. The Monte Carlo generators employed in this analysis are described in chapter 4.

Chapter 5 will give details on the selection of the data which has been collected by the H1 detector in the years 1996 and 1997. The experimental search for instanton-induced events is described in chapter 6. Since no significant evidence for instanton-induced events can be established with the given data, exclusion limits on the cross-section of instanton-induced processes be derived. Finally, an outlook on a search for instantons in a different kinematical range is finally given in chapter 8.

Chapter 1

Instantons in QCD

Quantum Chromodynamics (QCD) is the gauge theory of the strong interaction, the force responsible for the formation of hadrons. The strong interaction is also the force overcoming the Coulomb repulsion of the positively charged protons in the atomic nuclei. Understanding this fundamental force therefore provides basic insight into the formation of matter.

The main characteristic of QCD is that it is a *non-Abelian* gauge theory, which leads to a force of constant strength at long distances. Strongly interacting particles are asymptotically free at short distances (the coupling constant α_s being small) and confined at large distances (the force being constant, while the potential increases linearly). The non-Abelian nature of the interaction also induces, through non-perturbative vacuum fluctuations, a complicated topology of the vacuum. An important manifestation of this complex topological structure of the theory are instantons, which are tunnelling transitions between two topologically different vacuum states.

In the following, QCD is introduced as a non-Abelian gauge theory and some of the properties of QCD are described. The phenomenon of tunnelling in quantum mechanics is then explained in a semi-classical way which allows to derive instantons as tunnelling transitions between topologically different ground states of QCD. Finally, an overview of deep-inelastic scattering (DIS), the scattering of electrons on protons at large momentum transfers, is given and the production mechanism of instanton-induced processes in DIS is discussed¹.

1.1 Quantum Chromodynamics

Quantum Chromodynamics is a field theory which has three fundamental charges in contrast to quantum electrodynamics (QED) which has only one charge. Due to the fact that only certain combinations of all of the three charges give a zero charge, the charge in QCD is also named “colour”, hence the name chromodynamics. In the Standard Model the six different quark flavours (u, d, s, c, b, t) carry the fundamental charges and there are eight charged gauge bosons called “gluons”. The gauge group of the theory, the group of gauge transformations under which the Lagrangian of the theory has to be locally gauge invariant, is the non-Abelian group $SU(3)$. Non-Abelian gauge theories have been first proposed by C. N. Yang

¹An introduction to field theories, QCD and DIS can be found for example in [1].

and R. Mills [2], they are therefore also called *Yang-Mills theories*. The Lagrangian of QCD is of the form

$$L = -\frac{1}{4g^2}(G_{\mu\nu}^a)^2 + \bar{\psi}(i\gamma^\mu D_\mu)\psi - m\bar{\psi}\psi \quad , \quad (1.1)$$

where ψ is a generic fermion field and $G_{\mu\nu}^a$ the field strength tensor of the gluon field

$$G_{\mu\nu}^a = \partial_\mu A_\nu^a - \partial_\nu A_\mu^a + f^{abc}A_\mu^b A_\nu^c \quad , \quad (1.2)$$

which involves derivatives of the vector potentials A_μ^a . The index a thereby denotes the colour-index (1, ..., 8) of the gluon field. f^{abc} are the structure constants of the gauge group, defined by $[t^a, t^b] = if^{abc}t^c$ with t^a being the hermitian generators of the group. It is the fact that the generators of the group do not commute, that makes the theory non-Abelian. In Abelian theories, the term proportional to f^{abc} in (1.2) is absent.

The Lagrangian (1.1) is invariant under gauge transformations mediated by unitary matrices $V(x)$ as the representation of the gauge group of the form

$$\psi(x) \rightarrow V(x)\psi(x) \quad A_\mu^a(x)t^a \rightarrow V(x) \left(A_\mu^a(x)t^a + \frac{i}{g}\partial_\mu \right) V^\dagger(x) \quad , \quad (1.3)$$

where the x dependence of $V(x)$ makes the transformations local. The transformations can be written in infinitesimal form using the generators t^a of the group:

$$V(x) = \mathbf{1} + i\alpha^a(x)t^a + \mathcal{O}(\alpha^2) \quad . \quad (1.4)$$

α^a is a vector of eight parameters of the gauge transformation. Requiring the invariance of the Lagrangian under gauge transformations (1.3) entails the form of the covariant derivative in the Lagrangian:

$$D_\mu = \partial_\mu - igA_\mu^a t^a \quad . \quad (1.5)$$

It is noteworthy, that it is not possible to define a locally gauge invariant theory without the gauge fields A_μ^a .

The term quadratic in A_μ^a in the definition of the gluon field strength tensor (1.2) has an additional consequence. It induces terms proportional to the third and fourth power of the vector potential in the Lagrangian. In the equations of motion, which are derived from the Lagrangian by varying the fields and their derivatives, these terms, which are not present in QED, also show up, leading to a self-interaction of the gluon field (the quadratic term in A_μ is the kinetic energy term of the field, and is also present in QED). The resulting interaction vertices are shown in figure 1.1. In addition to the interactions between fermions and bosons, QCD has also three and four gluon vertices which are absent in QED. This self-interaction of the gluon field is responsible for an anti-screening of colour charges which leads to an increasing strength of the colour force with growing distance, called ‘‘confinement’’, which is responsible for tightly binding the quarks in hadrons together.

1.2 Tunnelling in Quantum Mechanics

In this section, instantons are introduced as tunnelling transitions of finite action. The double well potential is used as a simple example to study these processes.

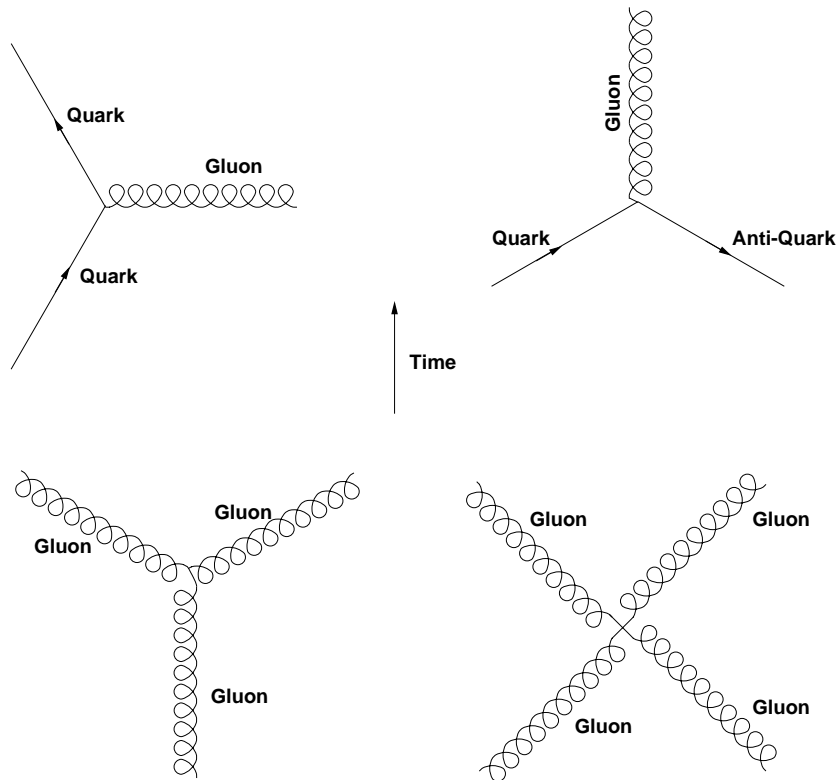


Figure 1.1: Feynman diagrams of the vertices appearing in QCD. In addition to the two vertices with fermions and bosons which are also present in QED, in QCD also the three and four gluon vertices exist, leading to a self-interaction of the gluon field.

Tunnelling processes are processes which are forbidden in classical physics because they represent solutions to the equations of motion with negative kinetic energy. Nevertheless, it is possible to calculate these solutions in a classical manner if one makes the transition from real time t to imaginary (Euclidean) time $\tau = it$. Under this transformation the action S becomes $S \rightarrow iS_E$. The special role of the classical tunnelling path becomes clear when applying the Feynman path integral formalism, where every path is weighted with the exponential $e^{iS[x(t)]} \rightarrow e^{-S_E[x(\tau)]}$. Although any path is in principle allowed in quantum mechanics, the dominant contribution comes from paths, which maximise the weight factor $\exp(-S_E[x(\tau)])$ and thereby minimise the classical action.

Let us consider a particle with spin zero and mass $m = 1$ in a one-dimensional double well potential (example taken from [3])

$$V(x) = \lambda(x^2 - x_0^2)^2 \quad (1.6)$$

with minima at $x = \pm x_0$, which represent the two “classical vacua” of the system depicted in Figure 1.2 (λ is a measure for the height of the potential barrier). The classical solution with minimal energy $E = 0$ of this problem is that the particle either resides at $+x_0$ or $-x_0$, i.e.

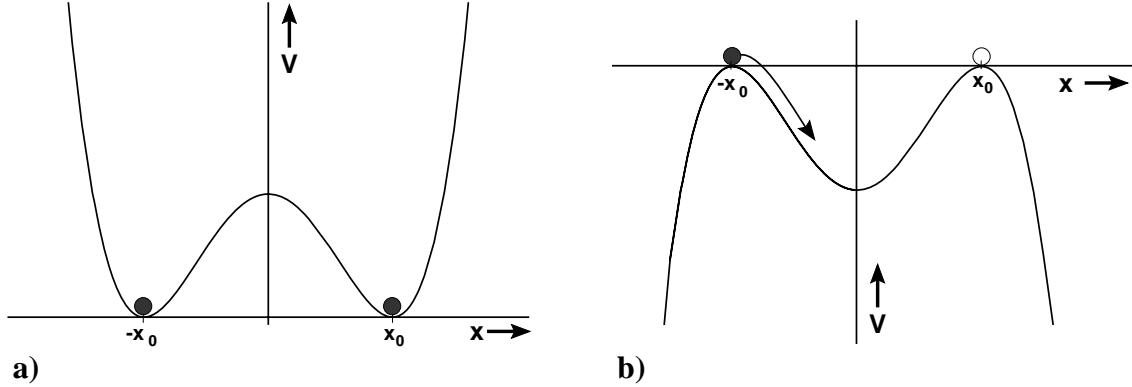


Figure 1.2: In a double well potential (a) classical particles reside in either of the two minima at $\pm x_0$. Transition to imaginary time (b) $\tau = it$ transforms the potential to the double hump potential depicted at the right, where the solution with minimal energy $E = 0$ is a particle moving from one of the humps to the other. This is the so-called “instanton solution”.

the ground state is doubly degenerated. Quantising around any of these two minima does not give the correct result for the state $|x\rangle$ in space in quantum mechanics, instead the solution is a superposition of these two states $| -x_0\rangle$ and $| +x_0\rangle$

$$|x\rangle = \frac{1}{\sqrt{2}}(|-x_0\rangle + |x_0\rangle) \quad . \quad (1.7)$$

Thus the symmetry of the system is restored by the tunnelling through the potential barrier and the expectation value of the particle location in the ground state is $\langle x \rangle = 0$.

We will describe the tunnelling process classically by a transition to imaginary time $t \rightarrow it = \tau$. The Hamiltonian of the system

$$H(x, \tau) = E = -\frac{1}{2} \left(\frac{dx}{d\tau} \right)^2 + V(x) \quad (1.8)$$

then changes the relative signs of the kinetic energy term and the potential energy term, which can be seen as a mirroring of the potential from $V(x)$ to $-V(x)$:

$$-E = \frac{1}{2} \left(\frac{dx}{d\tau} \right)^2 - V(x) \quad , \quad (1.9)$$

see Figure 1.2. We now want to find the so-called “instanton solutions” with minimal energy $E = 0$. Transforming (1.9) and inserting (1.6) one gets the differential equation

$$\frac{dx}{\pm \sqrt{2\lambda} (x^2 - x_0^2)} = d\tau \quad (1.10)$$

with solutions

$$x(\tau) = \pm x_0 \tanh \left(\sqrt{2\lambda} [\tau - \tau_0] x_0 \right) \quad . \quad (1.11)$$

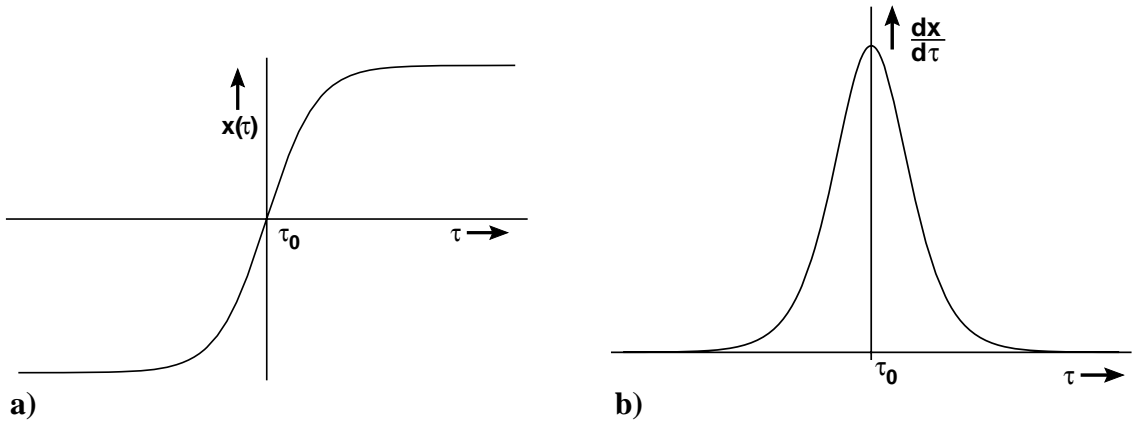


Figure 1.3: The instanton solution in imaginary time. In a) the instanton solution (1.11) is shown. b) shows the derivative $\frac{dx}{d\tau}$ of the process, illustrating the localisation in time.

The above solutions are called instantons (I), or anti-instantons in case of the minus sign. The arbitrary parameter τ_0 is the centre of the instanton. The instanton solution in imaginary time is depicted in figure 1.3.

All integrals that appear are finite, therefore, the action of the instanton solution can be calculated (recall that $V(x) = \frac{1}{2} \frac{dx}{d\tau}$):

$$S_0 = S[x(\tau)] = \int_{-\infty}^{+\infty} d\tau \left(\frac{dx}{d\tau} \right)^2 = \frac{4}{3} x_0^3 \sqrt{2\lambda} \quad . \quad (1.12)$$

Since the action is finite, non-trivial solutions have been found with a finite transition probability. The action does not depend on the arbitrary parameter τ_0 , so that the action is independent of the centre of the instanton. By this, the symmetry of the original problem is restored. In the following, the above thoughts are extended to Yang-Mills theories to generalise the idea of instantons.

1.3 Instantons in Yang-Mills Theory

In this section, the methods developed in the previous section are applied to non-Abelian gauge theories. The aim is to introduce instantons as solutions of finite action of the equations of motion in Euclidean Yang-Mills theory and to derive some of the basic properties of instantons like the behaviour of the cross-section or their size. The derivation follows closely the introductions to instanton theory found in [3, 4, 5].

The Lagrangian of a Yang-Mills theory in Euclidean space can be written as (for the details of the transition from Minkowski space to Euclidean space see [3])

$$L = \frac{1}{4g^2} G_{\mu\nu}^a G_{\mu\nu}^a \quad , \quad (1.13)$$

where fermion fields have been neglected and $G_{\mu\nu}^a$ is the field strength tensor of the gluon

field with coupling constant g :

$$G_{\mu\nu}^a = \partial_\mu A_\nu^a - \partial_\nu A_\mu^a + f^{abc} A_\mu^b A_\nu^c \quad . \quad (1.14)$$

Here f^{abc} are the structure constants of the gauge group ($SU(2)$ is chosen for simplicity in the following discussion), and A_μ^a is the gluon field of colour $a = (1, \dots, 3)$.

The classical action of be rewritten as

$$S = \int d^4x L = \frac{1}{4g^2} \int d^4x G_{\mu\nu}^a G_{\mu\nu}^a \quad (1.15)$$

$$= \frac{1}{8g^2} \int d^4x ((G_{\mu\nu}^a \pm \tilde{G}_{\mu\nu}^a)^2 \mp 2G_{\mu\nu}^a \tilde{G}_{\mu\nu}^a) \quad (1.16)$$

$$= \left(\frac{1}{8g^2} \int d^4x (G_{\mu\nu}^a \pm \tilde{G}_{\mu\nu}^a)^2 \right) \mp \frac{8\pi^2}{g^2} Q \quad , \quad (1.17)$$

where the topological charge (also called Pontryagin-number in mathematical literature or Chern-Simons number N_{CS} in field theory)

$$Q = N_{CS} = \frac{1}{32\pi^2} \int d^4x G_{\mu\nu}^a \tilde{G}_{\mu\nu}^a \quad (1.18)$$

has been defined using the dual tensor $\tilde{G}_{\mu\nu}^a$ to $G_{\mu\nu}^a$:

$$\tilde{G}_{\mu\nu}^a = \frac{1}{2} \varepsilon_{\mu\nu\alpha\beta} G_{\alpha\beta}^a \quad .$$

$\varepsilon_{\mu\nu\alpha\beta}$ is the totally anti-symmetric Levi-Civita tensor. The identity $\tilde{G}_{\mu\nu}^a \tilde{G}_{\mu\nu}^a = G_{\mu\nu}^a G_{\mu\nu}^a$ can be obtained with the help of the contraction $\varepsilon_{\alpha\beta\mu\nu} \varepsilon_{\alpha\beta\rho\sigma} = -(\delta_\rho^\mu \delta_\sigma^\nu - \delta_\sigma^\mu \delta_\rho^\nu)$ and the anti-symmetry of $G_{\mu\nu}^a$.

The finiteness of the action (1.15) poses certain restrictions on the fields as is explained in [6]. Since $G_{\mu\nu}^a G_{\mu\nu}^a$ is positive definite, on a large sphere with radius $|x| = R \rightarrow \infty$ the gluon field strength tensor must vanish

$$G_{\mu\nu}^a(|x| = R) \rightarrow 0, \quad \text{faster than } R^{-3}, \quad (1.19)$$

which can be fulfilled, if A_μ^a is a pure gauge field on large spheres:

$$A_\mu^a T^a \rightarrow iU(x) \partial_\mu U^{-1}(x), \quad \text{for } R \rightarrow \infty. \quad (1.20)$$

Here the generators of the gauge group T^a have been introduced, which are in the case of $SU(2)$ the Pauli spin matrices σ^a . The matrices $U(x)$ are elements of this group: $U(x) \in SU(2)$.

To find the tunnelling paths with minimum Euclidean action, it is useful to exploit the fact that the topological charge Q is a total derivative, which allows to apply the theorem of Gauss:

$$Q = \frac{1}{32\pi^2} \int d^4x G_{\mu\nu}^a \tilde{G}_{\mu\nu}^a = \int d^4x \partial_\mu K_\mu^a = \oint d\sigma_\mu K_\mu^a \quad (1.21)$$

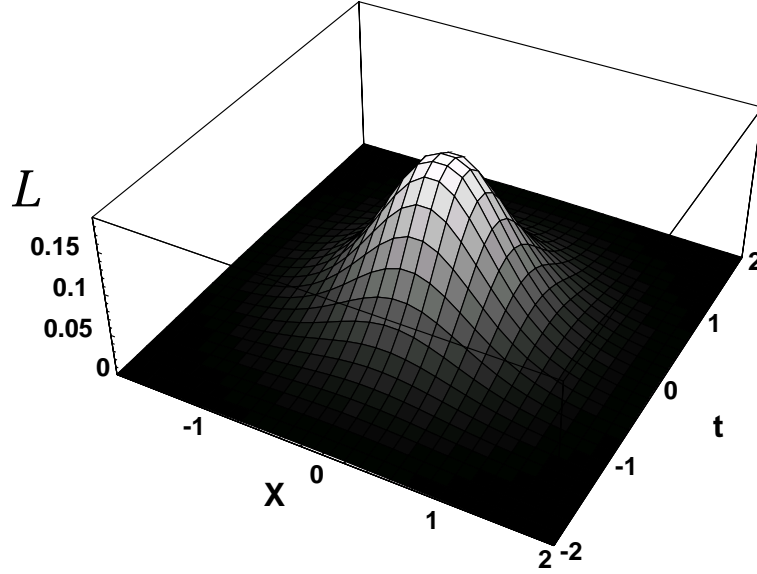


Figure 1.4: The Lagrange density of the instanton solution in 1+1 dimensions. The instanton is localised in space and time.

with the topological Chern-Simons current

$$K_\mu^a = \frac{1}{16\pi^2} \varepsilon_{\mu\alpha\beta\gamma} \left(A_\alpha^a \partial_\beta A_\gamma^a + \frac{1}{3} f^{abc} A_\alpha^a A_\beta^b A_\gamma^c \right) . \quad (1.22)$$

Therefore, Q only depends on the properties of the fields on the sphere with $R \rightarrow \infty$. Inserting $A_\mu = iU\partial_\mu U^{-1}$ into (1.22) one finds that Q is an integer number. Using this, minimal solutions of (1.15) have to fulfill the (anti-) self-duality relation

$$G_{\mu\nu}^a = \pm \tilde{G}_{\mu\nu}^a , \quad (1.23)$$

which leads to minima of the action of $S = \frac{8\pi^2}{g^2} |Q|$.

How do explicit solutions with minimum action look like? Using the special gauge transformation $U = ix_\mu \sigma_\mu$ as an ansatz with $\sigma = (\vec{\sigma}, -i)$, $\vec{\sigma}$ again being the Pauli spin matrices, one finds (by inserting into (1.20)) $A_\mu^a = 2\eta_{a\mu\nu} x_\nu / x^2$, where the 't Hooft symbol

$$\eta_{a\mu\nu} = \begin{cases} \varepsilon_{a\mu\nu} & \mu, \nu=1, 2, 3, \\ \delta_{a\mu} & \nu = 4, \\ -\delta_{a\nu} & \mu = 4, \\ 0 & \text{otherwise} \end{cases} \quad (1.24)$$

was used. One can also define $\bar{\eta}_{a\mu\nu}$ where the two middle equations change sign. This ansatz fulfills the boundary conditions (1.19). Extending it by multiplying an arbitrary function $f(x)$, with $f(x) \rightarrow 1$ for $x^2 \rightarrow \infty$, and inserting into the self-duality relation (1.23) yields the

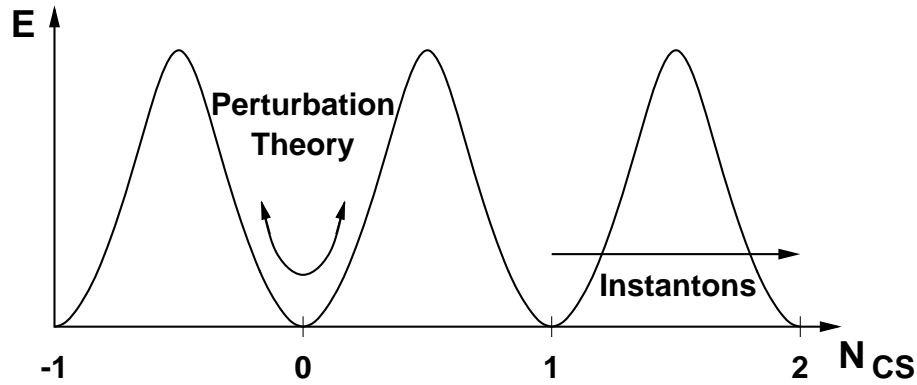


Figure 1.5: The topology of the QCD vacuum is depicted by the energy density of the gauge field as a function of the Chern-Simons number N_{CS} . At $N_{CS} = 0$ the field identically vanishes, while at the other integer values of N_{CS} the field is pure gauge. Perturbation theory makes field configurations accessible which are small changes of the vacuum field at $N_{CS} = 0$, while other minima are not accessible by continuous transformation of the field, but only through tunnelling of instantons.

solution $f(x) = x^2/(x^2 + \rho^2)$, which finally gives the so-called “BPST instanton” solution, named after the four authors who first derived it in [7]:

$$A_\mu^a(x) = 2 \frac{\eta_{a\mu\nu} x_\nu}{x^2 + \rho^2} . \quad (1.25)$$

The arbitrary parameter ρ characterises the size of the instanton. In addition, the classical instanton solution has further degrees of freedom. In $SU(2)$ they are the instanton position in space and three parameters which determine the colour orientation of the instanton. $SU(3)$ instantons can be constructed by embedding the $SU(2)$ solution, since $SU(2)$ is a subgroup of $SU(3)$, and have additional free parameters.

Inserting the instanton solution (1.25) into the definition of the field strength tensor (1.14) and $G_{\mu\nu}^a$ into the action (1.13), one immediately sees that

$$L \sim \frac{\rho^4}{(x^2 + \rho^2)^4} . \quad (1.26)$$

In Figure 1.4 the Lagrange density is shown in $1 + 1$ dimensions, which falls off like $1/x^8$ and clearly localises the phenomenon in space and time.

A more intuitive understanding of instantons is given in figure 1.5, where the energy density of the vacuum is shown as a function of the Chern-Simons number N_{CS} . While perturbation theory describes variations around the local minima, instantons tunnel from one local minimum to another. Clearly, an experimental discovery of instanton-induced processes would enhance our understanding of field theories significantly.

Another aspect of instanton-induced processes is that they violate quantum numbers which are conserved in perturbative processes. In the case of quantum flavourdynamics

(QFD), the theory of the weak interaction, the baryon (B) plus lepton (L) number conservation is violated due to electroweak instantons (W), according to the selection rule

$$\Delta L_{e,\mu,\tau} = \frac{1}{3}\Delta B = -\Delta N_{CS}[W] \quad , \quad (1.27)$$

from which

$$\Delta(B+L) = -6\Delta N_{CS}[W] \quad , \text{ while } \Delta(B-L) = 0 \quad (1.28)$$

follows. In analogy, QCD instantons (G) induce a violation of chirality (the difference of the number of right- and left-handed fermions: $\chi = \#(f_R + \bar{f}_R) - \#(f_L + \bar{f}_L)$) conservation for every quark flavour [8]:

$$\Delta\chi_{u,d,s,\dots} = 2\Delta N_{CS}[G] \quad . \quad (1.29)$$

1.4 Deep-Inelastic Scattering

When colliding highly energetic leptons with nucleons, the momentum transfer from the lepton to the constituents of the nucleon can become so large, that the nucleon fragments. These events are called ‘‘Deep-Inelastic Scattering’’ (DIS) events. At HERA, electrons or positrons collide with protons:

$$ep \rightarrow eX \quad (1.30)$$

A Feynman graph of such an event is shown in figure 1.6. A virtual photon γ^* with four-momentum q is exchanged between the electron with four-momentum k and a quark (four-momentum p) within the proton with four-momentum P . In addition to the photon, also a Z^0 -boson can be exchanged (a weak ‘‘neutral current’’ event). In ‘‘charged current’’ events a charged weak gauge boson (W^\pm) is exchanged. In this case the electron turns into a neutrino, which cannot be measured in the detector. These events are not studied in the analysis. Deep-inelastic scattering events where a Z^0 is exchanged do also not play a role in this analysis, because the analysis is conducted at relatively low values of $Q^2 = -q^2$ (compared to the Z^0 mass).

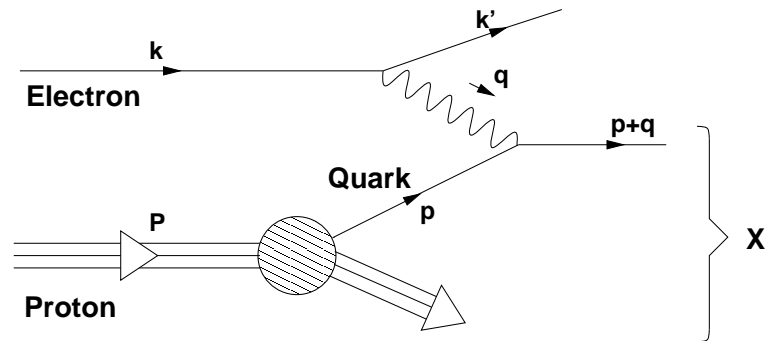


Figure 1.6: Feynman diagram of deep-inelastic scattering, where an electron scatters off a proton which breaks up into hadrons X .

The kinematic properties of the process depicted in figure 1.6 can be described by the following quantities:

Squared Centre-of-Mass Energy s

$$s = (k + P)^2 = m_e^2 + 4E_e E_p + M_p^2 \approx 4E_e E_p \quad (1.31)$$

At HERA where electrons with a beam energy of $E_e = 27.5 \text{ GeV}$ collide on protons with an energy of $E_p = 820 \text{ GeV}$, the centre-of-mass energy is $s = 90200 \text{ GeV}^2$.

Four-Momentum Transfer Squared Q^2

$$Q^2 := -q^2 = -(k' - k)^2 \quad (1.32)$$

Q^2 is a measure for the resolution of the photon, probing the constituents of the proton.

Bjorken Scaling Variable x

$$x := \frac{Q^2}{2P \cdot q} \quad (1.33)$$

In the Quark-Parton Model (QPM, see figure 1.7), where the proton is assumed to consist only out of three non-interacting quarks, x is the momentum fraction of the constituent quark (with respect to the proton) which is being hit by the photon: $p = xP$.

Inelasticity y

$$y := \frac{q \cdot P}{k \cdot P} \quad (1.34)$$

The inelasticity y can be interpreted as the relative momentum transfer from the electron to the hadronic system in the proton rest frame. y is also directly correlated with the angle of the scattered electron θ_e in the laboratory frame, where y can be expressed by

$$y = 1 - \frac{E'_e}{2E_e} (1 - \cos \theta_e) \quad (1.35)$$

In this relation, E'_e is the energy and θ_e the angle of the scattered electron.

Only two of the kinematic variables are independent, because of energy and momentum conservation. The kinematics of the collision can therefore entirely be described by the polar angle and energy of the scattered electron. In particular, the relation $Q^2 = sxy$ holds. Measuring any two independent kinematic variables of the scattered $e + X$ system after the collision allows to derive the complete kinematics of the collision.

At tree level and in leading order of the strong coupling constant α_s , three types of standard DIS processes can be distinguished. These are (see figure 1.7) the Quark-Parton Model (QPM) process in which the exchanged photon strikes a quark within the proton, the Boson-Gluon Fusion (BGF) process where a gluon out of the proton first splits into a $q - \bar{q}$ -pair and one of the quarks scatters on the exchanged photon, and the QCD-Compton process in which a gluon is radiated by the struck quark either in the initial or final state.

In the final state, the above processes contain either a single (QPM) or two quarks (BGF), or a quark plus a gluon (QCD-Compton) which carry a colour charge and hadronize into so-called ‘‘jets’’. Jets consist of several hadrons emitted in the direction of the parton produced

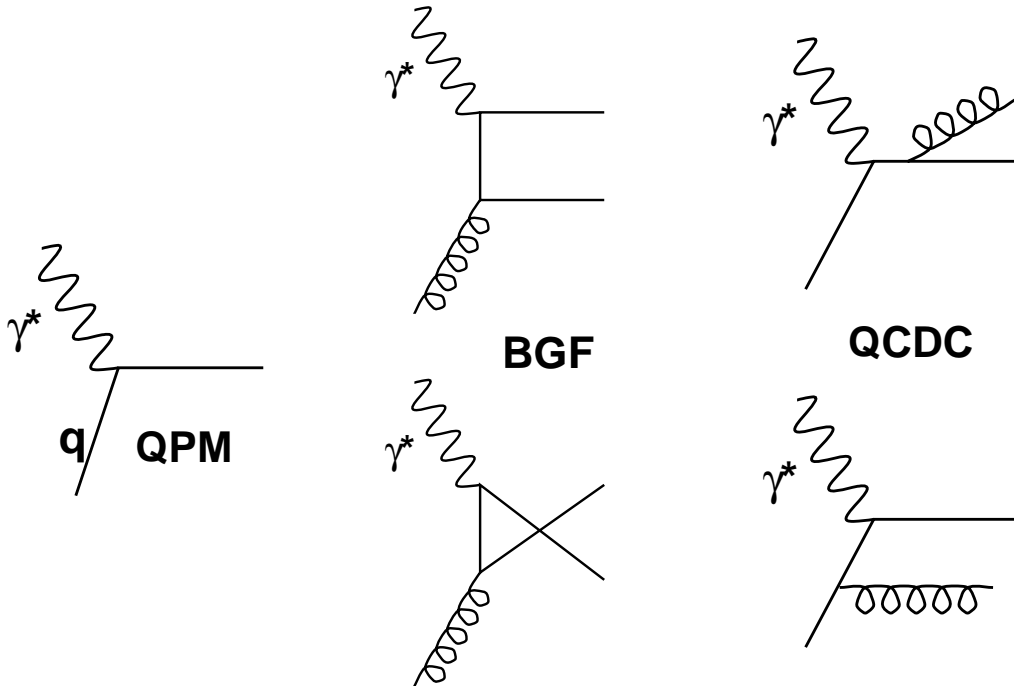


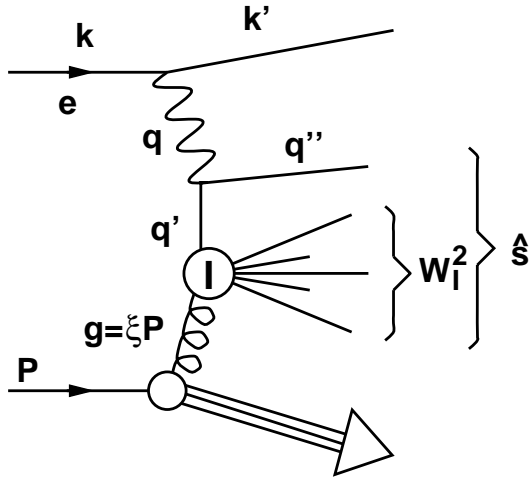
Figure 1.7: In standard deep-inelastic scattering, three different processes occur on the tree level and in leading order α_s : The Quark-Parton-Model (*QPM*) process (left), the Boson-Gluon Fusion (*BGF*) process (middle) and the QCD-Compton process (shown on the right).

in the hard subprocess. Since the partons are coloured objects, the potential energy of the connecting colour fields increases with growing distance of the partons. If the energy stored in the fields is sufficiently high, new coloured particles are created. These secondary partons can form hadrons, if their relative momenta are small enough. Due to the dynamics of the colour field, the hadrons are emitted in roughly the same directions as the partons from the hard subprocess. They form jets of hadrons.

In DIS events in electron-proton collisions also higher order processes in α_s contribute. These processes will have more quarks and gluons in the final state and can produce more jets. As we will see in the following section, they could contribute substantially to the background when looking for QCD instanton-induced processes and can only be calculated in an approximate way.

1.5 QCD Instanton-Induced Processes in ep Collisions

In addition to the standard deep-inelastic scattering events described above also instanton-induced processes can occur. Balitsky and Braun first showed that the contribution of instanton-induced processes to deep-inelastic scattering from a real gluon rises very rapidly with decreasing x [9]. The calculations were, however, restricted to large x : $x > 0.3$. Ringwald,



DIS variables:

$$Q^2 := -q^2 = -(k - k')^2$$

$$x := Q^2 / (2P \cdot q)$$

Variables of I-subprocess:

$$Q'^2 := -q'^2 = -(q - q'')^2$$

$$x' := Q'^2 / (2g \cdot q')$$

$$W_I := (q' + g)^2 = Q'^2 (1 - x') / x'$$

$$\hat{s} := (q + g)^2 = (q + \xi P)^2$$

$$\xi := x(1 + \hat{s} / Q^2)$$

Figure 1.8: Sketch of a boson-gluon fusion process with an instanton transition. A virtual photon (with four-momentum q) emitted by the incoming electron fluctuates into a $q - \bar{q}$ -pair in the instanton background, one of which (with four-momentum q') fuses with a gluon (g) out of the proton, while the other (*current-quark*) forms a hard jet. The I-subprocess is characterised by the negative four-momentum squared $Q'^2 = -q'^2$ of the incoming quark and x' , which is defined in analogy to the standard DIS variable x . ξ is the longitudinal momentum fraction of the gluon in the proton entering the instanton process.

Schrempp and collaborators showed, that deep-inelastic scattering at HERA offers a unique opportunity [10] to discover such processes induced by small instantons because of their sizeable rate [11, 12, 13] and their characteristic final state signature [10, 14, 15, 16]. Here, a brief summary of the essential ideas is given following the reviews found in [17, 18]. The dominant process is photon-gluon fusion, as sketched in figure 1.8, where a photon emitted by the incoming electron splits into a $q - \bar{q}$ -pair in the instanton background. One of these quarks (with four-momentum q') enters into the I-subprocess. The basic reaction in this subprocess is

$$\gamma^* + g \Rightarrow \sum_{\text{flavours}} (\bar{q}_R + q_R) + n_g g \quad , (I \rightarrow \bar{I}, R \rightarrow L) \quad , \quad (1.36)$$

where q_R (\bar{q}_R) denote right-handed quarks, or anti-quarks respectively. Gluons are denoted by g . In every I-induced event, one quark anti-quark pair of all n_f kinematically accessible flavours is produced². Chirality is violated by these events with $\Delta_\chi = 2n_f$. Anti-Instantons also contribute to the cross-section; they only have left-handed quarks q_L and \bar{q}_L in the final state. The quarks are emitted isotropically together with a mean of $\langle n_g \rangle \approx \mathcal{O}(1/\alpha_s) \approx 3$

²In principle, also heavy flavours contribute whenever very small instantons are probed. In general, the quark must appear approximately massless on the scale of the dominant I-size $\rho^*(Q', x')$, i.e. $\rho^* m_q \ll 1$. In the HERA kinematical regime, the rate is dominated by $\rho^* \approx 0.35$ fm, where only u, d and s quarks appear massless ($n_f = 3$). It was checked, that the predicted final state signature does not change significantly, if heavy quarks are included.

gluons. The quark that is generated in the fluctuation of the photon and does not enter into the I-subprocess also hadronizes and forms a relatively hard jet.

The cross-section of instanton-induced processes in unpolarised ep -collisions can be calculated in I-perturbation theory [11, 12] and the differential cross-section can be written in the Bjorken-limit as the product of the differential luminosity $L_{q'g}^{(I)}$, accounting for the number of $q'g$ collisions per eP -collision and the total cross-section $\sigma_{q'g}^{(I)}$:

$$\frac{d\sigma_{eP}^{(I)}}{dx' dQ'^2} \simeq \frac{dL_{q'g}^{(I)}}{dx' dQ'^2} \cdot \sigma_{q'g}^{(I)}(Q', x') \quad (1.37)$$

The differential luminosity $L_{q'g}^{(I)}$ can be understood as a convolution of the gluon density of the proton, the photon flux P_{γ^*} and the probability that the photon produces a quark-anti-quark pair in the background of the instanton process. $L_{q'g}^{(I)}$ has been calculated in [12].

The total instanton cross-section can be calculated by an integration over all free parameters of the instanton solution, also called ‘‘collective coordinates’’, that is the I-size (\bar{I} -size), the $I\bar{I}$ -distance and the relative $I\bar{I}$ colour orientations. The cross-section then takes the form:

$$\sigma_{q'g}^{(I)}(Q', x') = \int d\rho d\bar{\rho} \int d^4R e^{i(P+q')R} \int dU e^{-(\rho+\bar{\rho})Q'} D(\rho, \mu_r) D(\bar{\rho}, \mu_r) \dots e^{-\frac{4\pi}{\alpha_s(\mu_r)} \Omega(U, \frac{R^2}{\rho\bar{\rho}}, \frac{\rho}{\bar{\rho}})} . \quad (1.38)$$

The ellipsis denotes several parts of the integrand which are not of interest here. ρ is the instanton size, R the instanton anti-instanton distance and U is the colour orientation matrix. μ_r denotes the renormalisation scale. The function $-1 < \Omega(U, \dots) \lesssim 0$ is the $I\bar{I}$ interaction associated with a resummation of final state gluons and can be calculated with the help of the optical theorem and the $I\bar{I}$ -valley method [19].

The instanton density $D(\rho, \mu_r)$ can also be calculated perturbatively [8, 20, 21] and is given by

$$D(\rho, \mu_r) = d \left(\frac{2\pi}{\alpha_s(\mu_r)} \right)^{2N_C} e^{-\frac{2\pi}{\alpha_s(\mu_r)} \frac{(\rho\mu_r)^{\beta_0\Delta_1 - \Delta_2}}{\rho^5}} , \quad (1.39)$$

where d is a renormalisation scheme dependent constant, β_0 is the first coefficient of the QCD β -function, $\beta_0 = \frac{11}{3}N_C - \frac{2}{3}n_f$, and Δ_1 and Δ_2 are constants which depend on μ_r and are at one-loop level equal to $\Delta_1 = 1$ and $\Delta_2 = 0$. Inserting these one-loop expressions, yields $D \sim \rho^6$ for $n_f = 0$ and $N_C = 3$. $\Delta_{1,2}$ are also known at the two-loop level [21], at which the I-density is renormalisation-group invariant. Due to this power law, the integral over the instanton (anti-instanton) size generally diverges for large ρ ($\bar{\rho}$). However, for large enough Q'^2 only small instantons enter into the calculation, because of the exponential factor $e^{-(\rho+\bar{\rho})Q'}$.

Inspecting equations (1.38) and (1.39), one can see that the cross-section dependence on the coupling constant is

$$\sigma \sim \left[\frac{2\pi}{\alpha} \right]^{4N_C} e^{-\frac{4\pi}{\alpha}(\Omega+1)} , \quad (1.40)$$

which also holds for QFD ($N_C = 2$), where $\alpha = \alpha_W$ is much smaller than $\alpha = \alpha_s$ in QCD ($N_C = 3$). In order to bring the tiny instanton-induced electroweak $B + L$ violation into a

possibly measurable range, the final state emission of a huge number of W -bosons is absolutely crucial [22], i.e. $(1 + \Omega_W) \approx 0$. In QCD, however, final state gluons only provide a moderate numerical correction of the rate. Correspondingly, the predictions of the I-induced rate in QCD depends much less on the resummation of final state gauge bosons, which may be hard to control. In addition, DIS provides a scale $Q^2 \approx Q'^2 > Q_{\min}^2$ which was shown to dynamically cut off large sizes $\rho > \rho_{\max}$ (since Q'^2 and the instanton size are conjugate variables: $\rho_{\max} \sim 1/Q'$) such that the cross-section for small instanton sizes can be calculated perturbatively. In fact, the integrals in (1.38) are dominated by a unique saddle-point

$$U^* = \text{most attractive relative colour orientation} \quad (1.41)$$

$$\rho^* = \bar{\rho}^* \sim 1/Q'; \quad R^{*2} \sim 1/(P+q')^2 \quad \Rightarrow \quad \frac{R^*}{\rho^*} \sim \sqrt{\frac{x'}{1-x'}}. \quad (1.42)$$

In the following, the cross-section for I-induced processes at the HERA eP -collider is numerically evaluated [14].

To identify the ρ, R region, in which I-perturbation theory and thereby the calculated cross-section can be trusted, (1.39) and the (also perturbatively calculable) instanton distance distribution is compared to QCD lattice calculations, where the interaction of gluon fields is simulated on a discrete lattice. Figure 1.9 shows the instanton size and distance distributions, which have been simulated by the UKQCD Collaboration [13, 23] using three different lattice sizes without fermion fields (i.e. with $n_f = 0$, a so-called “quenched” calculation). Also shown is the $D \sim \rho^6$ behaviour of the perturbatively calculated density for $n_f = 0$. A fit to the data allows to define the following fiducial region [12, 16]:

$$\left. \begin{array}{l} \rho \lesssim \rho_{\max} \approx 0.35 \text{ fm} \\ \frac{R}{\rho} \gtrsim \left(\frac{R}{\rho}\right)_{\min} \approx 1.05 \end{array} \right\} \Rightarrow \left\{ \begin{array}{l} Q'^2 \geq \left(30.8 \Lambda_{\overline{\text{MS}}}^{n_f=3}\right)^2 \approx 113 \text{ GeV}^2 \\ x' \gtrsim 0.35 \end{array} \right. \quad (1.43)$$

The above transition from the lattice variables $\rho, R/\rho$ to x', Q' is done using the saddle point approximation.

The dependence of the I-subprocess cross-section on x' and Q'^2 is illustrated in figure 1.10. In the fiducial kinematical range (1.43) and with the general, experimentally motivated cuts $x > 10^{-3}$ and $0.1 < y < 0.9$ applied, the cross-section at HERA is calculated [14] to be (c.f. ref [24])

$$\sigma_{\text{HERA}}^{(I)} \approx 89_{-15}^{+18} \text{ pb} \quad , \quad (1.44)$$

with errors only referring to the uncertainty in $\Lambda_{\overline{\text{MS}}}^{(3)} = 346_{-29}^{+31} \text{ MeV}$ for three flavours, as deduced from the 1998 world average of the strong coupling constant [25].

To reduce remaining theoretical uncertainties connected to non-planar diagrams³, which have not been comprehensively calculated perturbatively, an additional cut, $Q^2 > Q_{\min}^2$, has been advocated [11, 14, 16] as the default prediction. This leads to an instanton-induced cross-section at HERA in the kinematical range $x' > 0.35$, $Q^2 \gtrsim Q_{\min}^2 \approx 113 \text{ GeV}^2$, $x > 10^{-3}$ and $0.1 < y < 0.9$ of

$$\sigma_{\text{HERA}}^{(I)} \approx 29_{-8}^{+10} \text{ pb} \quad , \quad (1.45)$$

³Non-planar diagrams have crossed outgoing quark-lines. The non-planar diagrams are necessary to preserve gauge invariance, but are negligible for large Q^2 [11]. For simplicity these processes were not included in the calculations of the cross-section.

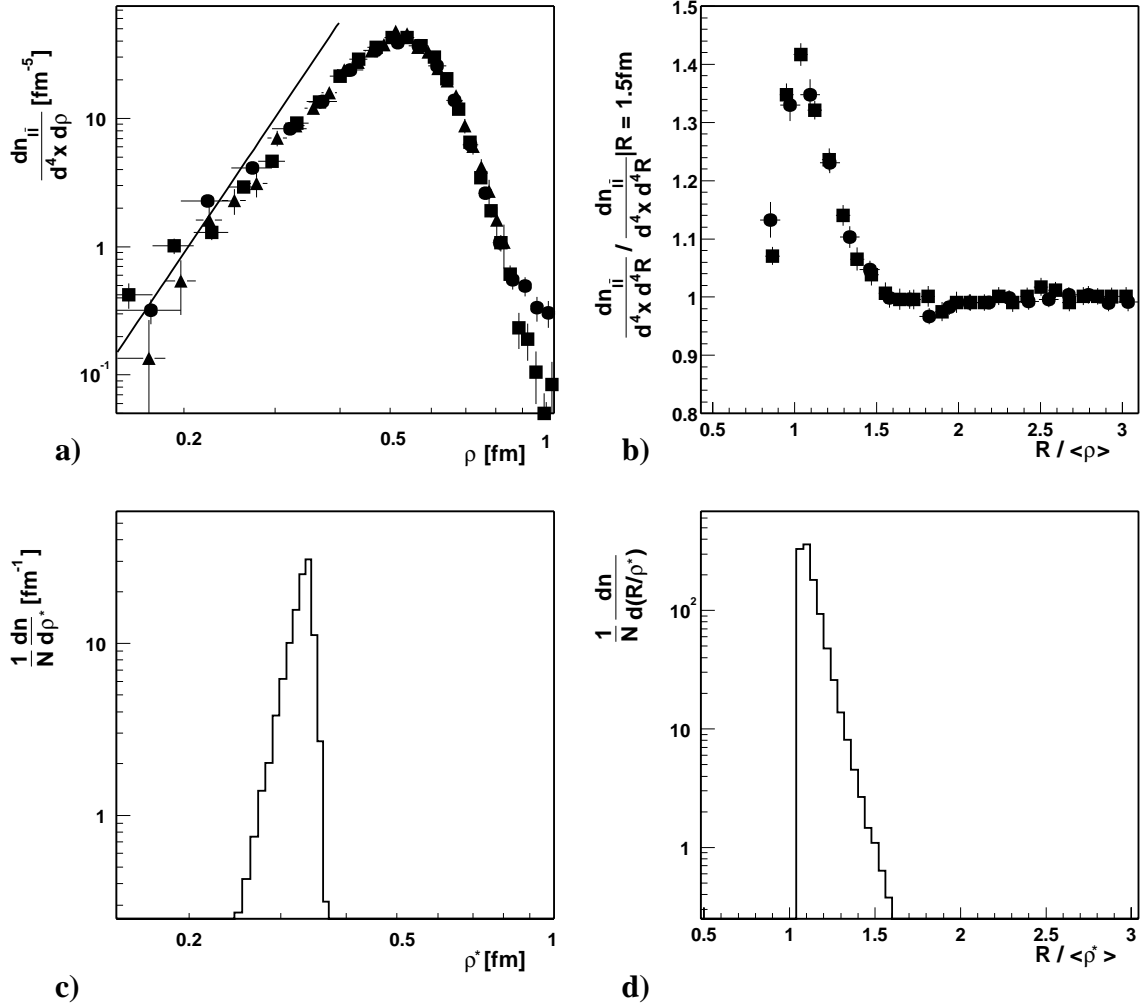


Figure 1.9: Plots a,b) show the ρ and R/ρ distributions calculated on a discrete space-time lattice for different values of the lattice-spacing by the UKQCD Collaboration [13, 23]. Also shown in a) as a straight line in this double logarithmic plot, is the perturbatively calculated $D(\rho, \mu) \sim \rho^6$ behaviour of instantons. The lower plots c,d) show the ρ^* and $R/\langle \rho^* \rangle$ instanton-distributions generated by the QCDINS Monte Carlo generator (see section 4.2) for $\rho < 0.35$ fm and $R/\rho > 1.05$. The figure was adapted from [16].

where the error is again only attributed to the uncertainty of $\Lambda_{\overline{\text{MS}}}$.

This cross-section is sizeable and makes a dedicated search for instanton-induced events at HERA promising. In the same kinematical region, however, the neutral current DIS cross-section at HERA is $\sigma_{\text{sDIS}} \approx 3000$ pb which is two orders of magnitude larger than the expected instanton cross-section. It is clear, that sophisticated selection techniques are necessary to discriminate I-induced events against such a large background which need to exploit the characteristics of the final state. An opportunity for discovering instanton-induced events was provided by the development of the QCDINS [14] Monte Carlo generator, which simulates the full hadronic final state of instanton-induced events and allows a search based on

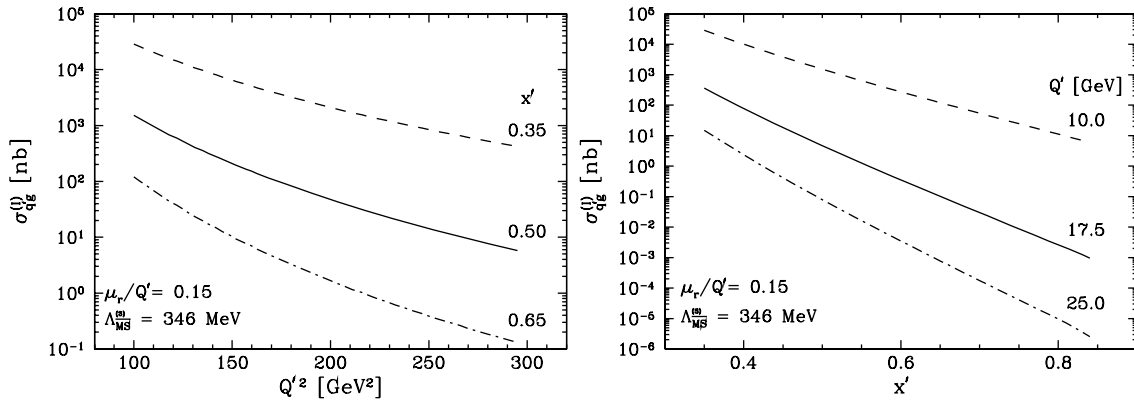


Figure 1.10: The dependence of the cross-section of the instanton subprocess in bins of x' and Q'^2 . Figures taken from [14].

a discrimination against the standard DIS background events by exploiting the characteristic features of the final state [10]:

A jet with modest E_t produced by the current quark, which is generated in the splitting of the virtual photon $\gamma^* \rightarrow q\bar{q}$ and which does not enter the instanton subprocess.

A large number of hadrons with high transverse energy E_t which are isotropic in the instanton rest-frame. Since many of the hadrons will be charged due to the conservation of isospin, a large number of charged particles are expected.

An increased production of strange hadrons due to the flavour-democracy of the instanton transition (1.36), which produces quarks of all kinematically allowed flavours. Therefore, at least one hadron containing strange quarks is produced in every event.

The chirality violation (1.29) in the instanton subprocess makes every quark produced in the instanton “decay” right-handed and the quarks produced by an anti-instanton left-handed.

The QCDINS generator and two Monte Carlo generators which model the standard DIS background events will be described in chapter 4. The sophisticated discrimination techniques which allow to distinguish between instanton-induced and background events based on the Monte Carlo simulations of the final state will be described in chapter 3, but prior to this, the HERA accelerator which provides high energetic electron and proton beams for the study of deep-inelastic eP -collisions and the H1 detector, measuring such collisions at the HERA accelerator are described in the following chapter.

Chapter 2

The HERA Accelerator and the H1 Detector

The HERA machine (German: Hadron Elektron Ring Anlage) is the first storage ring in which protons collide with electrons or positrons. After seven years of construction work, the ring consisting of two independent particle accelerators, one for protons and one for leptons, was commissioned in 1992. It is located in a tunnel 6.4 km long at the research centre DESY (German: Deutsches Elektronen Synchrotron) in Hamburg, providing four experiments with high energy particle beams. While the detectors of the H1 and ZEUS experiments investigate electron¹-proton collisions, the HERMES experiment uses the longitudinally polarised electron beam to study the spin structure of polarised nucleons in a fixed target. The HERA-B experiment on the other hand, uses the proton beam to copiously produce *B*-mesons employing a target of metal wires. Besides measuring the *B*-production cross-section, also the atomic number dependence of charmonium production is studied.

2.1 The HERA Storage Ring

The HERA machine accelerates and stores protons of up to 920 GeV and electrons of up to 27.5 GeV which then collide with a centre-of-mass energy of $\sqrt{s} = 320$ GeV. The machine is capable of accelerating positrons as well as electrons. It was operated using positrons in the years from 1994 to 1997 and from the end of 1999 until the shutdown in autumn of 2000. With positrons longer lifetimes of the beam can be reached, since for positrons fewer collisions with the remaining gas atoms in the evacuated ring take place [26]. As can be seen from figure 2.1, HERA needs several pre-accelerators to bring the energy of electrons up to the necessary injection energy of 14 GeV and of protons to 40 GeV.

Electrons and positrons are first accelerated in linear accelerators to an energy of 500 MeV. The positrons are then accumulated first in the PIA storage ring (omitted in figure 2.1) before they are injected into the DESY II synchrotron. Electrons are injected directly into DESY II. In the DESY II synchrotron bunches of $4 \cdot 10^{11}$ electrons are accelerated to a final energy of 7 GeV and then injected into the PETRA II ring. Here, 70 bunches of particles are stored and accelerated to 14 GeV before they are finally injected into the HERA machine. Since HERA

¹In the following, electron stands for both, electron or positron, unless stated otherwise.

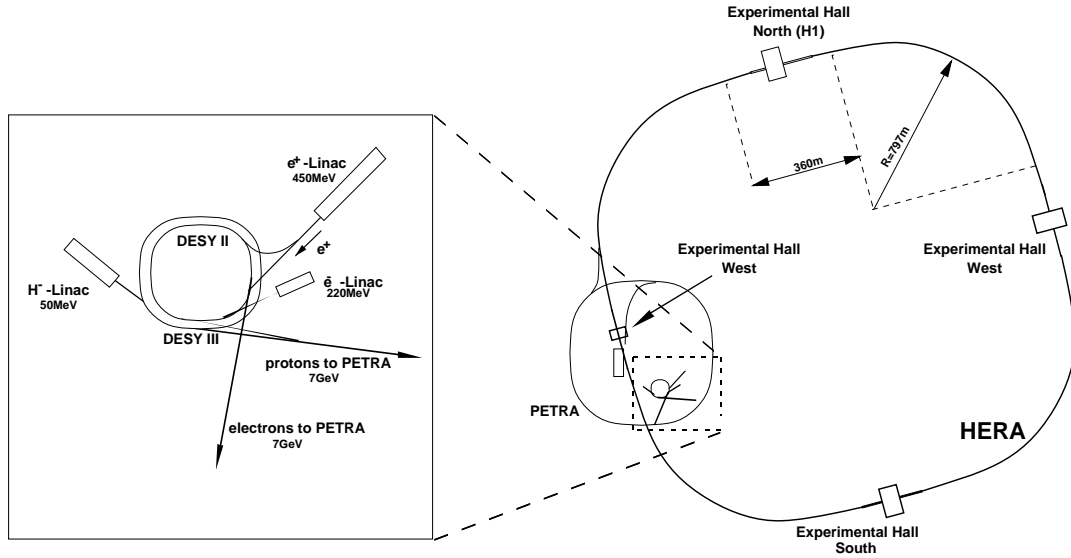


Figure 2.1: The electron-proton collider HERA and its pre-accelerators.

is capable of storing 210 bunches of both protons and electrons, it is necessary to repeat the acceleration of the particles in the PETRA ring three times.

Protons are produced using a H^- -ion linear accelerator, where the ions first acquire an energy of 50 MeV and then pass a metal foil to strip off the electrons. The produced protons are then injected into the DESY III synchrotron, where they are accelerated to 7.5 GeV and transferred to the PETRA ring. In this final step, before the injection to HERA, 70 bunches of particles are accumulated and accelerated to the injection energy of 40 GeV.

In the years 1996 and 1997, during which the data for this analysis were taken, HERA operated with positrons of an energy of 27.5 GeV and protons of 820 GeV. The limiting factor for the electron energy is the emission of synchrotron radiation. During one circulation of the ring electrons emit 150 MeV of synchrotron radiation, which adds up to a total power loss of the beam of 13 MW. This loss needs to be compensated by radio frequency klystrons. For protons, the limiting factor is the field strength of the dipole magnets that keep them on the circular trajectory. Since 1998 the currents of the super-conducting dipole magnets of the proton ring of HERA have been increased to generate a field of 4.7 T, which makes it possible to reach a proton energy of 920 GeV.

Besides the centre-of-mass energy, the luminosity L is the most important quantity of a collider. It is defined as

$$L = f \frac{N_1 N_2}{A} \quad , \quad (2.1)$$

where f is the collision frequency of the particle bunches, N_1 and N_2 the numbers of particles in the bunches and A the transverse (w.r.t. the flight direction) area of the collision zone. At HERA, where the time between two bunch crossings is 96 ns, and the sizes of the bunches are $\sigma_x \approx 280 \mu\text{m}$, $\sigma_y \approx 60 \mu\text{m}$ for the electrons and $\sigma_x \approx 180 \mu\text{m}$, $\sigma_y \approx 60 \mu\text{m}$ for the protons, the maximum luminosity in the years 1996 and 1997 was approximately $10^{31} \text{ cm}^{-2} \text{ s}^{-1}$.

The number of observed events is proportional to the luminosity integrated over the time of the observation

$$N = \sigma \int dt L \quad , \quad (2.2)$$

and σ the cross-section of the process inducing the events. In the years 1996 and 1997, HERA delivered a total integrated luminosity of $L = \int dt L = 34.1 \text{ pb}^{-1}$ [27].

2.2 The H1 Experiment

The H1 detector is a multi-purpose detector to study electron-proton collisions at the HERA collider. Being located at the northern interaction zone of the HERA ring in a depth of 20m, H1 measures $10 \cdot 12 \cdot 15 \text{ m}^3$ and weighs roughly 2800t. As can be seen in figure 2.3, it consists of several subsystems, which are arranged in layers around the interaction point. The interaction point is not in the exact centre of the detector, but shifted in the electron direction, since the centre-of-mass system of the ep -system moves along the proton direction in the laboratory frame of reference. Due to this, the detector is also built asymmetrically with respect to the proton and electron directions, while it is rather symmetric about the beam axis. A detailed description of the H1 detector can be found in [28, 29]. In the following, only those parts of the detector including the triggering system will be briefly explained, which are relevant for this analysis. The description is based on the state of the detector in the years 1996 and 1997. More recent changes are described in [30].

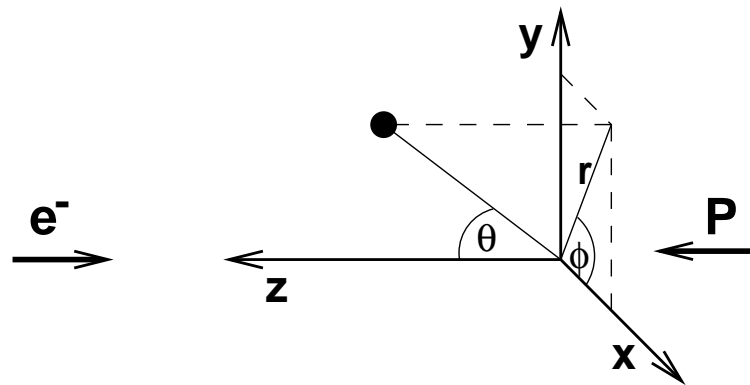


Figure 2.2: Sketch of the H1 coordinate system indicating also the electron and proton beam directions. The protons move along the positive z -axis.

In the H1 coordinate system (see sketch in figure 2.2), the protons move in the positive z -direction, while the electrons move in the opposite direction. The centre of the coordinate system approximately coincides with the interaction point within the detector. The proton direction is often referred to as the “forward” direction, since the centre-of-mass frame of the ep -system moves in this direction in the laboratory frame. In addition to the Cartesian coordinates, also cylinder coordinates (z, r, ϕ) are commonly used.

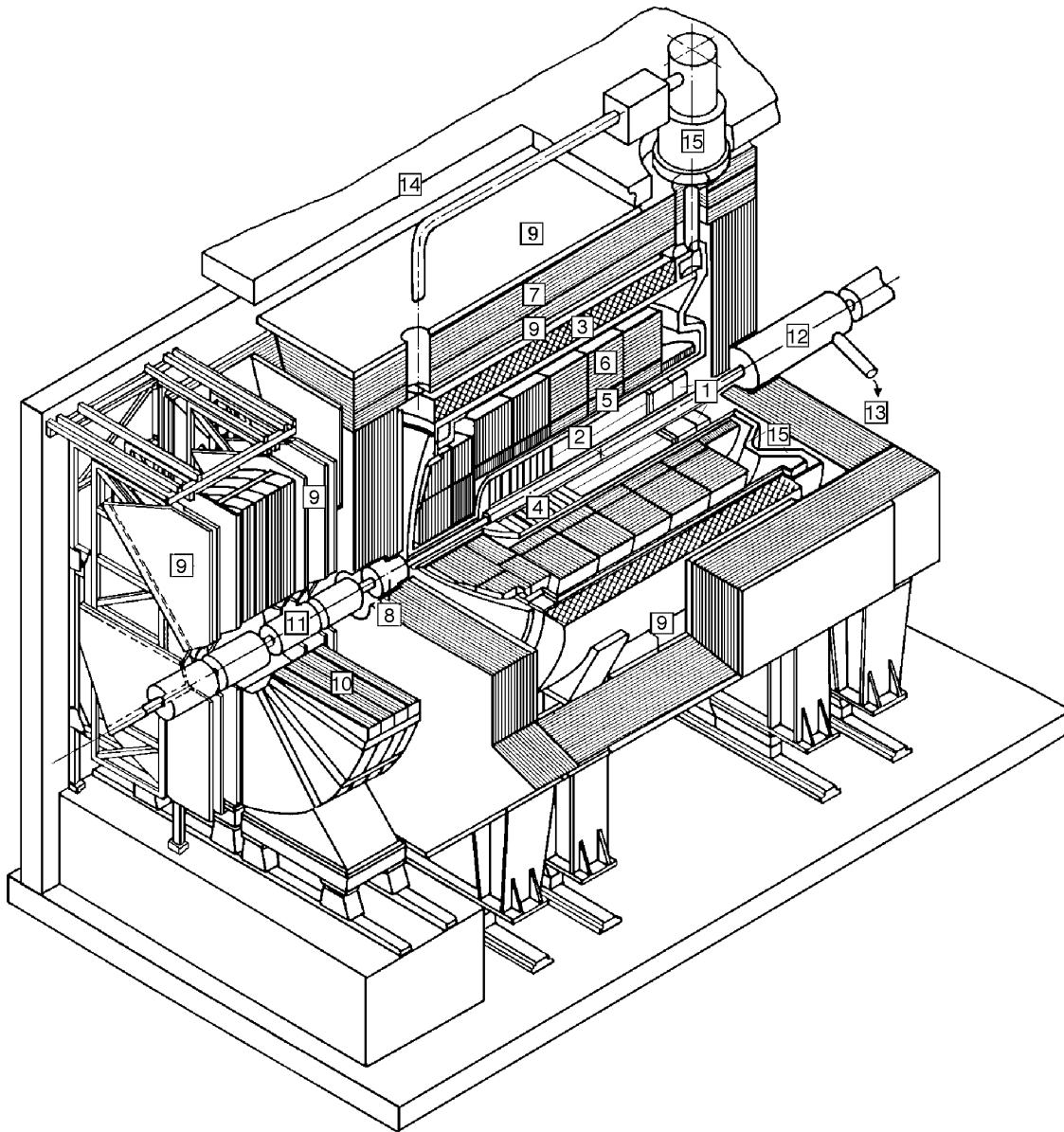


Figure 2.3: An overview of the H1 detector including the beam pipe and close-by magnets **11**. Shown is the backward calorimeter SpaCal **1**, the central tracking chambers **2**, forward trackers **4**, electromagnetic and hadronic liquid argon calorimeter **5, 6** including the cryostat **15**, the super-conducting solenoid **3** providing a field of 1.2T and the required compensator magnet **12** with the helium cooling system **13**. Also shown are the plug calorimeter **8**, the muon chambers **9**, the return yoke with instrumented iron **7** and the muon toroid magnet **10**. Around the detector a concrete screen **14** is placed.

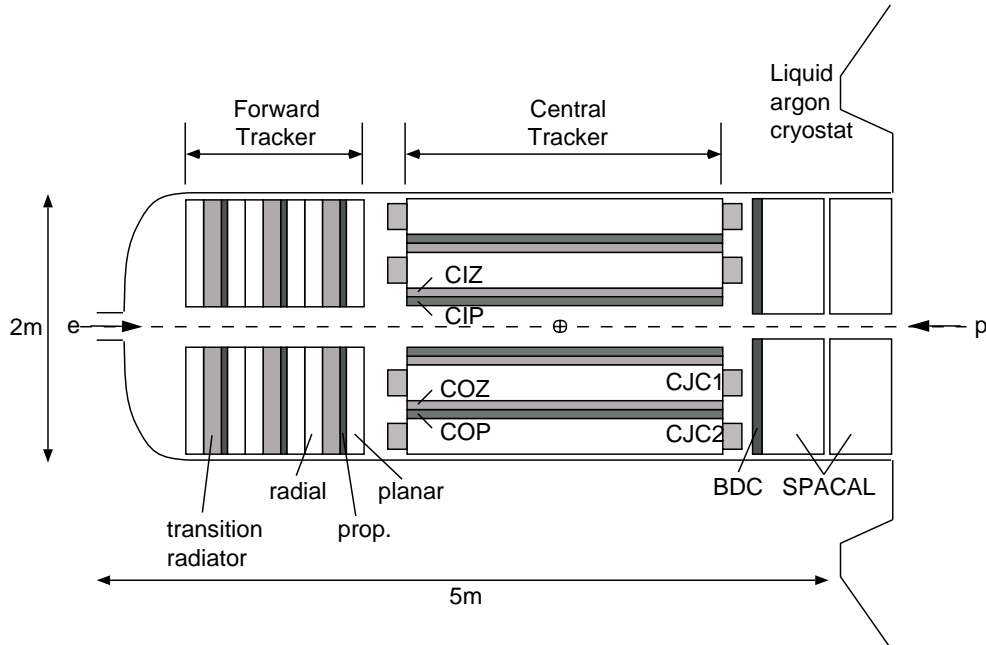


Figure 2.4: This drawing shows an overview of the tracking system of the H1 experiment consisting of forward, central and backward trackers (BDC).

2.2.1 The Tracking Systems

The tracking system of the H1 experiment (for an overview see figure 2.4) delivers the coordinates allowing to reconstruct the trajectories of charged particles in the detector, which in turn makes it possible to measure their momenta and the actual interaction vertex of the event. The measurement of the particle momenta is achieved with the aid of a magnetic field of 1.2T produced by the super-conducting solenoid. In this field, charged particles follow a spiral with a radius proportional to the particle transverse momentum (p_t) perpendicular to the field-lines, which are parallel to the beam axis. It is also possible to identify charged particles by measuring their specific energy loss dE/dx during their flight through the central tracking system. In this analysis, the central trackers are used to define the hadronic final state objects (see chapter 5.4.2) together with the calorimeter information. Particle identification is not used in the presented work. The forward and backward trackers are in this analysis only used for triggering events. A detailed overview of the entire H1 tracking systems can be found in [29].

The Central Trackers

The reconstruction of tracks in the central part of the detector is performed with the help of four concentric drift chambers, covering approximately the polar angles from 20° to 160° : two jet chambers *CJC1* and *CJC2* (central jet chambers 1 and 2) and the *z*-chambers *CIZ* and *COZ* (central inner and outer *z*-chambers), which are located immediately within and outside the *CJC1* [31, 32, 33]. The *CJC1* consists of 30 cells with 24 signal wires each, while *CJC2*

has 60 cells containing 32 signal wires. All of the in total 2640 signal wires are arranged parallel to the z -axis, which provides a spatial resolution in the $x - y$ -plane of about $170\mu\text{m}$ and a transverse momentum (p_t) resolution of $\sigma_{p_t}/p_t^2 < 0.02\text{ GeV}^{-1}$ [29]. The resolution in the z -direction of the jet chambers is about 2cm, which is unsatisfactory. Therefore, the z -chambers have wires, which are lying in the $r - \phi$ -plane perpendicular to the beam direction. The z -resolution can be improved using *CIZ* and *COZ* to about $300\mu\text{m}$ [34].

The Central Proportional Chambers

The central proportional chambers *CIP* and *COP* [35, 36] are multi-wire proportional chambers (MWPS's) which provide a fast response to the passage of particles within 21 ns. This time resolution allows to associate charged particles with single collisions, i.e. the bunch crossing for which the collision occurred can be determined. The chambers are divided into 8 segments in case of the *CIP* and 16 segments in case of the *COP*. Both MWPC's are also used to trigger on charged particles from the interaction point that pass the forward trackers (FPC, forward proportional chamber) [37, 38].

The Backward Drift Chamber

The backward drift chamber (*BDC*, see figure 2.6) is situated in front of the SpaCal calorimeter (see section 2.2.2) in the rear part of the detector and covers the polar angular range from 151° to 177.5° . The *BDC* is used to associate a track with a high energetic cluster in the calorimeter in order to improve the electron identification and to reduce background events (see section 5.3). Four double layers of wires, divided into eight sectors, are used for charged particle detection. Since the resolution in θ is most important, the wires are arranged in the $x - y$ -plane perpendicular to the radial direction. The double layers are rotated with respect to each other by 11.25° . A detailed description of the *BDC* can be found in [39].

2.2.2 The Calorimeters

Calorimeters measure the energy of showering particles and help to distinguish different types of particles. The two main calorimeters of the H1 experiment are the liquid argon (LAr) calorimeter, covering the central and forward region of the detector, and the scintillating lead fibre calorimeter SpaCal in the rear.

The Liquid Argon Calorimeter

The liquid argon calorimeter [40] (figure 2.5) covers the polar angle $4^\circ < \theta < 154^\circ$ and is divided into an electromagnetic and hadronic part in order to optimise the measurement of the energies of electrons, photons and hadrons. The active medium of the detector is liquid argon at a temperature of 90.2 K, which fills the space between absorber plates made of steel in the hadronic part and plates made of lead in the electromagnetic part of the calorimeter. In these plates, incident primary particles undergo interactions and produce showers of secondary particles. Some of the energy of the produced particles ionises the active medium, which is measured. While the many absorber plates ensure that also very high energetic particles deposit their energy within the calorimeter, only the energy loss in the active medium

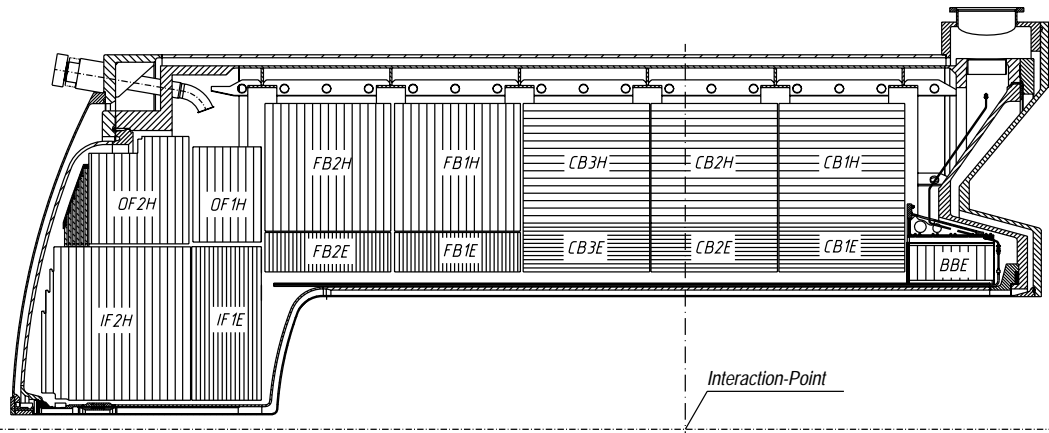


Figure 2.5: A cross-section of the upper half of the liquid argon calorimeter of the H1 experiment along the z -axis. The plates of the inner electromagnetic (dark hatching) and outer hadronic (light hatching) part of the detector are arranged such that the angle of incidence from particles coming from the interaction zone is larger than 45° .

can be measured. Hence the LAr calorimeter is a so-called “sampling calorimeter”. It only takes samples of the energy deposition between the absorber plates. The total deposited energy is then proportional to the energy deposited in the active medium. Since this is only a small fraction of the entire energy, statistical fluctuations of the number of charged particles, which ionise the active medium, limit the energy resolution. The number of charged particles produced is proportional to the deposited energy. In the case of electromagnetically interacting particles, this number is Gaussian-distributed, such that the energy resolution is $\sigma_E/E \sim 1/\sqrt{E}$. The relative error of the energy measurement of higher energetic particles is therefore smaller.

For hadronically interacting particles, the situation is more complex [41]. In hadronic showers mainly neutral pions, which decay into electromagnetically interacting photons, and charged pions, or kaons are produced, which can decay into muons or neutrinos. These particles easily escape the detector. Therefore, hadronic showers fluctuate strongly, depending on what particles are produced. In addition, the hadronic energy is underestimated due to the loss of particles, unless the calorimeter is a so-called “compensating calorimeter”, where the material and the thickness of the layers are chosen to compensate for this effect. The fluctuations of the shower lead to an energy resolution $\sim 1/\sqrt{E}$ typically worse than for electromagnetic showers. Furthermore, a constant term is induced in the energy resolution in the case of non-compensating calorimeters that limits the energy resolution at high energies.

The LAr calorimeter is segmented into about 45000 cells. This fine granularity leads to a good spatial resolution. In the electromagnetic part of the calorimeter 2.4 mm lead absorber plates take turns with likewise 2.4 mm thick layers of liquid argon. The electromagnetic part amounts to 20 – 30 radiation lengths x_0 in total. In the hadronic part the absorber is steel arranged in the form of 16 mm thick plates around argon filled gaps of 4.8 mm width. The whole calorimeter is between four to eight interaction lengths λ deep.

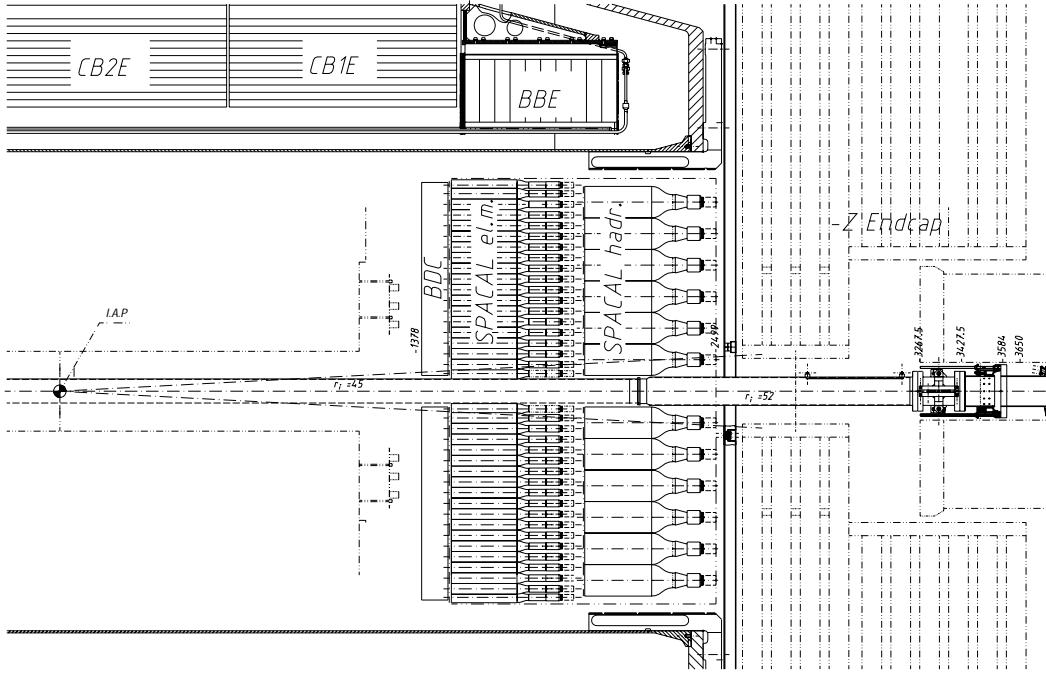


Figure 2.6: The backward spaghetti calorimeter (SpaCal) consists of an electromagnetic (inner) and outer hadronic part.

Test beams have been used to measure the energy resolution of the calorimeter. Using beams of electrons a resolution of

$$\frac{\sigma_E}{E} = \frac{12\%}{\sqrt{E/[\text{GeV}]}} \oplus 1\%$$

was determined [42], while with pion beams

$$\frac{\sigma_E}{E} = \frac{50\%}{\sqrt{E/[\text{GeV}]}} \oplus 2\%$$

was measured [43]. The LAr calorimeter is not intrinsically a compensating calorimeter. Instead, an energy weighting scheme [44] takes account of the underestimation of the hadronic energy off-line and adjusts the measured energy using a weighting function that depends on the amount of deposited electromagnetic energy. This explains the relatively small constant term in the energy resolution.

Particle showers usually extend over many cells. Therefore neighbouring cells are aggregated to clusters of cells which are also the objects that are used to define the hadronic final state objects (see section 5.4.2).

The SpaCal Calorimeter

The SpaCal (*Spaghetti Calorimeter*, see figure 2.6) is the backward calorimeter of the H1 experiment, which covers the polar angles between 155° and 177.5° [45]. It consists of

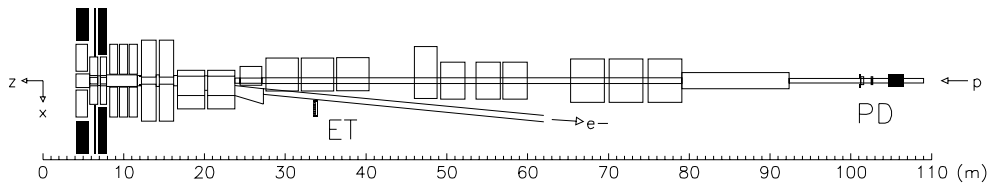


Figure 2.7: The luminosity system of the H1 detector consists of an electron tagger (ET) and a photon detector (PD) which can measure the coincidence of emitted photons and scattered electrons of the Bethe-Heitler process $ep \rightarrow ep\gamma$.

an electromagnetic and a hadronic part. The name is due to scintillating fibres, which are oriented in beam direction and are embedded in grooves of lead plates, which act as the absorber material.

Since measuring the exact position and energy of scattered electrons is the most important task of the SpaCal, the electromagnetic part of the detector consists of a large number (1192) of cells with a size of $4 \times 4 \times 25 \text{ cm}^3$. The depth of 27.5 radiation lengths ensures that the energy of electromagnetically interacting particles is well contained. The energy resolution in this part is $\sigma(E)/E = 7\% / \sqrt{E/[\text{GeV}]} \oplus 1\%$ [46].

The hadronic part of the SpaCal consists of 136 cells with a volume of $12 \times 12 \times 25 \text{ cm}^3$. Electromagnetic and hadronic part of the calorimeter together are two nuclear absorption lengths deep, which is not enough to contain a hadronic shower. In the hadronic part the energy resolution is $\sigma(E)/E = 30\% / \sqrt{E/[\text{GeV}]}$ [47] if the shower is contained in the calorimeter.

In this analysis the SpaCal is mainly employed to measure the energy and the position of the scattered electron.

2.2.3 The Luminosity System

The luminosity delivered by the HERA machine is measured using the Bethe-Heitler process $ep \rightarrow ep\gamma$ [48] in which a bremsstrahlung photon is produced. This elastic scattering process can be calculated in QED and is independent of the inner structure of the proton. In principle, the photon and the scattered electron can be measured in coincidence by the luminosity system (shown in figure 2.7) of the H1 experiment, which consists of an electron tagger and a photon detector. However, due to the uncertainty of the efficiency of the electron tagger of $\approx 3\%$, only the photon detector is used leading to a slightly higher background rate. Using only the photon detector, the luminosity can be measured with a precision of 1.5% [49]. Both detectors are made of small crystal scintillating calorimeters which are located close to the beam pipe in 33 m (electron tagger) and 103 m (photon detector) distance to the interaction point in electron direction.

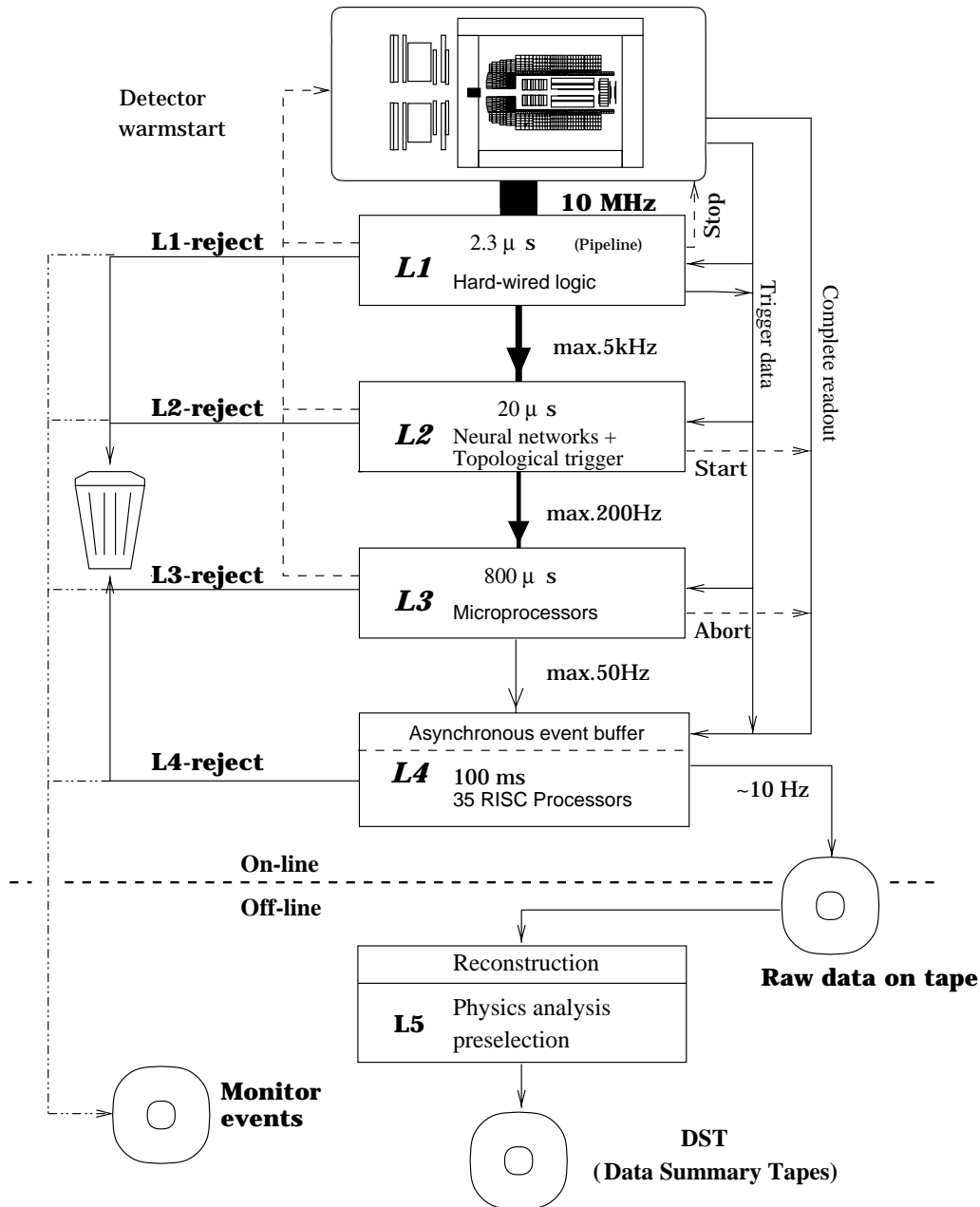


Figure 2.8: The H1 experiment has a four level triggering system, where on each subsequent level the rate of events is reduced, and thus more time is available for decision making. Only the level *L1* and *L4* are equipped with a buffer which stores incoming data during the processing time, such that they work without dead time.

2.2.4 The Triggering System

The constant stream of information of about 100kByte of zero suppressed data per event caused by *ep*-collisions as well as background events is far more than can be stored on the

tape systems of H1, which can only cope with a data rate of about 1.2MByte/s. Therefore, it is necessary to filter out events of interest and suppress the background events, which have a rate of the order of 100kHz. At the H1 experiment, an on-line four level triggering system is employed, to reduce the rate of events. On the first level the least time is available for decision taking and therefore only simple requirements are used. The following trigger levels have an increasing amount of time for use and can thus take more complex decisions. Using several filtering levels with increasing time for complex decision taking makes the overall system simple, since only a few hardware components are necessary to sequentially process the events. In contrast, a data acquisition system which would read-out nearly every event and process all the events in a final and necessarily parallel step, as is now proposed by the LHC experiments, is far more complex and also very expensive.

An overview of the four on-line triggering levels and the fifth off-line selection step is given in figure 2.8. Employing a zero suppression algorithm, the 3MByte information per event can be compressed to about 100kByte. Thus about 10 events can be written to a storage tape per second. In the following, a short description of the trigger levels is given. A full description of the system can be found in [50].

The First Trigger Level

Main task of the first level trigger (*L1*) is to discriminate between background events and *ep*-scattering events due to electrons and protons from both beams colliding with each other. The *L1* trigger resembles a hard-wired logic circuit which connects the triggering information of individual subcomponents of the detector to 256 so-called “trigger elements”. Since some of the detector components cannot deliver their trigger signal within the time of one bunch crossing ($BC \hat{=} 96\text{ ns}$), a ring buffer (also called “pipeline”) with a depth of 24 entries is used to buffer the event information, until all the data coming from the subdetectors is collected after at most $2.3\ \mu\text{s}$. The central trigger logic (CTL) then forms out of the trigger elements 128 subtriggers, logically connecting the trigger elements. If one or more of the subtriggers matches its condition the pipeline is stopped and a *L1-keep* signal is emitted. Since the ring buffer now cannot continue to collect information from the detector subcomponents, the time until the pipeline is restarted is the dead time of the detector.

The Second Trigger Level

More complex decisions than at the first level of the triggering system can be taken at the second level, since here not only the trigger elements are available, but also the detailed information which was used to compile them. In addition, up to $20\ \mu\text{s}$, i.e. nearly ten times more time than on the previous level, is available for the decision making after the *L1-keep* signal was emitted.

On *L2* two independent trigger systems, *L2NN* and *L2TT*, are present. *L2NN* is a neural network trigger [51], which uses up to 13 neural networks (see also section 3.3). The neural networks are implemented in dedicated microprocessors and can exploit the multidimensional correlations between the input quantities. *L2TT* is a second level topological trigger [52], which uses topological correlations in two dimensions of the input data.

Both triggers provide their decision in form of *L2* subtriggers. A list of *L1* subtriggers

is assigned to every L2 subtrigger, which need to fire in coincidence, thus validating the L2 subtrigger. If this requirement is fulfilled, the *L2-keep* signal is set. The output rate of the second trigger level is approximately 45 Hz.

The Third Trigger Level

After the *L2-keep* signal was sent, all detector components are read out to collect the full information about the event, which lasts about 1.5 ms. Originally it was planned to use microprocessors to reconsider the *L2*-decision using the complete input information [53]. This system was never implemented.

The Fourth Trigger Level

On *L4* all detector information is available. It is stored in a buffer, which can hold up to 30 events, which are asynchronously processed by a farm of PowerPC computers, so that the time of processing does not contribute to the dead time of the detector. The computers reconstruct parts of the event and recalculate the decisions of previous trigger levels that can be overruled. *L4* also selects events which have been triggered by so-called “monitor triggers” on the lower trigger levels that randomly trigger on otherwise rejected events. This mechanism ensures that not accidentally all events of a certain kind are discarded. Another task of the *L4* system is to select rare events using so-called “finders”. These are subprograms that detect events of interesting physics channels, which would otherwise be suppressed by e.g. the rejection of events with low Q^2 . The trigger has a maximum output rate of about 10 Hz. Events that pass *L4* are classified according to pre-defined criteria which makes the subsequent physics analyses easier and faster.

It should be noted that the division of tasks of the *L4/L5* system is subject to a constant change of responsibilities, which also moved from one of the systems to the other, so that no separate description of *L5* is given here. For example, until the end of the year 1997 the classification of events was performed by the off-line *L5* process; this division was removed afterwards.

Chapter 3

Analysis Techniques

In chapter 1 a comparison of the expected cross-section of instanton-induced events and the expected rate of background events showed that a considerable reduction of background will be necessary to extract a sample of events with a high likelihood of being instanton-induced. In this chapter, the required classification techniques to discriminate background events will be presented. In the first section the principles of event classification will be developed, including the necessary terminology. Three different classification methods will be studied in more detail. A classification based on cuts on selective observables is presented in section 3.2, followed by a more sophisticated method based on artificial neural networks presented in section 3.3. Finally, a multivariate discrimination technique, which uses a range searching algorithm is studied in detail in section 3.4. All three methods are compared in section 3.5.

3.1 Event Classification

When searching for a distinctive type of events among a large number of background events, one is confronted with a problem known as event classification. Does an event with the properties that have been measured belong to the signal class (i.e. the class one is interested in) or the background class? In order to solve this problem, it is necessary to compare the properties of the event (also called “event variables” in the following) with the known or at least expected properties of signal type and background type of events. This comparison is done by calculating the normalised probability density of signal ρ_s and background events ρ_b at the position in the event variables space, which is given by the values of the measured quantities $\mathbf{x} = (x_0, \dots, x_n)$ of the event that is to be classified. The probability that this event is a signal type event is then given by

$$D(\mathbf{x}) = \frac{\rho_s(\mathbf{x})}{\rho_s(\mathbf{x}) + \rho_b(\mathbf{x})} \quad . \quad (3.1)$$

$D(\mathbf{x})$ can be calculated for any event with event variables \mathbf{x} . The function $D(\mathbf{x})$ is also called discriminant because it can be used to discriminate between signal and background events by cutting at a certain value. The remaining problem is to calculate or estimate the probability densities $\rho_s(\mathbf{x})$ and $\rho_b(\mathbf{x})$.

Estimating the probability density in event variable space for signal and background type of events is unfortunately a very difficult task for large dimensions n of the event variable space, if there is no theoretical model available, which gives a parametrisation of ρ_s and ρ_b . Usually only Monte Carlo generators (see the next chapter for an introduction into these computer simulations of high energy physics events) are available to simulate events, which allow to sample the needed probability densities. The techniques which are employed are divided into multivariate and univariate methods, depending on whether they take into account correlations among variables or not.

In the following sections the simple cut-based technique, which is a univariate method and two multivariate methods are described. The two multivariate methods are neural networks and a method which directly estimates the phase space density using range searching. A comparison between the three methods will be done using a simple example. While the performance of the discrimination techniques in a complex real world example cannot be estimated with such a toy-example, it will allow to demonstrate how the different methods work.

To compare different classification techniques, it is necessary to define a quantity which measures the performance of a selection. In this analysis the *separation power*

$$S := \frac{\epsilon_s}{\epsilon_b} = \frac{\frac{N_{s,\text{selected}}}{N_{s,\text{total}}}}{\frac{N_{b,\text{selected}}}{N_{b,\text{total}}}} \quad (3.2)$$

for a given signal efficiency $\epsilon_s = \frac{N_{s,\text{selected}}}{N_{s,\text{total}}}$ is used. This is equivalent to the commonly employed signal to background ratio at a given signal efficiency.

3.2 Univariate Classification Methods

An often applied method for background reduction is to impose a set of one-dimensional cuts on single variables characterising the events of interest. These cuts are normally optimised by examining the distributions of signal and background events in the characterising variables after sampling them with Monte Carlo generators. These methods are still in wide use in high energy physics, but they suffer from the fact that they only apply a cut on the linear combination of the variables and do not take complex correlations among the variables into account. Therefore these univariate methods do not perform optimally.

A two-dimensional example is shown in figure 3.1. Here, a signal and a second background distribution depending on two variables a and b are shown. Both distributions are Gaussian, with the signal having a spread of $\sigma_s = 0.5$ and means $\bar{a} = 5$, $\bar{b} = 3.5$, while the background distribution has a spread of $\sigma_b = 1$ and means $\bar{a} = 3$ and $\bar{b} = 4.5$. To choose cuts, which reduce the background while keeping most of the signal events, the projections onto the axes a and b are studied. These distributions are also shown in figure 3.1 together with the chosen cuts: $a > 4$ and $b < 4$. Applying these cuts, a signal efficiency of $\epsilon_s \approx 82.4\%$ is achieved with a separation power of $S \approx 17.7$.

Of course this cut is not optimal, and by looking at the two-dimensional distribution of events, it is clear that a line with a slope of 2 (which is the orthogonal to the connecting line between the two centres of the signal and background distributions) will give a much better

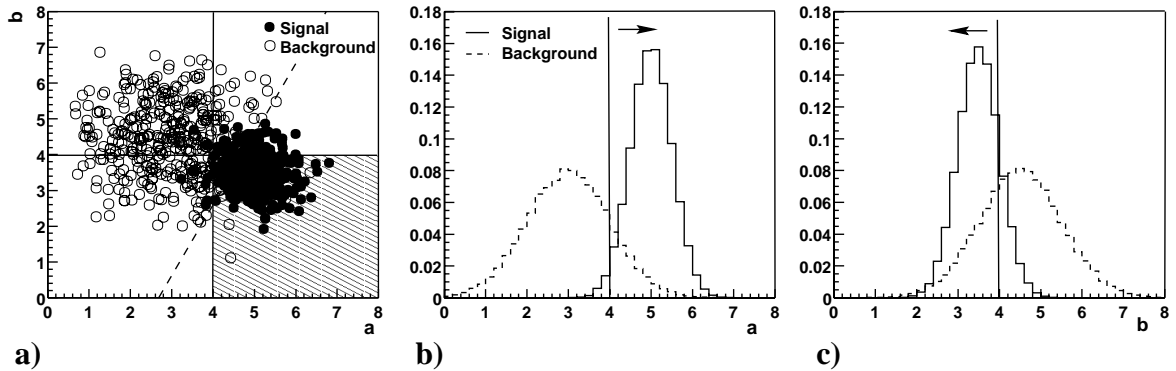


Figure 3.1: a) shows the phase space density in the variables a and b of a signal and a background class of events. Both classes of events follow a Gaussian distribution, but with different means and standard deviations. To select events of the signal class (full circles), cuts are applied with the help of projections of the distributions in a (figure b)) and b (figure c)), by defining the cut values $a > 4$, $b < 4$ as the intersection of the densities in the histograms. By looking at the phase space density in the selected region (depicted by the hatched area), it is clear, that this procedure does not maximise the signal to background ratio at a given efficiency of the signal class. Such a cut perpendicular to the principal axis is shown as a dashed line.

result. A cut at $b > 2a - 5.49$ achieves a separation power of $S = 22.4$ with a signal efficiency of 82.1% (see the dashed line in figure 3.1a). This method, namely designing the optimal cut by simply inspecting the distributions, does work for two variables, i.e. the two-dimensional case, but is not applicable in n dimensions. Nevertheless, the same cut could be calculated automatically by applying a transformation to the principal axes of the two distributions. This transformation is, however, only linear and while it will work in this toy-example, it cannot take into account more complex correlations of the distributions.

3.3 Neural Networks

Artificial neural networks (NN) are computational tools, which are inspired by the way living nets of neurons work and which can be used to tackle problems such as pattern recognition; a task real neural networks are very good at. The similarity to biological neural nets comes from the fact that neural nets simulate neurons that form networks, which change their properties in a learning phase before they are applied to pattern recognition problems. An introduction to neural networks can be found in [54]. NNs have been successfully applied to a variety of classification problems in high energy physics. An overview can be found in [55].

The building block of an artificial neural network is the formal neuron, which is depicted in figure 3.2a. It receives a vector $\mathbf{x} = (x_1, x_2, \dots, x_n)$ of inputs and calculates a response $y = g(w_o + \mathbf{w}^T \mathbf{x})$ depending on the vector of weights $\mathbf{w} = (w_1, w_2, \dots, w_n)$ that scales the input of the formal dendrites, a threshold w_0 and a monotonically increasing response function

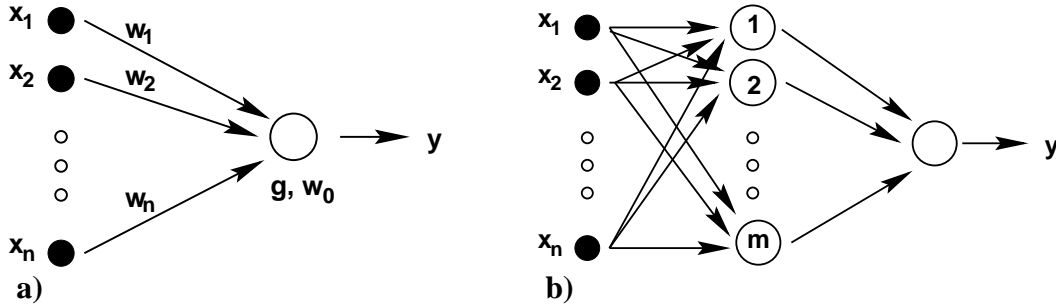


Figure 3.2: a) A single formal neuron with n input nodes that can be used to form a neural net. b) the depicted network has one input layer with n input nodes, a single hidden layer with m nodes and one output neuron.

such as

$$g(x) = \frac{1}{1 + e^{-x}} \quad . \quad (3.3)$$

The scalar product $\mathbf{w}^T \mathbf{x}$ actually defines a distance to a plane perpendicular to \mathbf{w} , which thus divides the space into two regions separating the classes of events.

In a feed-forward layered network the neurons are arranged in consecutive layers where every neuron in a layer receives only input from the layer in front. Such a feed-forward network with one “hidden layer” and only one output node is illustrated in Figure 3.2. A restriction to a single output node allows the response of this node to be interpreted as a “yes” or “no” answer to a classification problem, but such a restriction is not necessary for more general networks. Adding more hidden layers is also possible. In general, neural networks can be described by a mapping $\mathbf{G}(\mathbf{x}, \mathbf{w})$ which maps the input vector \mathbf{x} to an output vector \mathbf{y} . In this notation \mathbf{w} contains all the weights of the neurons. For classification purposes the output of a neural network is usually a scalar $G(\mathbf{x}, \mathbf{w})$. Only such networks will be studied in the following.

In a training phase with N known input-output pairs the weights of the net are adjusted to optimise the error function

$$R(\mathbf{w}) = \frac{1}{N} \sum_{i=1}^N |G(\mathbf{x}_i, \mathbf{w}) - y_i|^2 \quad (3.4)$$

which is the quadratic sum of the classification errors of the individual events. A common algorithm for the task of finding the optimal weights \mathbf{w}^* is the “Back-Propagation Algorithm”, which implements the gradient algorithm for the search of a local minimum [54]. In the case of classification the output of the neural network is compared to a threshold value α with

$$\begin{cases} G(\mathbf{x}, \mathbf{w}^*) \geq \alpha & \mathbf{x} \text{ accepted as signal,} \\ G(\mathbf{x}, \mathbf{w}^*) < \alpha & \mathbf{x} \text{ rejected.} \end{cases} \quad (3.5)$$

Since $g(x) \in (0, 1)$, the threshold parameter should be chosen as $0 \leq \alpha \leq 1$, and it is not possible to map the signal and background events to 1 and 0 itself. Instead, in practice

one chooses a small parameter ε such that signal type events will be mapped to $1 - \varepsilon$ and background events to ε .

In the following, it will be shown that the decisions of the neural network can be considered as a cut on a discriminant (3.1). Let the training events \mathbf{x}_i with designations y_i be values of random vectors \mathbf{X} and Y such that (3.4) samples the mean error of the net

$$R(\mathbf{w}) = \int d\mathbf{x} (G(\mathbf{x}, \mathbf{w}) - (1 - \varepsilon))^2 \rho_s(\mathbf{x}) + \int d\mathbf{x} (G(\mathbf{x}, \mathbf{w}) - \varepsilon)^2 \rho_b(\mathbf{x}) \quad , \quad (3.6)$$

where the integration is over the whole n -dimensional event variable space. It can be shown that

$$\gamma(\mathbf{x}) := (1 - \varepsilon) \frac{\rho_s(\mathbf{x})}{\rho_s(\mathbf{x}) + \rho_b(\mathbf{x})} + \varepsilon \frac{\rho_b(\mathbf{x})}{\rho_s(\mathbf{x}) + \rho_b(\mathbf{x})} \quad (3.7)$$

is the mean value of Y when $\mathbf{X} = \mathbf{x}$. From the theory of regression it is known that a net that minimises (3.6) approximates the mapping $\gamma(\mathbf{x}) = y$ (for a proof see e.g. [56]). Using sufficiently large networks in principle very general mappings can be approximated by the output of the neural network [57]. Therefore, the output of the neural network is asymptotically

$$G(\mathbf{x}, \mathbf{w}^*) \approx \gamma(\mathbf{x}) \quad . \quad (3.8)$$

Looking closer at equations (3.7) and (3.8), one can see that the classification rule (3.5) is actually a cut on a discriminant as defined in (3.1):

$$\begin{cases} D(\mathbf{x}) \geq \alpha & \mathbf{x} \text{ accepted as signal,} \\ D(\mathbf{x}) < \alpha & \mathbf{x} \text{ rejected.} \end{cases} \quad (3.9)$$

From the above discussion on the functioning of a neural net, it is clear, that neural networks classify events by fitting $D(\mathbf{x})$ in the learning phase by adjusting the weights \mathbf{w} . Event classification is then done by calculating $D(\mathbf{x})$ for an input event and comparing to a cut parameter α . While well trained NNs show an excellent classification performance (for a comparison with other classification methods, see e.g. [56]) since large enough networks can fit arbitrary probability densities, the way they work also has some drawbacks in practice. Because the back-propagation algorithm is a local minimum finder, it can also happen, that the global minimum is not found. Therefore, human intervention is necessary to evaluate the performance of trained networks and change the initial conditions of the fitting procedure accordingly. This can be a substantial amount of work. When neural networks are used for a search for a new type of events, another problem arises due to the non-locality of the fit of $D(\mathbf{x})$ in the parameter space. Events that neither match the signal nor the background events will be classified anyway, with arbitrary result. Improper modelling of signal and background can thus easily result in a fake signal.

To demonstrate the power of neural networks, a single hidden layer feed-forward neural network¹ with two input nodes, ten nodes in the hidden layer and a single output node is applied to the problem already presented in the previous section. 30000 ‘‘events’’ have been used to train the network and 5000 events have been used as a validation sample for signal

¹A package from J. P. Ernenwein was used. It is written in C++ and can be used in the ROOT [58] analysis framework. The source code is available at <http://e.home.cern.ch/e/ernen/www/NN/>.

and background, each. In figure 3.3a the mean classification error (3.4) achieved by the network during the 100 training cycles is shown. The network optimises the error using the 30000 training events, while the performance of the network is measured with the validation events. This avoids that the network adjusts to the statistical fluctuations of the limited data sample and neglects the relevant information for the general case. This behaviour is called “over-learning”. Diverging errors in the learning curves for the training and validation sample are a sign of over-learning, which is not the case here. Over-learning happens if too few training events are used to train a neural network with a large number of adjustable weights. As a rule of thumb the number of events used for training should be at least ten times the number of adjustable weights. This condition is easily fulfilled in the example.

The resulting classification of the validation events is shown in figure 3.3b. Cutting at a network output value of larger than 0.87 yields a signal efficiency of 82.1%, which is only slightly lower than the signal efficiency in the example using simple cuts. The network achieves a separation power of $S = 27.2$. This is an increase of 54% over the simple cuts studied in the previous section! This increase in the separation power compared to the simple cuts shows the power of neural networks.

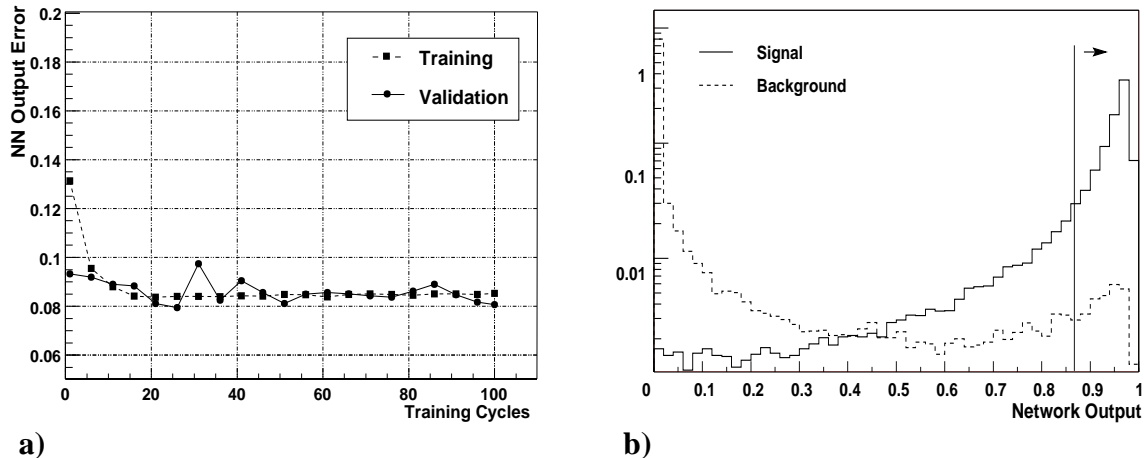


Figure 3.3: The performance of the neural network: In a), the mean error of the neural network during the 100 training periods is shown for the training (dashed) data sample and the validation data sample (full line). b) shows the output distribution for the validation background and signal events. The line at a network output of 0.87 marks the region, in which 82.1% of the signal events are found.

3.4 Event Classification Based on Range Searching

A different concept of estimating the density of signal and background events at a point in event variable space is to count the number of signal and background events in a small volume around the point in question. The ratio of the number of signal events over the

number of background events in the small volume $V(\mathbf{x})$ around the point \mathbf{x}

$$\ell(\mathbf{x}) := \frac{\text{\#Signal-Events in } V(\mathbf{x})}{\text{\#Background-Events in } V(\mathbf{x})} \sim \frac{\rho_s(\mathbf{x})}{\rho_b(\mathbf{x})} \quad (3.10)$$

is proportional to the ratio of the signal and background probability densities at \mathbf{x} . By normalising $\ell(\mathbf{x})$ with the total number of background over the total number of signal events, the probability of an event to be a signal event is given approximately by

$$D(\mathbf{x}) \approx \frac{\ell(\mathbf{x})}{1 + \ell(\mathbf{x})} \quad (3.11)$$

(this is equivalent to the definition of $D(\mathbf{x})$ in (3.1)). The approximation provides a good estimate of the local event density and prevents a wrong classification due to bad interpolation by methods that try to fit the event density globally. However, a large number of Monte Carlo generated events is needed to densely populate the whole phase space. This can be a limiting factor, if the number of variables and thus the dimensionality of the problem is high. If this is the case, then neural networks will probably give better results, since they are interpolating the density in variable space over a large volume. In any case, a large number of Monte Carlo events is needed and in the vicinity of each event to be classified a large number of events has to be counted — a potentially time-consuming task. This problem is known as “Range Searching” in computational sciences.

Range searching has been studied intensively since several years, because the problem occurs in all sorts of classification tasks. Searching e.g. for people fulfilling certain selection criteria in a database of inhabitants² is essentially the same problem. Powerful algorithms have been devised to tackle this task [59, 60]. They can be used with today's computers to also scan millions of Monte Carlo generated events in order to estimate the event density in a high dimensional variable space in reasonable time. Two different classes of algorithms are usually applied: One which subdivides the entire volume of the variable space into small boxes and stores the events within the boxes in a linked list³. Searching for an event then just involves looking up which boxes are in the vicinity of the event that is to be classified and then simply scan the linked list for events within a certain distance. The second class of algorithms use multi-dimensional binary trees to store the events. An algorithm of this class as described in [61] has been used for this analysis and will be described in detail in section 3.4.1.

The choice to use an algorithm employing binary trees was based on the characteristics of algorithms using a subdivided volume with linked lists, which limit their use in high energy physics. These algorithms require prior knowledge of the extent of the variable space and have a huge memory consumption, if the dimensionality of the problem is large, since they have to store the pointers to the linked lists in an array of the dimension of the problem, even if no event lies in a box. Such a behaviour is expected for high energy physics events, for which the variables describing their properties are in many cases correlated.

²A controversial application of this is known as “Rasterfahndung” in German.

³A data structure with a data member (the event) and a pointer to the next structure.

3.4.1 The Range Searching Algorithm

The algorithm used in this analysis for the classification of events is based on the range searching algorithm described in [61]. The main parts of the actual implementation can be found in appendix A together with some comments on the time and memory consumption. The algorithm allows to search through n Monte Carlo generated events that sample the signal and background density within a time $\sim \log(n)$. To achieve this scaling of the algorithm with the total number of events, all n events are first stored in two multi-dimensional binary trees — one for the background and one for the signal events — as is sketched in figure 3.4 for a two-dimensional example: Consider a random sequence of signal events $e_i(x, y)$, $i = 1 \dots 7$ shown in figure 3.4a with their position in $x - y$ -space, which are to be stored in a binary tree⁴. The first event in the sequence becomes by definition the topmost node of the tree. The second event $e_2(x, y)$ has a larger x -coordinate than the first event, therefore a new node is created for it and the node is attached to the first node as the right child (if the x -coordinate had been smaller, the node would have become the left child). Event e_3 has a larger x -coordinate than event e_1 , it therefore should be attached to the right branch below e_1 . Since e_2 is already placed at that position, now the y -coordinates of e_2 and e_3 are compared, and, since e_3 has a larger y , e_3 becomes the right child of the node with event e_2 . Thus the tree is sequentially filled by taking every event and, while descending the tree, comparing its x and y coordinates with the events already in place. Whether x or y are used to compare depends on the level within the tree. On the first level, x is used, on the second level y , on the third again x and so on. The result for events e_i is shown in figure 3.4b. The amount of time needed to fill the tree is $\sim \sum_{i=1}^n \log(i) = \log(i!) = O(n \log(n))$. The last equality can be easily verified with the help of STERLING's formula.

Finding all events within the tree which lie in a given box, is done in a similar way by comparing the bounds of the box with the coordinates of the events in the tree. For example, if the whole box lies to the right of event e_1 , then only events on the branch below and including e_2 need to be searched. This halves the number of events in question. Only if an event in a node lies within the bounds of the coordinates of the box that it is compared to, both its siblings need to be searched. Searching the tree once requires therefore an effort only $\sim \log(n)$. It needs to be noticed that the whole tree of Monte Carlo generated events needs to be kept in the main memory of the computer to have a reasonably fast access time when comparing the coordinates. Therefore, only the advent of computers with random access memory on the order of hundreds of megabyte makes it possible to use millions of events to sample the signal and background densities.

3.4.2 Properties of Range Searching

Classification problems in high energy physics have so far not been solved by using range searching, since only recent computers have the power to store millions of events in random access memory. The performance of this ansatz therefore needs to be evaluated. Here, range searching shall be applied to the toy-model defined in section 3.2. A comparison to neural networks for a more complex real-world problem will be done in chapter 8.

⁴The algorithm described here differs slightly from the implementation in the appendix, where an optimisation for speed and simplicity of the code was done.

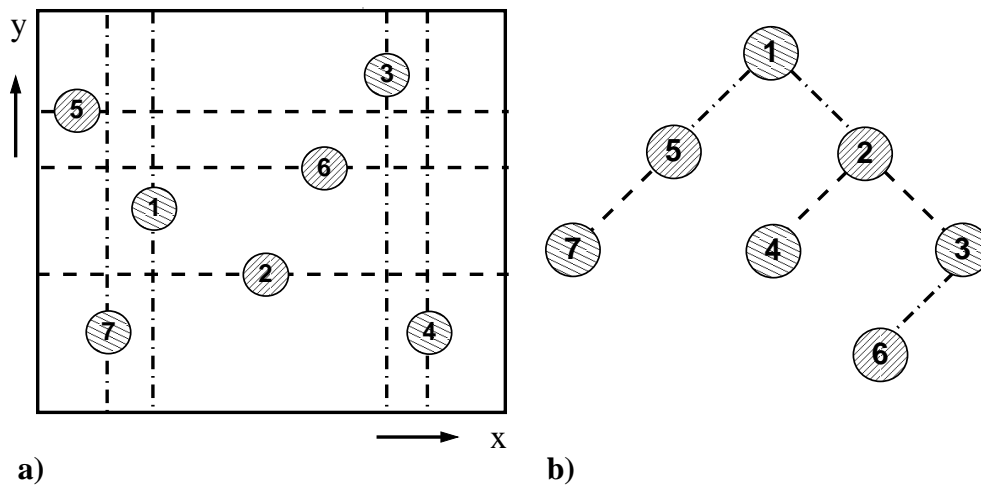


Figure 3.4: Example of a binary tree storing events 1–7 according to their position in the $x - y$ -plane (a). The first event is always the top node of the tree (b), which has two daughter nodes for events with smaller and larger x -value. On the second level the tree then sorts according to y .

As for neural networks, it is prudent to split the Monte Carlo generated events modelling signal and background into “training” and “validation” samples, where the training events are stored in the binary trees and the validation events are used to estimate the performance of the discriminator. If the same events are used to fill the binary trees and to measure the performance, this will yield seemingly too good results, since within each box around a signal event that is to be classified at least one signal event is found — the event itself that was stored in the signal tree. The same is true for background events. As in the example using the artificial neural network in the previous section, 30000 events were stored as training events in the binary trees for classification purposes, and 5000 validation events were used to calculate the performance.

The only free parameters of the algorithm are the lengths of the edges of the volume in which the events are counted. To reduce the number of parameters, the box is set to have sides of equal length $2d$ so that d is the largest distance in the maximum norm of every counted event to the centre of the box. Figure 3.5 shows the separation power S at a signal efficiency of 82.4% as a function of d for the toy-problem introduced in section 3.2. The separation power has a broad plateau and within one order of the box-size d , S only varies within 20%. This behaviour makes the separation power nearly independent of the box-size and will allow to use the algorithm with a minimum human intervention.

The fall-off of the separation power towards larger bin-sizes can be explained by the worse resolution of the sampling of the event densities around the event to be classified. On the other hand, too small boxes will diminish the number of events in the box and thus will also make the resolution of the discriminant smaller, because events which are neighbours might end up in different places of the distribution of the discriminant due to statistical fluctuations. This leads to a smearing of neighbouring events across a larger part of the discriminant, which degrades the resolution. To limit this effect and to control the statistics

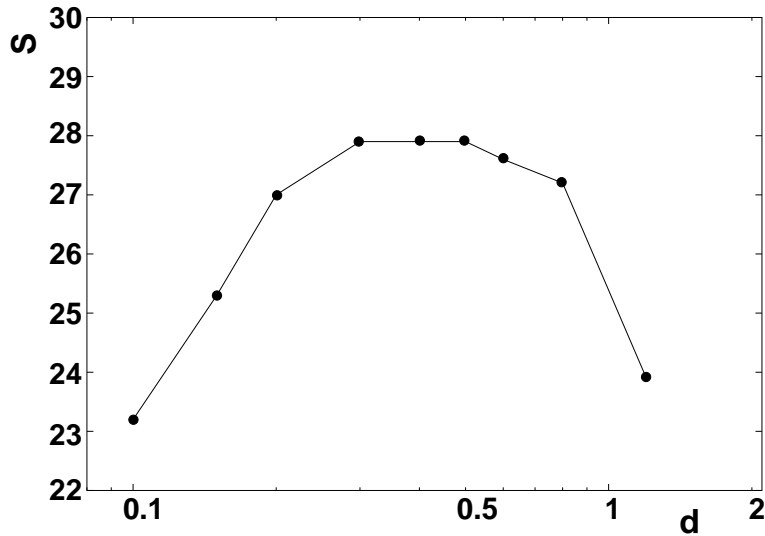


Figure 3.5: The dependence of the separation power S on the box-size d .

on which a decision is based, events which are to be classified have to have at least 20 signal and background events in their vicinity. Otherwise they will be classified as background ($D = 0$).

The maximum separation power at $d = 0.4$ is $S = 27.9$ which is even slightly larger than the result obtained with the neural network. The resulting discriminant D is shown in figure 3.6c and looks quite similar to the neural network output in figure 3.3b. Even the value at which D is cut (0.886) is similar to the cut on the network output (0.87). Figure 3.6b shows the discriminant $D(\mathbf{x})$ giving an idea of how the algorithm works.

3.5 Conclusions

The presented study on the classification algorithm based on range searching has shown, that the discrimination power of the method is always at least comparable to the discrimination power provided by neural networks. It has also been shown, that the method is rather insensitive to the choice of the free parameters that need to be set manually.

When comparing the time consumption of the range searching algorithm to the time needed by a neural network, it is interesting to note, that both algorithms have a very different behaviour. While for the range searching algorithm the time during the set-up period of filling the binary trees is more or less the time for reading in the data from a storage medium, the time needed to train the artificial neural network is considerable. On the other hand, the time needed to classify a single event after the initialisation phase takes longer with the range searching algorithm, at least when compared to NNs of moderate size. However, descending down the binary trees to collect events is a task which naturally parallelises, which has been done using multiple threads of program execution.

It is clear, that a simple toy-model as presented in this chapter, can only give a hint at the

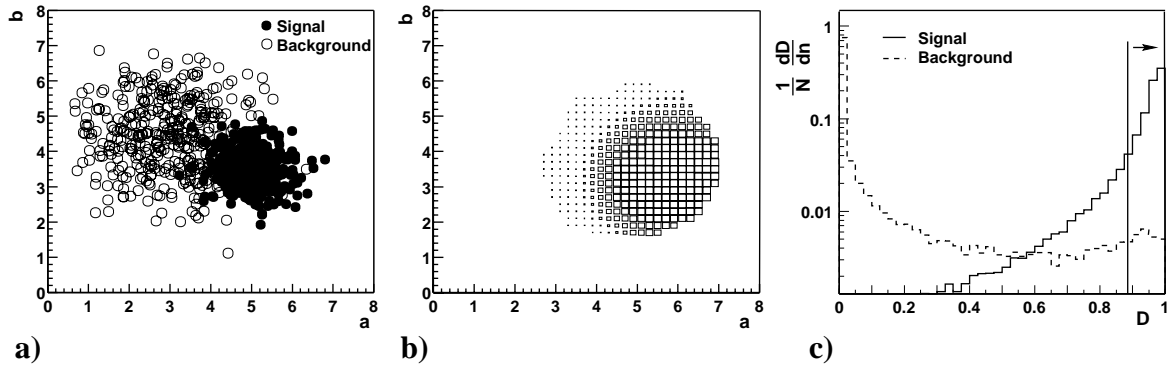


Figure 3.6: In a) the phase space density in the variables a and b of two classes of events is shown. Both classes of events follow a Gaussian distribution but with different means and standard deviations. b) depicts the output $D(a, b)$ of the range searching algorithm. Large boxes denote values close to 1 indicating regions with high likelihoods to find a signal event. c) shows the discriminant distribution of signal (full line) and background events (dashed line). The line at $D = 0.866$ marks the cut at which the signal efficiency is $\varepsilon_s = 82.4\%$.

behaviour of the algorithm in higher dimensional problems with more complex input data. This will be studied in more detail in chapter 8, where we will see that the range searching algorithm is also able to screen a large number of observables for those with a high combined discrimination power. This can only be done without too much human intervention due to the few parameters of the algorithm which are in addition not very sensitive. Another application will be presented in section 7, where the range searching algorithm is used to compare jets produced in instanton-induced events to a model describing the properties of the current jet. Since there no background event class is present, this problem cannot be tackled by neural networks in a straightforward way.

Thus, classification with range searching promises to be a powerful method which allows to control the classification error (because the statistics on which a decision is based is always known), and which works reliably and fast without too much human intervention since no training is needed. Therefore, in the search for instantons which is presented here, only the probability density estimator based on range searching will be used along with the more conservative cut-based method. NNs are used only to validate the performance of the range searching method, while the more conservative cut-based method is used as a cross-check.

Chapter 4

Monte Carlo Models

To search for instanton-induced events in deep-inelastic scattering, models of standard DIS events and of instanton-induced events are necessary. Such models are provided by Monte Carlo event generators which simulate the entire final state of DIS events. Applying a simulation of the H1 detector, Monte Carlo generated events can be directly compared to data taken with the detector.

Monte Carlo simulation of events is done in two separate steps, which correspond to the perturbatively calculable hard subprocess and the hadronization step, which encompasses the non-perturbative transition from partons to hadrons at a lower energy scale. Two Monte Carlo generators, RAPGAP [62] and ARIADNE [63], are used to simulate the perturbative processes in standard DIS events. Both generators incorporate $O(\alpha_s)$ matrix elements. The main difference of these programs is the treatment of higher order parton emission. RAPGAP implements the parton shower approach, while ARIADNE employs the colour dipole model [64]. Therefore RAPGAP will be referred to as “MEPS” (Matrix Element plus Parton Shower) and ARIADNE as “CDM” in the following. The standard DIS Monte Carlo generators are described in section 4.1. Instanton-induced processes are simulated by the Monte Carlo event generator QCDINS [14], explained in section 4.2. The hadronization step of the employed Monte Carlo generators is performed using either the “Lund-String-Model” [65] or the cluster fragmentation model [66]. Both models are explained in section 4.3. The simulation of the detector response to the generated Monte Carlo events is explained in section 4.4.

4.1 Standard DIS Monte Carlo Models

At the beginning of the simulation of a deep-inelastic scattering event at HERA, the independent kinematic variables of the event have to be generated. First, the total cross-section σ_{tot} is calculated by numerically integrating over the kinematic phase space, then a random point (x, Q^2) in this phase space is picked with the probability given by the normalised derivative of the cross-section $\frac{d^2\sigma}{dx dQ^2} / \sigma_{\text{tot}}$ with respect to x and Q^2 . Now a process in leading order α_s (QCD-Compton scattering or BGF, see section 1.4) or a QPM event is selected according to the calculated matrix elements, where the cross-section for a QPM event is given by the total cross-section minus the cross-sections of the BGF and QCD processes. Before and

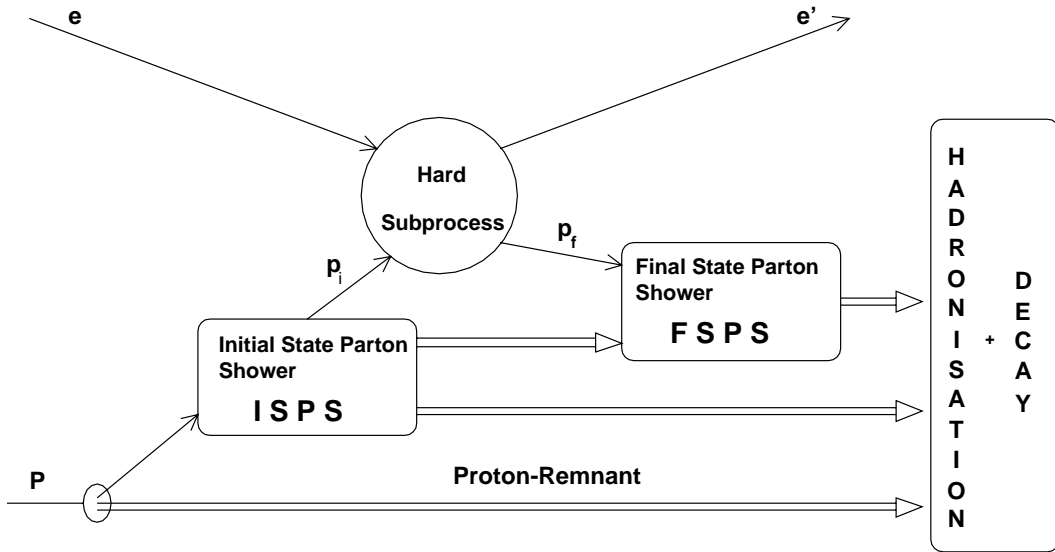


Figure 4.1: A sketch of the Matrix Element plus Parton Shower (MEPS) model. In this model, parton showers are emitted before (initial state parton showers) and after the hard subprocess (final state parton showers).

after the hard process, additional partons are produced which enter the hadronization step described in section 4.3.

The Monte Carlo generator RAPGAP implements the MEPS (Matrix Element plus Parton Shower) model depicted in figure 4.1 to simulate the hard subprocess and produce initial and final state partons. The matrix element of the hard subprocess is calculated in leading order α_s . Higher orders are approximated by the emission of partons in the initial and final state. The generation of parton showers is based on the DGLAP (Dokshitzer, Gribov, Lipatov, Altarelli and Parisi) evolution equations [67] which sum up higher order terms in α_s , i.e. terms $\sim \left(\alpha_s \log \frac{Q^2}{Q_0^2}\right)^n$, using the “leading logarithmic approximation”. By emitting space-like gluons ($m_g^2 > 0$) in the initial state, the parton entering the hard subprocess has a time-like virtuality $m_q^2 < 0$ which corresponds to the virtuality Q^2 of the event. In the final state parton shower, time-like gluons are emitted. Interference terms between the gluons emitted in the initial and final state are neglected in the RAPGAP Monte Carlo.

The ARIADNE Monte Carlo can only produce the parton cascade of an event and calculate the matrix element. It therefore needs to be plugged into another Monte Carlo generator that sets up the kinematics of the hard subprocess. The LEPTO [68] Monte Carlo generator can be used to generate the kinematical variables x and Q^2 . The emission of parton showers is implemented in the colour dipole model which assumes that a colour dipole is created between the scattered quark and the rest of the proton in case of QPM and QCD-Compton events. BGF-events are later added “by hand”. The colour dipole then emits additional gluons which form new dipoles with neighbouring partons as sketched in figure 4.2. The ARIADNE Monte Carlo generator calculates the matrix element in leading order α_s and

corrects the transverse momentum of the emitted partons accordingly. It should be noted that interference terms between the emitted gluons are taken into account by the described procedure.

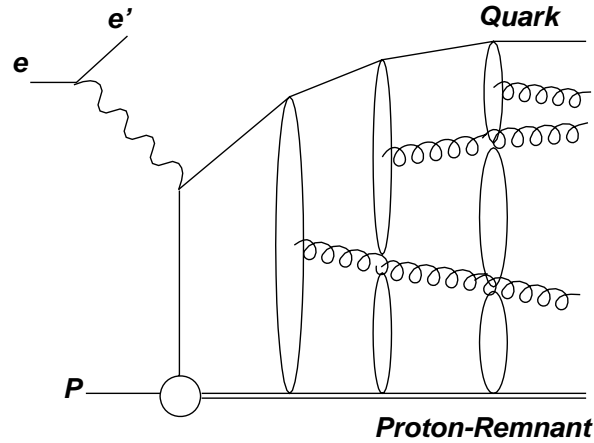


Figure 4.2: A sketch of the colour dipole model, which the ARIADNE Monte Carlo uses to generate partons. Between the struck quark and the proton remnant a colour dipole is spanned which emits a gluon, which again forms additional dipoles.

The Monte Carlo Generators need as an additional input the measured parton densities in the proton. Both Monte Carlo DIS samples employed in this analysis have been generated using the CTEQ4 [69] parton density functions and have been reweighted using a parametrisation extracted from the recent H1 measurement of the proton structure function [70].

The standard DIS Monte Carlo simulations used in this analysis were specially weighted to increase the statistics in the region of high values of Q^2 , large y -values and to enhance processes with high E_t , while keeping the overall amount of data small. This is done by generating a large number of Monte Carlo events and calculating a certain probability for every event to be actually kept. Events are then kept randomly according to this probability and a weight is assigned to the kept events, which is the reciprocal of this probability. Details of the method can be found in [71]. For the analysis, 301722 real MEPS events with a sum of weights of $1.754 \cdot 10^6$ and 163930 CDM events with a sum of the weights of 834000 were used.

4.2 QCDINS

The QCDINS Monte Carlo program [14] generates instanton-induced deep-inelastic scattering events as a hard subprocess (see figure 1.8) within the HERWIG Monte Carlo generator [72]. QCDINS first samples the total cross-section in the available $x' - Q^2$ phase space and then generates events with randomly chosen x' and Q^2 values according to the differential cross-section $\frac{d^2\sigma_{\text{INS}}}{dx' dQ^2}$ (see equation (1.38)). Using the incoming virtual photon with momentum q generated by HERWIG, the quarks with four-momenta q' and q'' are created

and the kinematic variables ξ, x and y are generated according to their distributions within the available phase-space. The four-momentum of the instanton can now be calculated as $g + q' = \xi P + q'$ and the instanton subprocess is generated in its centre-of-mass system.

The partonic final state is created by first generating n_g number of gluons according to a Poisson-distribution with mean $\langle n_g \rangle \approx 1/\alpha_s \approx 3$. In the next step quarks and anti-quarks are produced. Due to the flavour-democracy of the process, exactly one pair of each accessible flavour is produced. Each quark- anti-quark pair is associated with a random number of $\leq n_g + 1$ gluons (there is the additional gluon emitted by the proton), such that a “string” is formed with a quark at the beginning, the gluons in the middle and an anti-quark at the end. One of the gluons, quarks or anti-quarks is randomly marked as incoming. For the rest of the $2n_f + n_g - 1$ partons, momenta are generated in the instanton rest-frame according to an energy weighting scheme. Next, the colours and the colour connections are set up in the parton-“strings”, such that the colour flow is along the string. Finally, the particles generated in the hard subprocess are boosted into the laboratory frame. In this analysis, the CTEQ4 [69] parton density functions have been used with the QCDINS generator.

4.3 Hadronization Models

The final step in the generation of a DIS or instanton event is the formation of hadrons. Two models are used by the employed Monte Carlo generators. Most of the standard DIS Monte Carlo models use the JETSET [73] program, which implements the “Lund-String-Model”

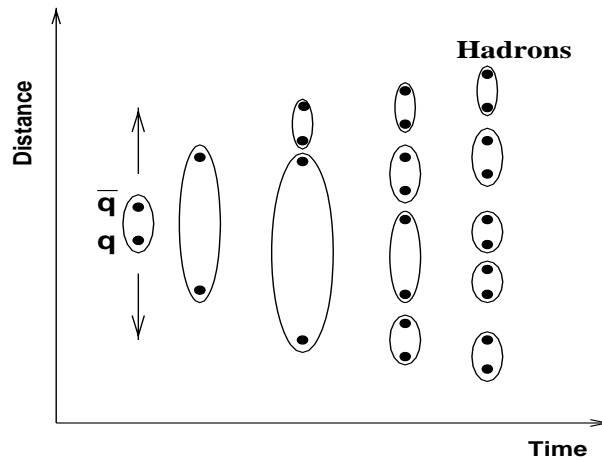


Figure 4.3: An illustration of the mechanism of the Lund String hadronization model. A $q - \bar{q}$ -pair builds up tension in the colour string between the two quarks when they separate. The breaking up of the string produces new quark- anti-quark pairs and further strings which fragment until the relative momentum is small enough to form hadrons.

[65, 73], depicted in figure 4.3. In this model, outgoing partons create a colour field between them, which is modelled as a flux-tube (also called “colour-string”) with a constant energy

density along its length. As an example, a $q - \bar{q}$ -pair is considered, with a large relative momentum. With growing distance, the energy stored in the flux-tube between the quarks grows until it is energetically favourable for the string to break up and create a new $q - \bar{q}$ -pair. Each of the quarks of this new pair is connected to one of the initial quarks by a new colour string. If the available energy is smaller than the energy necessary to create new pairs of quarks, the $q - \bar{q}$ -pairs are turned into hadrons.

The described model can also account for gluons in the final state, but then a detailed description becomes quite complex and may be found in [74].

QCDINS by default uses the hadronization routine included in HERWIG, which implements the cluster fragmentation model [66]. The cluster fragmentation model uses the *pre-confinement* property of perturbative QCD [75] which predicts a local colour compensation at the end of the generation of the parton shower. The gluons produced at the end of the parton shower development are split into quark- anti-quark pairs as shown in figure 4.4. Neighbouring quarks and anti-quarks are formed into colour-singlet clusters with an energy of typically a few GeV. If they are neither too light nor too heavy these clusters directly decay isotropically in the clusters rest-frame into two hadrons. If the mass of the cluster is too large, the cluster is split into two clusters. Clusters which are too light only decay into a single hadron, requiring a readjustment of momentum and energy in neighbouring clusters. Due to the domination of phase space in the formation of the clusters and their decay, the cluster fragmentation model has relatively few parameters.

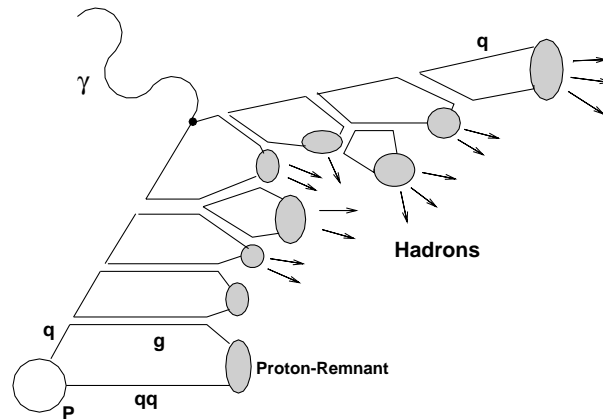


Figure 4.4: A sketch of the cluster fragmentation model. Gluons are depicted as double lines.

4.4 Detector Simulation

With the help of the program package H1SIM [76], the response of the H1 detector to the particles produced by the Monte Carlo generators is simulated. As a first step, the interaction of the particles with the detector is simulated. For this task, the GEANT [77] program is used,

which subdivides the detector into small cells and traces the passage of particles through these cells while taking the interactions of the particles with the material into account. In the following signal phase, the signals of the active detector regions are simulated including the entire read-out electronics. A simulation of the noise of the calorimeter is done by adding noise that was previously recorded. In the final step, called trigger phase, the reactions of the triggers to the simulated signals is calculated. The simulated events are stored in the same data format as the real data collected by the detector. They can therefore easily be compared to the measured data using the same analysis software. Monte Carlo generated events, which have undergone the detector simulation, are also called detector level Monte Carlo simulations in contrast to the hadron level Monte Carlo simulations.

Chapter 5

Data Selection

During the years 1996 and 1997, the period of time in which the data were taken for the presented analysis, the H1 experiment collected data amounting to a total integrated luminosity of 34.1 pb^{-1} [27]. However, not all the data taken during this time is of good quality and therefore some part of the data has to be excluded from the analysis. In addition, only deep-inelastic scattering events fulfilling certain well defined triggering conditions are taken into account. Finally, the kinematical phase space, in which the events taken have to lie, is limited by constraints that ensure that the kinematics of the event can be well reconstructed and that the necessary subdetectors work properly. In the following, the triggers that were required in the triggering condition of the events are described, then the restrictions on the phase space are explained and, finally, the technical cuts that ensure good data quality.

5.1 Used Subtriggers

To collect a well defined sample of events taken with the detector, it is necessary to require a well defined trigger condition for every event. In this analysis at least one of two *L1* subtriggers (*S1*, *S2*; see section 2.2.4) has been required. The sub-triggers depend on several *L1* trigger elements. In the following, these trigger elements are described as well as the dedicated triggers which provide the necessary input.

The *z*-Vertex Trigger

The *z*-vertex trigger (*zVtx*-trigger, [78]) finds the position of the vertex of the event on the *z*-axis with the help of the information of the *CIP*, *COP* and *FPC* trackers (see section 2.2.1). It reconstructs rays through the hits in the chambers and fills the position of their intersection with the *z*-axis into a histogram which has 16 bins covering the range in *z* from $z = -43.9 \text{ cm}$ to $z = +43.9 \text{ cm}$. The trigger elements provided by the *zVtx*-trigger are based on this histogram. The following trigger elements are used in this analysis:

zVtx_t0 This signal requires the *zVtx*-histogram to have at least one entry and can be used as a timing signal.

zVtx_sig The condition for this trigger element is satisfied, if the bin of the maximum of the histogram has a higher value than a certain threshold.

zVtx_mul This trigger element is a measure for the number of histogram entries. In this analysis $zVtx_mul < 7$ is used, which means that not more than 200 entries are in the histogram.

The DCRPhi-trigger

The *DCRPhi*-trigger [79] detects tracks in the $r - \phi$ -plane using the *CJC1* and *CJC2* tracking chambers (see section 2.2.1). It uses 10000 masks which are electronically overlaid on the digitised signals from the trackers. The trigger is capable of differentiating between tracks with high ($p_t > 800\text{MeV}$) and low ($400 < p_t < 800\text{MeV}$) transverse momentum, and can also distinguish between the sign of the charge of the particle. The trigger element used in this analysis is:

DCRPhi_THig This trigger element fires, if at least one of the masks for a high momentum track matches.

The Inclusive Electron SpaCal Trigger

In this analysis, it is demanded that the scattered electron hits the backward SpaCal calorimeter (see section 2.2.2). The SpaCal trigger fires, if a candidate for an electron is detected in the electromagnetic part of the calorimeter. The following trigger elements are provided and are relevant for this analysis:

SPCLE_IET > 1 This trigger fires, if the energy of the electron candidate, that is the sum of the energy of one trigger tower and its neighbours, is above a threshold of 2 GeV. The inner part of the calorimeter (the “CIET”-region) close to the beam-pipe, is excluded due to the high background.

SPCLE_IET > 2 The same as the previous trigger element, but the energy of the electron candidate is required to be above 6 GeV.

SPCLE_IET_Cen_2 The same as *SPCLE_IET > 1*, but including the inner region.

Veto-Trigger Elements

Two efficient systems of the detector to protect against non ep background events are the time of flight system (*TOF*) and the veto walls. The time of flight system consists of two detectors in the forward part of the H1 experiment, providing information on whether they registered a particle within (*FToF_IA*, *PToF_IA*) or outside (*FToF_BG*, *PToF_BG*) the time window of a bunch crossing. These trigger signals are combined to the veto requirement:

$$(FToF_IA \vee \neg FToF_BG) \wedge (PToF_IA \vee \neg PToF_BG) \quad . \quad (5.1)$$

It efficiently reduces background from beam-gas interactions or halo events. In beam-gas interactions protons collide with remnant gas atoms producing a large number of fragments. This can happen anytime during the passage of the proton bunches through the detector and these events can be efficiently rejected by accepting only events in the time window of the

ep -interaction. In halo interactions, particles away from the beam axis interact with each other outside of the interaction zone.

The subtriggers $S1$ and $S2$ are a logical concatenation of the above trigger elements. They are defined as:

$$S1 := SPCLe_IET > 2 \wedge zVtx_mul < 7 \wedge (zVtx_t0 \vee fwdRay_T0) \quad (5.2)$$

$$S2 := DCRPhi_THig \wedge zVtx_sig \wedge (SPCLe_IET > 1 \vee SPCLe_IET_Cen_2) \quad (5.3)$$

where $fwdRay_T0$ is a timing signal from the forward tracking system. In addition, both subtriggers require the above simple veto requirements. Trigger $S1$, prior to Sep. 5th 1996, had a different triggering requirement, so that in this analysis only data taken after this date is considered.

The subtrigger $S1$ suppresses events with a high multiplicity due to the $zVtx_mul < 7$ requirement. Since instanton-induced events are expected to have a high multiplicity, these events are of great interest to the analysis. The problem can be solved by requiring

$$S1 \vee S2 \quad ; \quad (5.4)$$

together they will also allow high multiplicity events to be triggered. In the following, the efficiency of this trigger condition depending on the multiplicity will be studied together with the dependency on the scattered electron energy, since it is equally important that the trigger condition is independent of the electron energy.

To study these dependencies, so-called ‘‘monitoring’’ triggers are used which have trigger requirements independent of the quantities relevant to the events. While it may seem that monitoring triggers might be better suited for the analysis, because they efficiently trigger the events in question, this is not the case, since the monitoring triggers normally have to be pre-scaled, i.e. only a certain fraction of the events being triggered by the monitoring triggers can be actually kept. The efficiency of the trigger is then given by the ratio of the number of events triggered by the monitor trigger *and* the physics trigger of the analysis to the number of events triggered by the monitor trigger alone

$$\varepsilon := \frac{N_{\text{Monitor Trigger}} \wedge N_{\text{Physics Trigger}}}{N_{\text{Monitor Trigger}}} \quad . \quad (5.5)$$

The monitoring triggers in this analysis are the triggers $S0$ and $S75$, where the trigger requirements of trigger $S75$ include only some energy deposition in the LAr calorimeter and $S0$ mainly requires $SPCLe_IET > 2$. The trigger $S0$ can therefore be used to monitor track conditions and $S75$ to monitor the electron finding in the SpaCal. The resulting efficiency as a function of the electron energy E_{el} is shown in figure 5.1a to be nearly independent of the electron energy and approximately 0.995 in the energy range relevant to the analysis. This factor is applied to the data as an overall correction factor for the trigger efficiency.

In figure 5.1b the dependency of the trigger efficiency on the track multiplicity in the central trackers is shown. As can be seen, using trigger $S1$ or $S2$ allows to efficiently trigger events with medium and high multiplicities. In the analysis, the data events are assigned a weight taking into account the efficiency of each event to have been triggered depending on the track multiplicity.

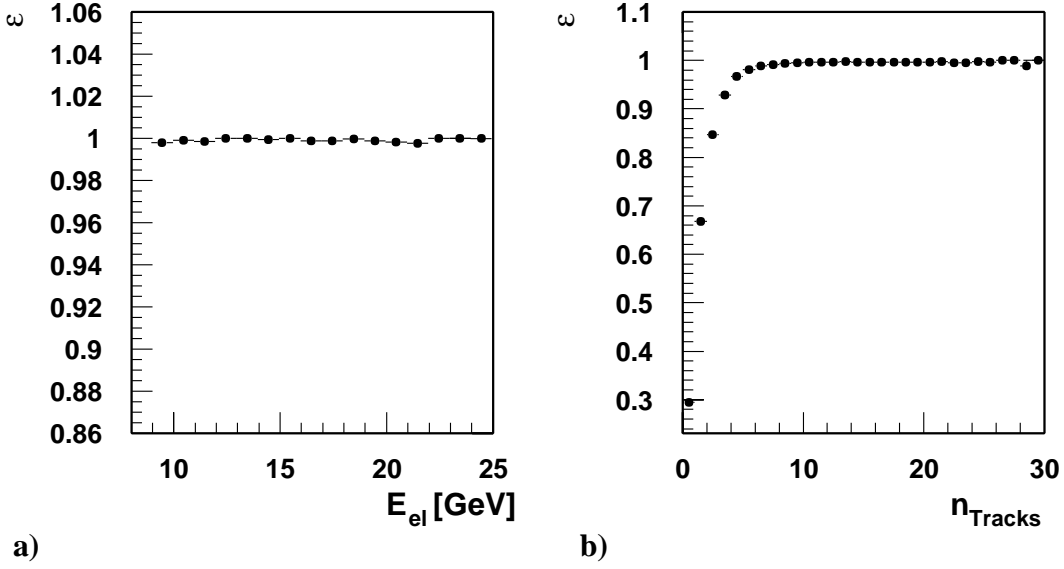


Figure 5.1: a) The dependence of the trigger efficiency ε on the scattered electron energy E_{el} and b) on the number of charged particle tracks n_{Tracks} in the central tracking system [80].

5.2 Kinematic Cuts

The kinematic variables of the selected events are reconstructed from the electron angle θ_e and electron energy E'_e of the scattered electron (the so-called “Electron-Method” [81]). The advantage of this method is that the kinematics does not depend on the hadronic final state. The following dependencies of Q^2 , x and y on θ_e and E'_e can be derived, neglecting the electron and proton mass:

$$Q^2 = 4E_e E'_e \cos^2 \frac{\theta_e}{2} \quad x = \frac{E_e E'_e \cos^2 \frac{\theta_e}{2}}{E_p \left(E_e - E'_e \sin^2 \frac{\theta_e}{2} \right)} \quad y = 1 - \frac{E'_e}{2E_e} (1 - \cos \theta_e) \quad . \quad (5.6)$$

The electron method allows a good resolution of the measurement of Q^2 , except for small polar angles θ_e . The resolution in x is good for sufficiently large y . For $y < 0.1$ the resolution is poor, since the x -resolution decreases with $1/y$ [82].

The distribution of the selected data events in the $x - Q^2$ -plane is shown in figure 5.2. The dots represent about 10% randomly picked events of the entire data sample. The lines denote the following cuts into the phase space, which are necessary to reduce either the experimental or the theoretical uncertainties of the analysis:

- A cut on the transferred momentum squared $Q^2 < 100 \text{ GeV}^2$ is a standard cut within H1 to distinguish between low and high Q^2 analyses. The cut is dictated by the use of the SpaCal calorimeter. For high Q^2 the electron is scattered into the LAr calorimeter.
- A cut on $0.1 < y < 0.6$. The cut $y > 0.1$ is necessary since below the accuracy of the reconstruction of the kinematics of the events by the electron method is poor. In

addition, at low y the hadronic final state can usually not be measured in the central part of the detector. The cut $y < 0.6$ is equivalent to a cut on the energy of the scattered electron of $E_{el} > 11$ GeV. This minimum energy of the electron is required to make sure the electron is correctly identified. The cut reduces background from photo production events, in which the exchanged photon is nearly real and not scattered into the SpaCal, but where hadronic final state particles, e.g. a π^0 or a charged pion can be misidentified as an electron.

- A cut on $x > 0.001$, which is (together with the y -cut) effectively a cut on the minimum $Q^2 \gtrsim 9 \text{ GeV}^2$ which limits the influence of non-planar diagrams on the instanton cross-section predictions (section 1.4). This cut was applied in the first cross-section calculation of instanton-induced events in [12].
- A cut on the scattering angle of the electron $\theta_e > 156^\circ$ ensures the electron is scattered well into the SpaCal and traverses the backward trackers.

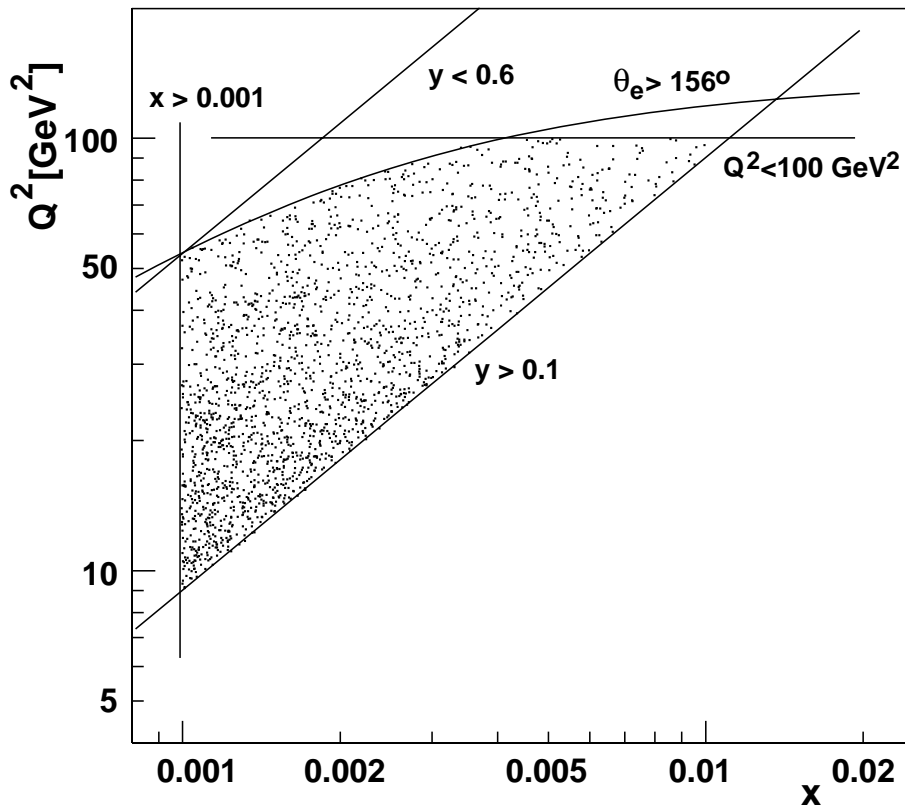


Figure 5.2: The distribution of the events in the kinematic variables x and Q^2 . In addition the kinematical cuts of this analysis are shown.

5.3 Data Quality Cuts

Several cuts were imposed on the properties of the events to ensure a good data quality of the selected events. In the following the cuts are presented and discussed.

5.3.1 Selection of Run-Ranges

The data acquired with the H1 detector are taken in so-called “runs” which last for up to two hours. Within each run the ambient conditions and the calibration of the subdetector systems are considered to be constant. During a run, the configuration of the detector, i.e. which subdetectors are used, does not change. A selection was done on the quality of these runs, requiring certain subsystems to work well and the beam conditions to be good. A list of the selected runs may be found in appendix A of [80].

5.3.2 A Cut on the Event Vertex

To make sure that the kinematic properties of an event are correctly reconstructed, the interaction vertex of the event needs to be known. While the vertex position perpendicular to the beam-axis is limited due to the small diameter of the beams to below a $100\mu\text{m}$, the z -vertex position needs to be reconstructed with the help of the tracks in the central detector region, because the interaction region has a length of about half a metre. To reduce beam-gas background events or events due to an interaction of one of the beams with the beam-pipe, which can happen along the whole length of the detector and beyond, only vertex positions close to the nominal vertex of the run are taken into account:

$$z_{\text{vtx}} = z_{\text{vtx,actual}} - z_{\text{vtx,nominal}}(\text{run}) \quad , \quad -30\text{ cm} < z_{\text{vtx}} < 30\text{ cm} \quad . \quad (5.7)$$

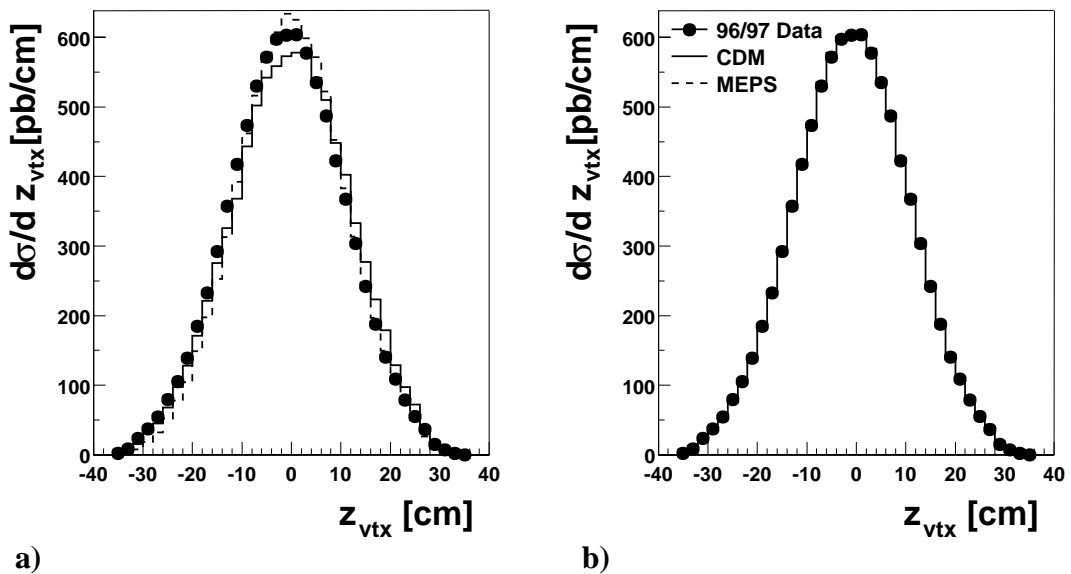


Figure 5.3: Description of the z_{vtx} distribution a) before and b) after reweighting.

The resulting z_{vtx} -position of the events and the description by the Monte Carlo simulations is shown in figure 5.3a. To improve the description of the z_{vtx} -position of the data events by the Monte Carlos, a reweighting of the Monte Carlo data samples was done. The resulting distributions are shown in figure 5.3b.

5.3.3 The Energy Balance

A measure for the energy balance and longitudinal momentum of an event is the so-called “ $E - p_z$ ”-quantity which is defined using the four-vector of the electron $k_e = (E_e, p_x, p_y, p_z)$:

$$E - p_z = 2E_e = E'_e (1 - \cos \theta'_e) + \sum_{i \in \{\text{had. objs.}\}} E_i (1 - \cos \theta_i) \quad . \quad (5.8)$$

Here, E_e is the energy of the beam electron. In the years 1996 and 1997 the electron beam had an energy of 27.5 GeV such that the electron four-momentum is $k = (27.5, 0, 0, -27.5)$ GeV, which results in $E - p_z = 55$ GeV.

This theoretical value can only be reproduced in the measurement, if all hadronic particles are detected and their energies correctly measured. Hadrons, which leave the detector through the beam pipe in the forward direction, contribute only little to $E - p_z$, because their z -component of the momentum is approximately equal to their energy. The quantity $E - p_z$ is, however, very sensitive to particle losses in the backward region. Therefore, a lower limit of $E - p_z$ can efficiently reduce photo-production events where the scattered electron is not measured (see also section 5.2). Beam induced background due to interactions with the beam-pipe or the remaining gas can be reduced by applying an upper limit on $E - p_z$. In the analysis,

$$35 \text{ GeV} < E - p_z < 70 \text{ GeV} \quad (5.9)$$

is required. The description of the energy balance by the standard DIS Monte Carlo generators is studied in section 5.4.2.

5.3.4 Cuts on the Properties of the Scattered Electron

The background induced by photo-production events can be efficiently reduced by applying cuts on the properties of the electron candidate. A way to discriminate DIS events against photo-production background is to require the cluster of the electron candidate in the SpaCal calorimeter to have a small transverse extent. Hadronic showers normally tend to be broad. Therefore, a cut on the cluster radius $r_{\text{cluster}} < 4$ cm is applied to reduce the probability to misidentify hadrons as an electron.

An additional reduction of the background can be achieved by linking the track in the backward tracker BDC to the cluster in the SpaCal and by requiring the distance between the track extrapolated into the calorimeter and the cluster of the electron candidate in the calorimeter to be smaller than 3 cm. This linking is only done, if a track is found in the BDC.

During the data taking in 1996 and 1997, the inner region (CIET) of the SpaCal had a very high trigger rate, probably due to synchrotron radiation. Since the electron is only scattered into this region for very low values of Q^2 , this region can be safely excluded from this analysis [80]. In addition, some of the trigger cells in the outer part of the SpaCal did not

work well during long run-periods and have therefore been taken out of the fiducial region for the electron in the SpaCal (for a list of the regions, see [80]). About 1.3%, i.e. 5813 events, of the total number of events are cut away by these two last cuts.

5.3.5 Track Selection

In this analysis only tracks in the central trackers of the H1 detector are taken into account. The tracks have to have a polar angle of at least 20° and at most 160° . The transverse momentum of the tracks has to be higher than 150 MeV. To clearly identify a track, a minimum track length is required. Tracks with a polar angle smaller than 150° have to have a length of at least 10 cm, for the rest of the tracks 5 cm is sufficient. Primary tracks, i.e. tracks that come from the interaction vertex, have to have a reconstructed distance of closest approach (DCA) to the interaction vertex of less than 2 cm and need to start at most at a radius of 50 cm away from the vertex.

During the 1997 data taking period, the efficiency of several wires of the CJC was degraded due to depositions of dirt in one radial segment. The Monte Carlo description of this region is poor, therefore this part of the tracking chamber was removed from the analysis in both data and Monte Carlo simulations by a cut on $-160 < \phi < -80$. Since the 1997 data are the majority of the overall data studied, this was done for simplicity for the entire data set.

In the 1997 data taking period another problem occurred, which was found in 2001: The data readout of the CJC was not always able to assign the correct event-number to tracks that were digitised. This led to fragments of tracks missing in the event or additional track fragments appearing. The influence of this on an analysis depends, however, on the track selection criteria. Although it is possible to ignore the parts of the runs in which this problem occurred, this was not done, because of the loss in data. Instead, it was checked that by using only good runs, the outcome of the analysis does not change. Also, the description of the distributions of the polar and azimuthal track angles are equally good for both cases as is shown in figure 5.4.

5.4 Description of the Data by Standard DIS-Models

After the kinematic cuts and the cuts necessary to ensure a high data quality, 374596 events are found in the data, corresponding to an integrated luminosity of 21.1 pb^{-1} , of which 16.3 pb^{-1} were taken in the year 1997. In the following, the description of the inclusive DIS data sample by the two standard DIS Monte Carlo generators CDM and MEPS will be checked.

5.4.1 Description of the Electron Distributions

Figure 5.5 shows a selection of control variables characterising the scattered electron and the distribution of the kinematic variables. The cross-sections shown are not corrected for detector migrations and are simply the number of measured events divided by the luminosity. The Monte Carlo simulations have been reweighted with respect to the measured z_{vtx} . In

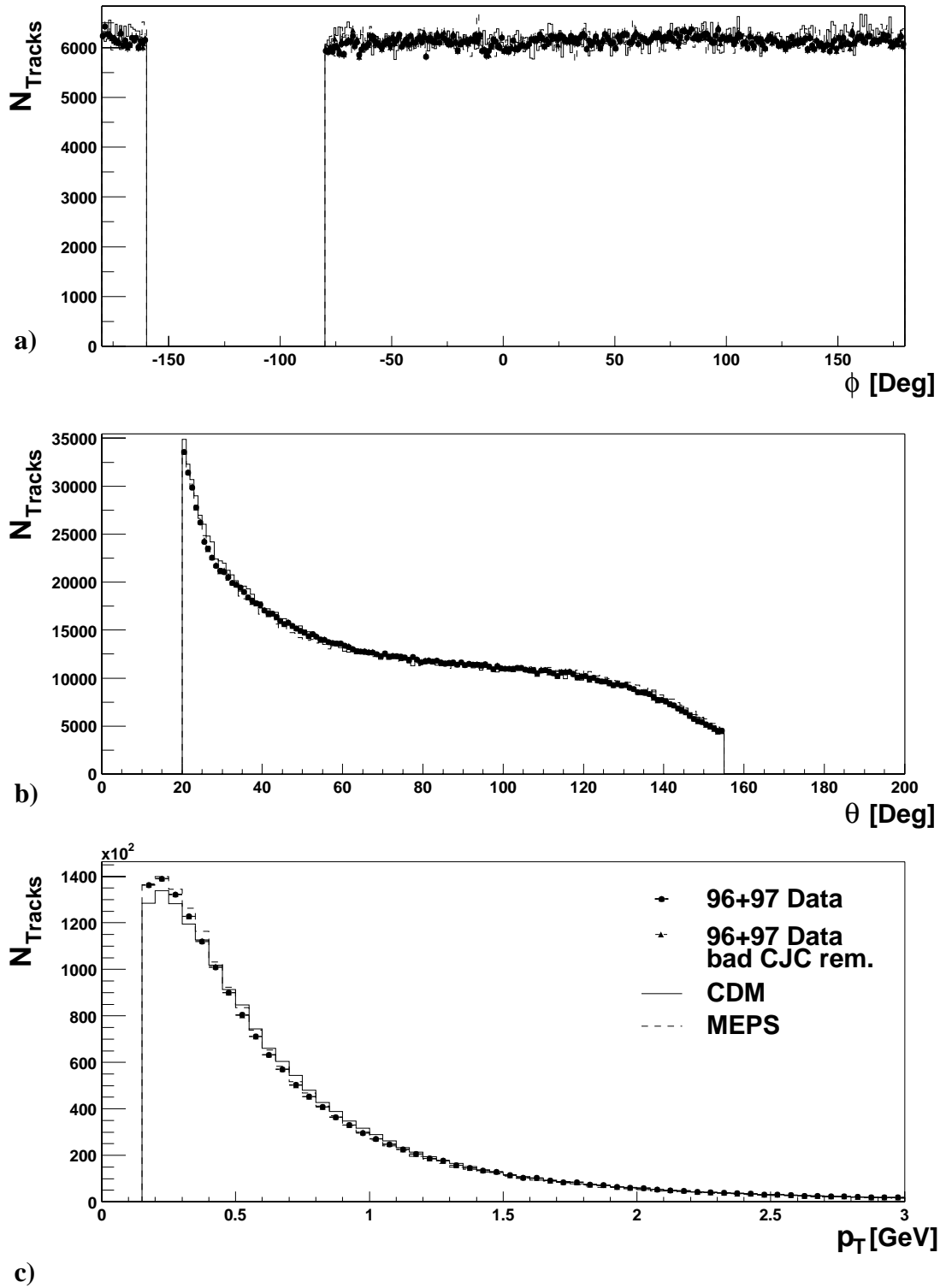


Figure 5.4: The distributions of the angles ϕ and θ of the tracks and the transverse momentum distribution of the tracks in the data compared to the two DIS Monte Carlos CDM and MEPS after z_{vtx} reweighting. In addition, the data are shown with those parts of the runs removed, which were affected by the 1997 CJC event mixing problem (see text).

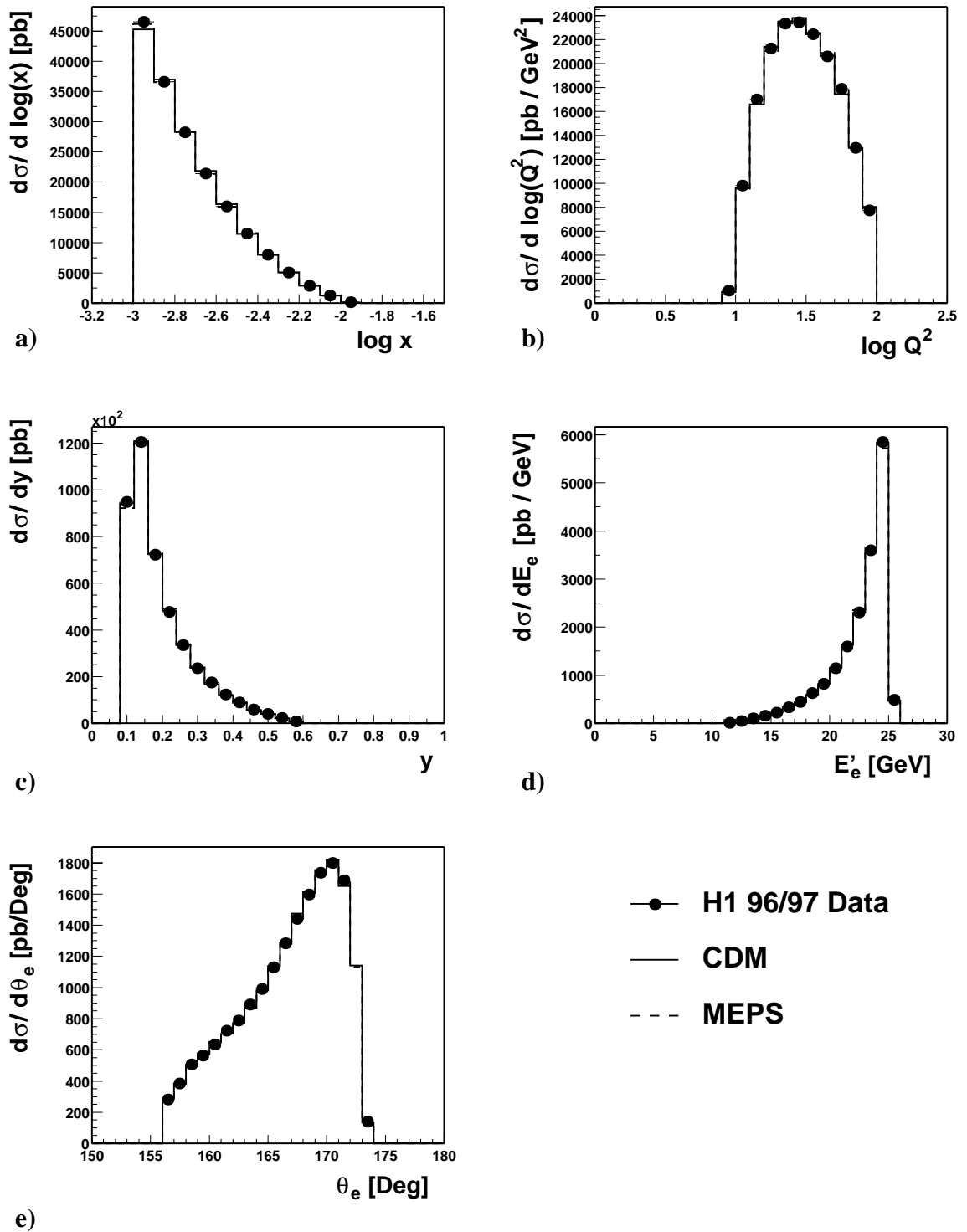


Figure 5.5: Control plots of kinematic variables characterising the description of the scattered electron after z_{vTX} reweighting. Shown are the data as dots and the CDM (full line) and MEPS (dashed) Monte Carlo simulations. In a) the logarithm of the Bjorken variable x is shown, in b) the logarithm of the scaling variable Q^2 . Plot c) shows the inelasticity y and d) and e) the energy E'_e and polar angle θ_e of the scattered electron.

addition a reweighting of the structure function F_2 used by the Monte Carlo simulations to the F_2 determined by a recent H1 measurement was done. The description of the data by the two Monte Carlo models is good and the overall normalisation is correct within 2%.

5.4.2 Description of the Hadronic Final State

The hadronic final state of events in this analysis is described by hadronic final state objects that combine calorimeter information with information from the tracking system. These hadronic final state objects will later be used to e.g. identify the current jet of instanton-induced processes or to classify the final state of the instanton subprocess. A good description of the hadronic final state objects by the standard DIS Monte Carlo generators is therefore essential for the analysis.

Different methods exist to define hadronic objects using calorimeter and track information. Throughout this analysis FSCOMB [83] objects will be used. It has been shown that FSCOMB objects provide a good description of the hadronic final state, particularly of the properties of jets (for an overview see e.g. [80]).

FSCOMB Hadronic Final State Objects

FSCOMB hadronic final state objects combine the calorimeter information with the information of low momentum tracks [83]. This allows to take particles with low momenta ($\lesssim 200\text{MeV}$) into account, which do not reach the calorimeter due to the magnetic field in the detector and the amount of dead material in front of it. The energy resolution of the tracking system is also better than that of the calorimeter for these low momentum particles. In the FSCOMB method, all central tracks with transverse momenta $p_t < 2\text{GeV}$ are used. Forward tracks are not taken into account in this analysis. The tracks are extrapolated to the calorimeter surface and a cylinder with a radius of 25 cm in the electromagnetic and 50 cm in the hadronic part of the calorimeter around the track is defined. The energy deposited in the calorimeter within this cylinder is then summed up and compared to the energy of the associated track. If the energy of the track is larger, the energy deposited within the cylinder is neglected and the FSCOMB object is built from the track information, in the other case, only the calorimeter information is used. This prevents double counting of objects and compensates for the loss of energy in the dead material in front of the calorimeter. Finally, the remaining calorimeter clusters are added to the list of final state objects, with the exception of the identified scattered electron.

The quality of the reconstruction of the hadronic final state and the description by the Monte Carlo simulations can be checked by looking at the p_t -balance of the events (the ratio of the vectorial sum of all transverse momenta of the hadronic final state objects to the transverse momentum of the scattered electron $p_{t,\text{had}}/p_{t,\text{el}}$) and the $E - p_z$ quantity defined in (5.8). The $E - p_z$ distribution is shown in figure 5.6a for the data and the CDM and MEPS Monte Carlos. The mean value for the data is at 53.3 GeV which is close to the expected value of 55 GeV. The mean values are 53.8 GeV for CDM and 53.5 GeV for MEPS, both being in good agreement with the data. The description of the distribution of the data for the $E - p_z$ distribution by the Monte Carlo generators is sufficiently good. The asymmetry of the $E - p_z$ distribution is attributed to QED radiation.

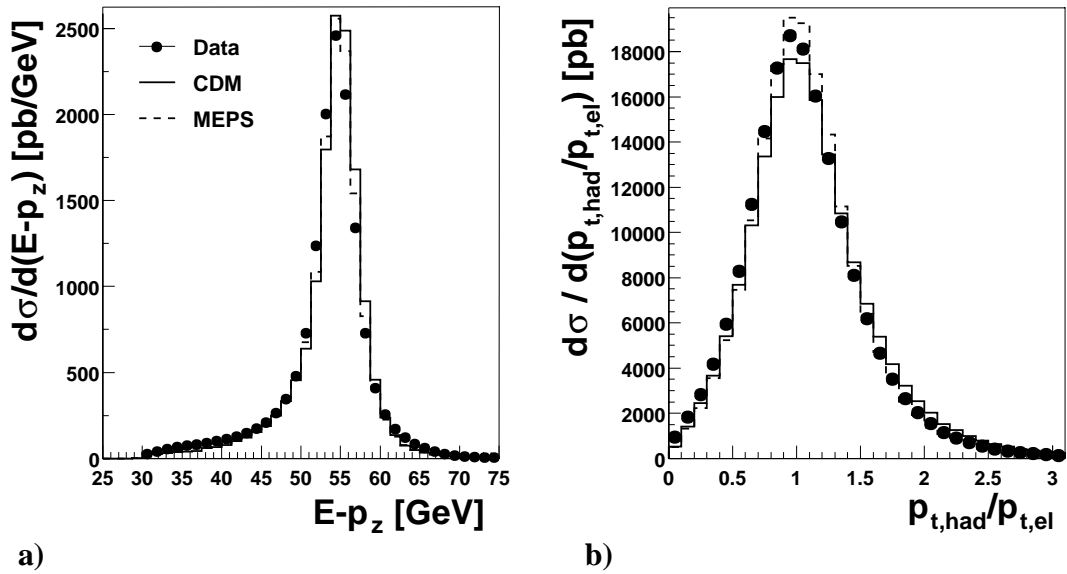


Figure 5.6: Description of the $E - p_z$ and $p_{t, \text{had}}/p_{t, \text{el}}$ distributions by the CDM and MEPS Monte Carlo simulations after z_{vtx} reweighting.

In figure 5.6b the balance of the transverse momentum of the electron $p_{t, \text{el}}$ and the total transverse momentum of the hadronic final state objects is shown. The mean of the distribution of the data events is 1.05, which is close to the theoretical value of 1 and for the distribution of the CDM and MEPS models it is 1.13 and 1.08 respectively. The Monte Carlo simulations describe the p_t -balance of the events over the whole range plotted.

With the application of the cuts described above, a sample of inclusive DIS events with a high quality and which is well described by the Monte Carlo simulations has been collected. In the following chapter, this data sample will be searched for instanton-induced events.

Chapter 6

The Experimental Search

In this chapter, the search for instanton-induced events using the 1996 and 1997 DIS data taken with the H1 detector is described. The strategy of the search is, to first identify suitable variables discriminating I-induced events from DIS background events and subsequently to employ two different discrimination methods to obtain a sample of events in the data with instanton-like characteristics as described by the QCDINS Monte Carlo model. For this sample of events, comparisons between the selected data and the standard DIS background models as well as the QCDINS predictions are made.

First, in section 6.1, a detailed introduction to the characteristics of I-induced events in deep-inelastic scattering from an experimentalist's point of view is given. Section 6.2 introduces the variables that discriminate between standard DIS background events and I-signal events. A detailed outline and discussion of the strategy of the search using the previously defined observables is given in section 6.3. The basic idea is to use only half of the characteristic observables to extract a subsample of instanton-induced events and to use the other observables to monitor the outcome. The systematic uncertainties of the variables, which are used to create the instanton-enriched sample, are studied in section 6.4. Both discriminating methods are described in sections 6.5 and 6.6, which also includes a comparison of data to the standard DIS background models. A discussion and comparison of the results is finally done in section 6.8.

6.1 Hadronic Final State in Instanton-Induced Processes

The search for instantons described here, is entirely based on the hadronic final state of instanton-induced events as modelled by the Monte Carlo simulation program QCDINS [14]. The characteristics of the simulated events, which may be exploited to discriminate events modelled by QCDINS against normal DIS background events, have been already described in sections 1.5 and 4.2 from a more theoretical point of view. However, since a detector always has limited resolution, acceptance and efficiency, not all the characteristics are easily utilised in an experimental search. In this section, the experimentalist's point of view shall motivate the implementation of the search.

The topology of a typical event simulated by QCDINS is shown in figure 6.1a, where the transverse energy E_t in the hadronic centre-of-mass system (hCMS, the frame of reference,

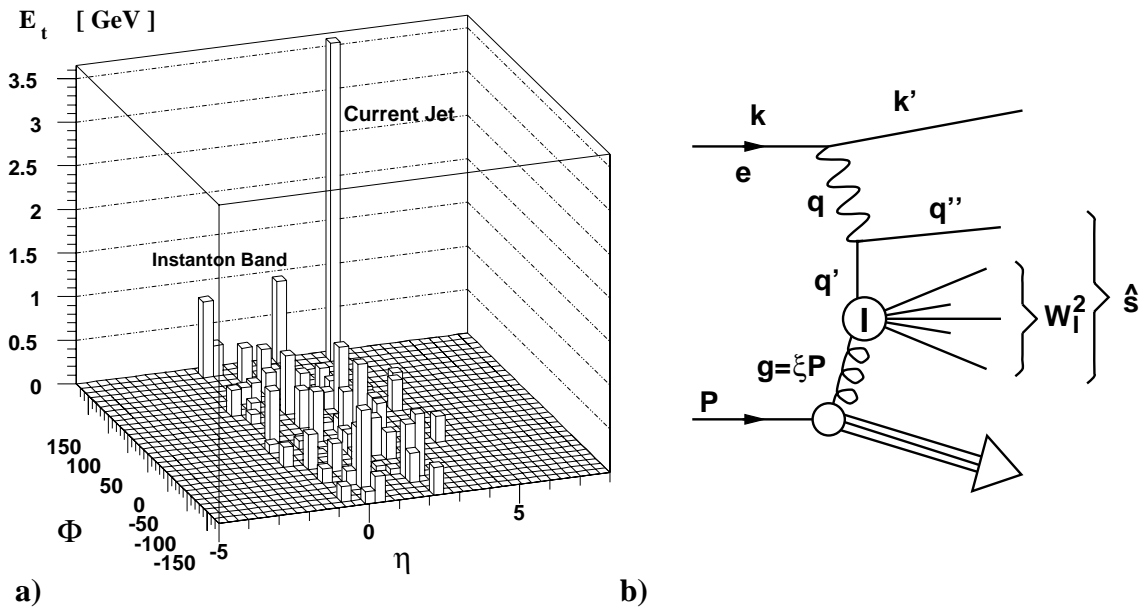


Figure 6.1: The topology of an instanton-induced event in the hadronic centre-of-mass frame is shown in a) as the transverse energy E_t of the produced hadrons deposited in bins of the $\eta - \phi$ -plane, where η is the pseudo-rapidity and ϕ the azimuth. In b) the diagram of the process is shown as a reminder.

where $\vec{q} + \vec{P} = 0$, see section 1.4) of the produced hadronic final state objects is shown in bins of the azimuth ϕ and the pseudo-rapidity η . The pseudo-rapidity η is defined as $\eta := -\ln(\tan(\theta/2))$. In the hCMS the forward part of the detector is mapped towards negative η . The $\eta - \phi$ -plane shows the transverse energy of the hadrons produced in the instanton-band around $\eta = 1$ and the current-jet of the instanton-induced event. Figure 6.1b shows the Feynman-like diagram of the instanton-process as a reminder. Another event is displayed in figure 6.2, where the simulated response of the H1 detector is depicted. A relatively hard jet can be seen. In addition to the current jet a band of hadrons is spread over almost the whole azimuthal angle.

Two peculiar features can therefore be easily identified in the E_t -map and the sketch of the detector. They are:

A jet with modest E_t in every event produced by the current quark, which is generated in the splitting of the virtual photon $\gamma^* \rightarrow q\bar{q}$ and is the one not entering the instanton subprocess. The jet has a typical transverse energy in the hCMS of $E_{t,\text{Jet}} \approx 4 \text{ GeV}$.

A band of hadrons with high E_t in the event homogeneously distributed in azimuth, which is generated by the particles produced by the instanton “decaying” isotropically in its rest frame. This isotropy manifests itself on the hadron level as a band of hadrons in hCMS with similar E_t due to the large number of particles produced in the instanton “decay”. Events simulated with QCDINS have transverse energies of up to 10 GeV per unit of rapidity [15] in the region of this band of hadrons, while standard deep-inelastic

scattering events produce on average only 2 GeV per unit of rapidity [85]. Many of the produced hadrons are charged. Since $2n_f - 1$ quarks are produced by the instanton decay and in addition $\langle n_g \rangle^I \approx 1/\alpha_s \approx 3$ gluons (see section 1.5) are emitted, the mean number of partons produced is 10 [10] and the number of charged particles (also called “multiplicity”) after the hadronization is approximately 20. The band is expected to have a width of 2.2 units of rapidity [10].

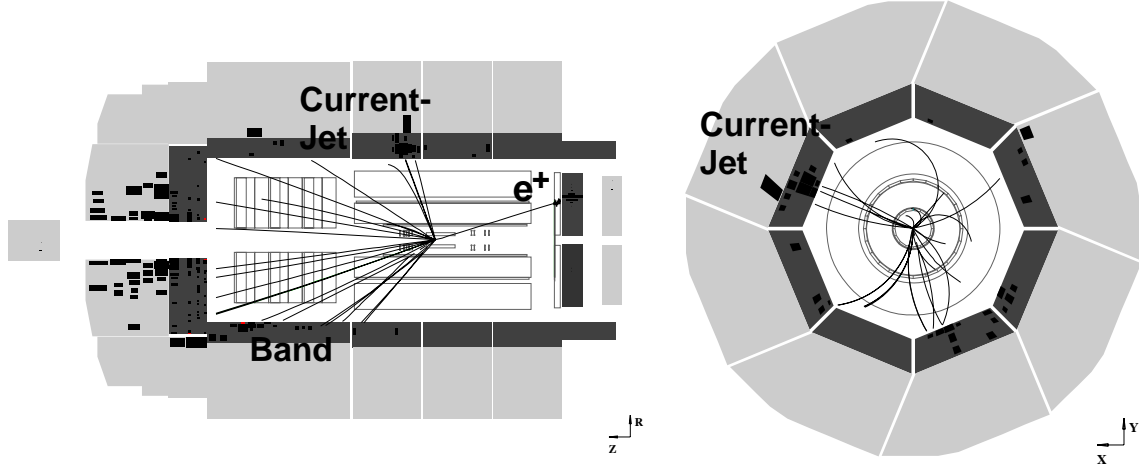


Figure 6.2: The simulated response of the H1 detector to a Monte Carlo generated instanton-induced event with typical kinematics $x' = 0.49$, $Q'^2 = 130.7 \text{ GeV}^2$, $x = 3.28 \times 10^{-3}$ and $Q^2 = 56 \text{ GeV}^2$. This figure shows a different event from the one in figure 6.1.

Two other features of instanton-induced events mentioned in section 1.5 are not as easily exploited experimentally. This is the production of strange mesons and baryons in every instanton-induced event and the chirality violation.

To detect strange particles, particle identification is necessary. The most abundant strange particles are kaons, mesons which contain strange or anti-strange quarks and in addition u or d quarks. Charged kaons K^\pm can be identified by their characteristic energy loss in the tracking chambers. The typical efficiency for charged kaon identification in a limited region of the transverse momentum of the tracks is 25% [86]. Neutral kaons exist in two varieties called K_S^0 and K_L^0 , which are CP -violating superpositions of the CP -eigenstates K_1^0 and K_2^0 . The mean decay length of K_L^0 is larger than the radius of the tracking system ($c\tau \approx 15.5 \text{ m}$) of the H1 detector so that these particles can usually not be identified. However, the K_S^0 ($c\tau \approx 2.7 \text{ cm}$) can be identified, if it decays into charged pions (in 64% of the cases) within the detector’s central region ($|\eta| < 1.3$) with an efficiency of $\approx 40\%$ [87].

Strange mesons can also be produced in standard DIS events, and in case of events with high multiplicity it is also quite likely that strange particles are produced in the fragmentation process. In instanton-induced events typically a large number of (charged) particles is produced, such that the strangeness production is not much larger than in the case of high multiplicity background events. In the case of at least 12 charged particles produced

and requiring at least one K_S^0 in the final state, only about 40% more K_S^0 are expected in instanton-induced events compared to standard DIS events [15, 84].

Both, the low efficiency for detecting strange particles and the expected high strangeness production in high multiplicity normal DIS events, make a discrimination of instanton-induced events based on an identification of strange mesons or baryons not very promising and it was not pursued in this search.

Since chirality is conserved in perturbative QCD, detecting the violation of chirality in a selected sample of DIS events would provide strong evidence for instanton-induced events. However, measuring chirality can only be done on event samples by exploiting the angular distribution of the decay particles using certain “self-analysing” decays of strange baryons. An outlook on the prospects of such a search is given in [88].

Neglecting the increased strangeness production and chirality violation, the search will be based on the typical kinematics of instanton-induced events and the expected high isotropy of the instanton decay products in the rest-frame of the instantons.

6.2 Characteristic Instanton Variables

The discriminating variables used in this analysis are a mixture of variables which approximately reconstruct the characteristic kinematical properties of the instanton subprocess, as well as observables which characterise the instanton final state. Several of them have been studied using Monte Carlo generated events without the detector simulation step [15, 84] to identify those with the highest combined discriminating power. However, in these studies the limited resolution and acceptance of the detector and the relatively low efficiency for detecting strange particles was not taken into account. This makes it necessary to re-investigate these proposed observables and also to partly redefine them such that they are less affected by uncertainties introduced by the detector. In the following, first the reconstruction of the kinematic variables of the instanton subprocess is described before the definition of all the characteristic instanton-observables is given. The description of the distributions of these observables in the data by the standard DIS Monte Carlo models is then studied. Finally, the sensitivity of these observables to the two hadronization models of the QCDINS Monte Carlo simulation is analysed.

6.2.1 Reconstruction of the I-Subprocess Kinematics and the I-Band

To define the reconstructed kinematical variables of the instanton subprocess and the observables characterising the final state of the I-subprocess, the following procedure was used:

1. Identify the scattered electron and calculate the photon four-momentum vector q by exploiting (see section 1.5)

$$q = k - k' \quad . \quad (6.1)$$

2. Make a list of all hadronic final state (FSCOMB-) objects (see section 5.4.2) and Lorentz-boost all objects into the hadronic centre-of-mass system, defined by $\vec{q} + \vec{P} = 0$ (see figure 1.8). Only objects in the range $-1.4 < \eta_{\text{lab}} < 2$ are taken into account. This restriction is justified by the distribution of the transverse energy flow per event and

unit of pseudo-rapidity η shown in figure 6.3 for the data, the CDM and MEPS background simulations and the QCDINS simulation in the laboratory frame. Whereas the MEPS model gives an excellent description of the data over the full η -range, the description by CDM of the forward region starting at $\eta \gtrsim 1$ is not very good. Here, higher E_t values are predicted by CDM than found in the data. However, also the CDM model follows the shape of the data distribution introduced by the properties of the detector. The upper cut on η_{lab} ensures the forward part of the LAr Calorimeter is cut away, where the description by CDM is poor. Moreover, for larger η_{lab} in case of the instanton Monte Carlo the transverse energy flow is probably not produced by the I-band or current jet, but by soft partons emitted between the I-band and the proton remnant. The simulations of these partons is anyhow doubtful, since it is not clear if the concept of parton showers can easily be transported to I-events. In the region $\eta < 2$ the energy flow associated with the I-band and current jet can be seen in the distribution of QCDINS. The cut $\eta_{\text{lab}} > -1.4$ is located at the backward edge of the LAr calorimeter.

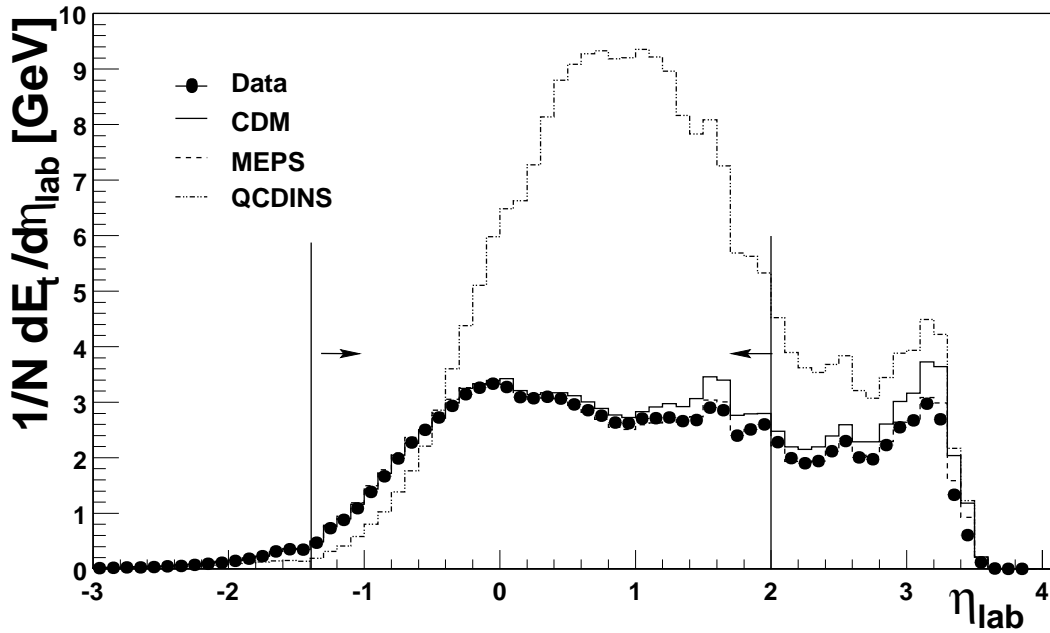


Figure 6.3: The transverse energy flow per event and per unit of η of the data, the CDM and MEPS Monte Carlo background simulations in the laboratory frame. Cuts are applied at $\eta = -1.4$, corresponding to $\theta = 152^\circ$ and at $\eta = 2$ ($\theta = 15^\circ$). In addition, the prediction of the instanton simulation is shown.

3. Find the highest E_t jet. The current jet is defined to be the jet with highest transverse energy E_t in the event. The CDF-CONE jet algorithm¹ [89, 90] is used with a cone radius of $R = 0.5$ and requiring a minimum transverse energy of the jet of $E_{t,\text{Jet}} \geq$

¹In a simplified way, the cone algorithm works as follows: First a distance measure is defined by $r = \sqrt{(\Delta\eta)^2 + (\Delta\phi)^2}$ in the $\eta - \phi$ -plane. All momentum vectors of the hadronic final state objects within a cone

1 GeV. The sum of the four-momenta of the objects identified by the jet algorithm as belonging to the jet is defined to be the reconstructed four-momentum of the current quark q''_{rec} . Using the identity $q = q'' + q'$, the reconstructed four-momentum squared of the quark entering into the I-subprocess is defined to be

$$Q_{\text{rec}}'^2 = -q_{\text{rec}}'^2 := -(q - q''_{\text{rec}})^2 \quad . \quad (6.2)$$

Comparing the direction of the identified current jet with the direction of the current quark for QCDINS simulated events, one finds that the current jet is correctly identified in about 70% of the cases. Several different procedures of reconstructing Q'^2 have been studied, including variation of the parameters of the cone algorithm or even to identify the band of hadrons produced by the I-transition first. A discussion on the ways to reconstruct Q'^2 , the quality of the reconstruction of Q'^2 and ways to reconstruct x' is presented in chapter 7. If no jet is found, $Q_{\text{rec}}'^2 \equiv Q^2$, but the event is later neglected in the search for instantons.

4. Remove the hadronic final state objects found by the jet algorithm in the previous step from the list of all hadronic objects.
5. Reconstruct the instanton band. Again, several strategies were studied. The iterative procedure described below was chosen due to its insensitivity to the remaining relatively poor description of the energy flow by the CDM Monte Carlo in the forward detector region (see figure 6.3). This has been explicitly checked by changing the acceptance cut in η_{lab} and studying the change of the observable distributions for the two Monte Carlo simulations and the data. The band is defined to have a width of ± 1.1 units in η centred around a mean $\bar{\eta}$ which is defined iteratively by the following procedure:
 - (a) Fill the transverse energy of all hadronic objects into a histogram in $\eta \in [-5, 5]$ with bins of $\eta = 1/3$. $\bar{\eta}_0$ is given by the middle of the bin containing the highest E_t .
 - (b) Iterate the mean pseudo-rapidity $\bar{\eta}_i$

$$\bar{\eta}_i = \frac{\sum E_{t,h} \eta_h}{\sum E_{t,h}} \quad , \quad (6.3)$$

where the sum is over all hadronic final state objects with transverse energy $E_{t,h}$ in the band given by $\eta \in \bar{\eta}_{i-1} \pm 1.1$, until

$$|\bar{\eta}_i - \bar{\eta}_{i-1}| < 0.01 \quad . \quad (6.4)$$

with radius R around a seed axis are summed up. The E_T weighted mean of η and ϕ of the objects then becomes the new jet-axis. The procedure is iterated until the jet-axis ceases to change. The jet is kept, if the transverse energy exceeds a minimum $E_{t,\text{min}}$. In this case, the same procedure is repeated for the remaining hadronic final state objects.

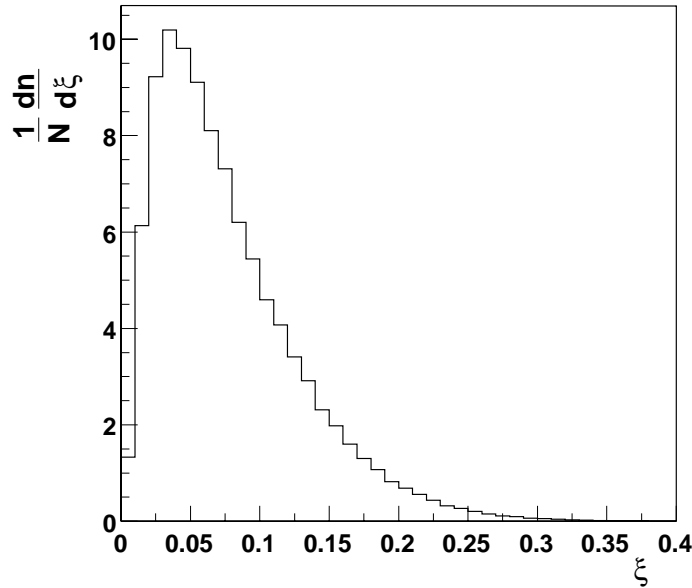


Figure 6.4: The distribution of the longitudinal momentum fraction ξ of the gluon momentum with respect to the proton momentum which enters into the instanton subprocess. The distribution generated by QCDINS is peaked at $\xi \approx 0.05$ and has a mean of $\bar{\xi} \approx 0.076$.

6. Boost all hadronic final state objects within the instanton band region into the approximated I-rest frame. Boosting into the rest-frame of the instanton is crucial to characterise the final state of the instanton transition with shape variables, since the instanton “decay” is expected to be isotropic only in its rest-frame. The boost is defined by (see figure 1.8 for the definitions)

$$\vec{q}'_{\text{rec}} + \bar{\xi} \vec{P} = 0 \quad , \quad \text{with } \bar{\xi} = 0.076 \quad . \quad (6.5)$$

Here, $\bar{\xi}$ is the mean of the ξ distribution, which is produced by the QCDINS Monte Carlo generator, as shown in figure 6.4. The ξ distribution depends on the known structure functions of the proton as well as the kinematics of the perturbative I-subprocess and is characteristic only for the instantons modelled by QCDINS.

Strategies to boost into the rest-frame of the band identified in the previous step were also studied, but have the disadvantage of also forcing standard DIS events to be spherical, thus degrading the separation power of the shape variables.

7. Calculate shape variables and the charged particle multiplicity in the I-rest frame. The exact definition of these variables is given below, together with the definitions of the variables describing the kinematic properties of the instanton subprocess.

6.2.2 Definition of the Characteristic Instanton Variables

In the following, six variables are defined within the frames of reference described above. The variables are:

1. The sphericity of the I-band, Sph_B , is defined in the instanton rest-frame by

$$Sph := \frac{3}{2}(\lambda_1 + \lambda_2) \quad , \quad (6.6)$$

where $\lambda_{1,2}$ are the two largest eigenvalues of the diagonalised sphericity tensor defined by

$$S^{\alpha\beta} := \frac{\sum_i p_i^\alpha p_i^\beta}{\sum_i |p_i|^2} \quad , \quad (6.7)$$

using the four-momenta p_i of all hadronic objects associated with the I-band. The calculation of Sph_B is performed by the LUSPHE routine of the JETSET [73] program package.

2. The virtuality of the quark entering the I-subprocess, Q_{rec}^2 , is defined as in the above procedure (section 6.2.1).

3. The number of charged particles in the I-band, n_B is defined as the number of charged particle tracks as defined in section 5.3.5 within the region $\eta \in \bar{\eta} \pm 1.1$ of the instanton band.

4. The transverse energy of the band, $E_{t,B}$, is the scalar sum of the transverse energy of all hadronic final state objects in the band region. It is calculated in the hCMS.

5. The isotropy variable, Δ_B [91], which is calculated for all hadronic objects within the I-band, is defined as

$$\Delta_B := \frac{E_{in,B} - E_{out,B}}{E_{in,B}} \quad (6.8)$$

with the help of

$$E_{in,B} := \max_{\vec{i}} \sum_{\substack{h \in \text{Hadr. in} \\ \text{Band}}} |\vec{p}_h \cdot \vec{i}| \quad \text{and} \quad E_{out,B} := \min_{\vec{i}} \sum_{\substack{h \in \text{Hadr. in} \\ \text{Band}}} |\vec{p}_h \cdot \vec{i}| \quad , \quad (6.9)$$

where the maxima and minima are found by trying out all orientations of the unit-vectors \vec{i} and \vec{p}_h are the momenta of the hadronic final state objects in the instanton rest-frame. For pencil-like events (see figure 6.5), Δ_B is close to 1, because there exists an axis \vec{i} for which E_{out} , the sum of the projection on this axis of all momentum vectors of the hadronic objects, is small, while there also exist a different axis perpendicular to the one shown and parallel to the direction of the main axis of the event, where $E_{in} \gg E_{out}$. For isotropic events no such axis exists and $E_{in} \approx E_{out}$ for all axes \vec{i} , such that $\Delta \approx 0$.

6. The transverse energy of the jet, $E_{t,Jet}$, is defined in the hadronic centre-of-mass frame by adding up the four-vectors of all particles associated with the reconstructed current jet.

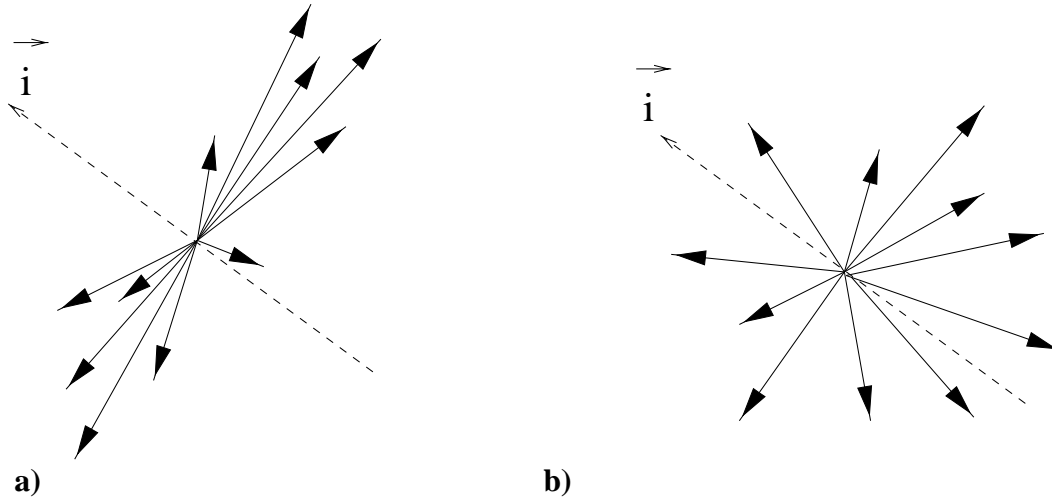


Figure 6.5: This sketch shows the momenta depicted by arrows of particles emitted from a single vertex for a pencil-like event (a) and an isotropic event in b). Also shown are the axes \vec{i} which are used in the definition of the isotropy variables E_{in} and E_{out} as given in the text.

6.2.3 Comparison of the Standard QCD Predictions with the Data

It has already been mentioned in the introduction of this chapter that half of the observables will be used to create a possibly instanton-enriched subsample of events and that the other half will be used to monitor the resulting sample. Therefore, the observables are studied here in two groups.

The distributions of the observables Sph_B , Q_{rec}^2 and n_B for the data, for the two standard DIS simulations and for the QCDINS Monte Carlo Generator are shown in figure 6.6a–c. The same distributions in a logarithmic scale are depicted in figure 6.7a–c. The overall description of the data by the CDM model is reasonably good; it describes the data within 10% except at very low and very high sphericity values, where a discrepancy of 20% is observed. CDM simulated events have a larger fraction of highly spheric events than are found in the data, while CDM undershoots the data in the region $Sph_B < 0.2$.

The MEPS Monte Carlo reproduces the data within 10–15%. However, at large multiplicities of the charged particles in the band, a discrepancy of up to 30% is found, since MEPS undershoots the data, as can be seen in figure 6.7c.

The other observables $E_{t,B}$, Δ_B and $E_{t,\text{Jet}}$ are shown in figures 6.6d–f and 6.7d–f. Here, the description of the data by the two standard DIS Monte Carlo models is slightly worse than for the previous observables. The Δ_B -distribution is described within 10–20% by both Monte Carlo models. For both transverse energy distributions $E_{t,B}$ and $E_{t,\text{Jet}}$, CDM and MEPS behave differently. MEPS overshoots the data in the range of small $E_{t,\text{Jet}} < 2.5 \text{ GeV}$ by 10%, while it has a softer tail towards higher $E_{t,\text{Jet}} < 10 \text{ GeV}$, where it is below the data by 20%. The tail of the distribution above 10 GeV is well reproduced up to the largest accessible values. The $E_{t,B}$ distribution is described by MEPS within 20%. CDM has a transverse energy spectrum, which is too hard for large transverse momenta in $E_{t,B}$ as well as

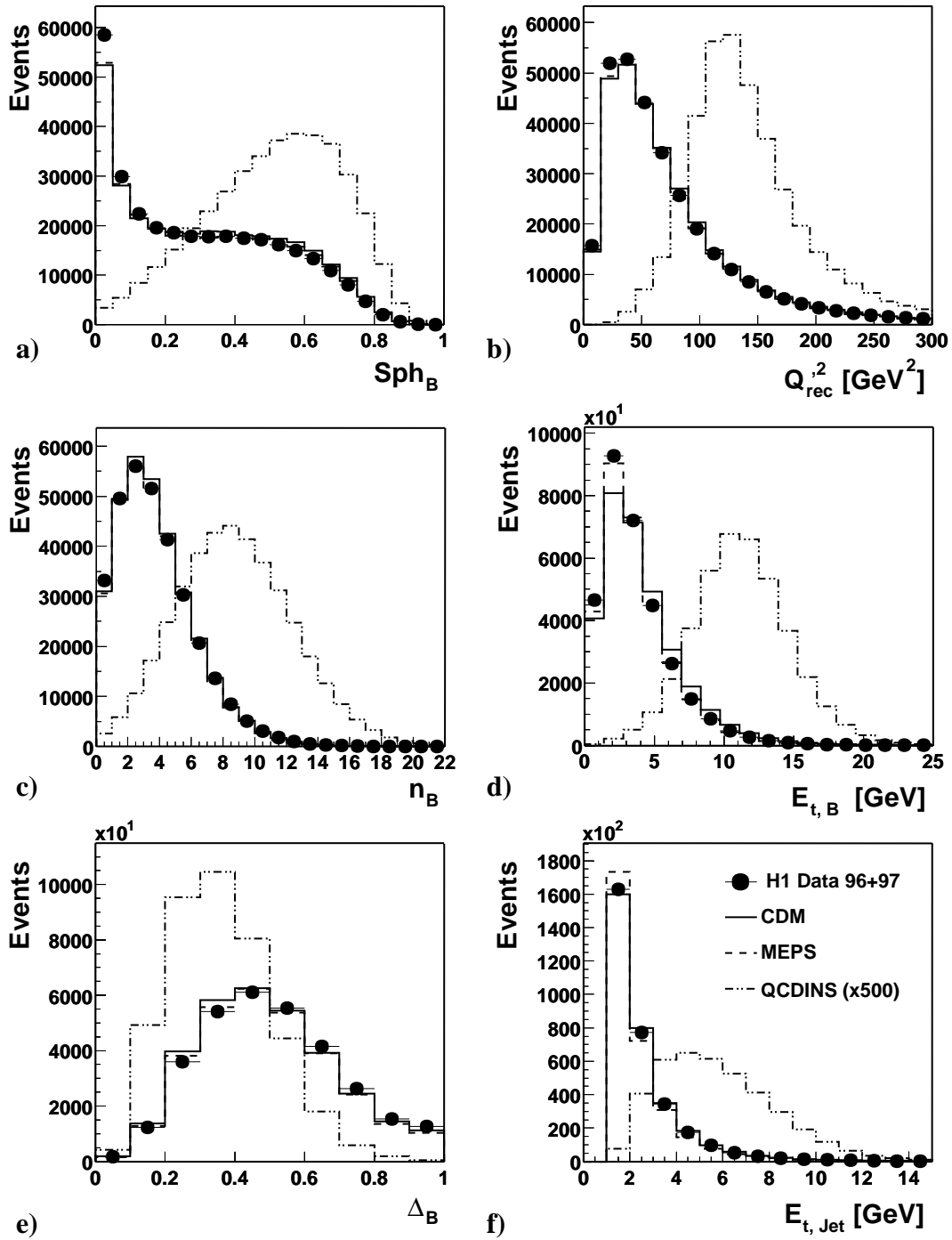


Figure 6.6: Distributions of the variables characteristic to instanton-induced events of the data and the two standard DIS Monte Carlo models CDM and MEPS. Also shown is the QCDINS model scaled by a factor of 500.

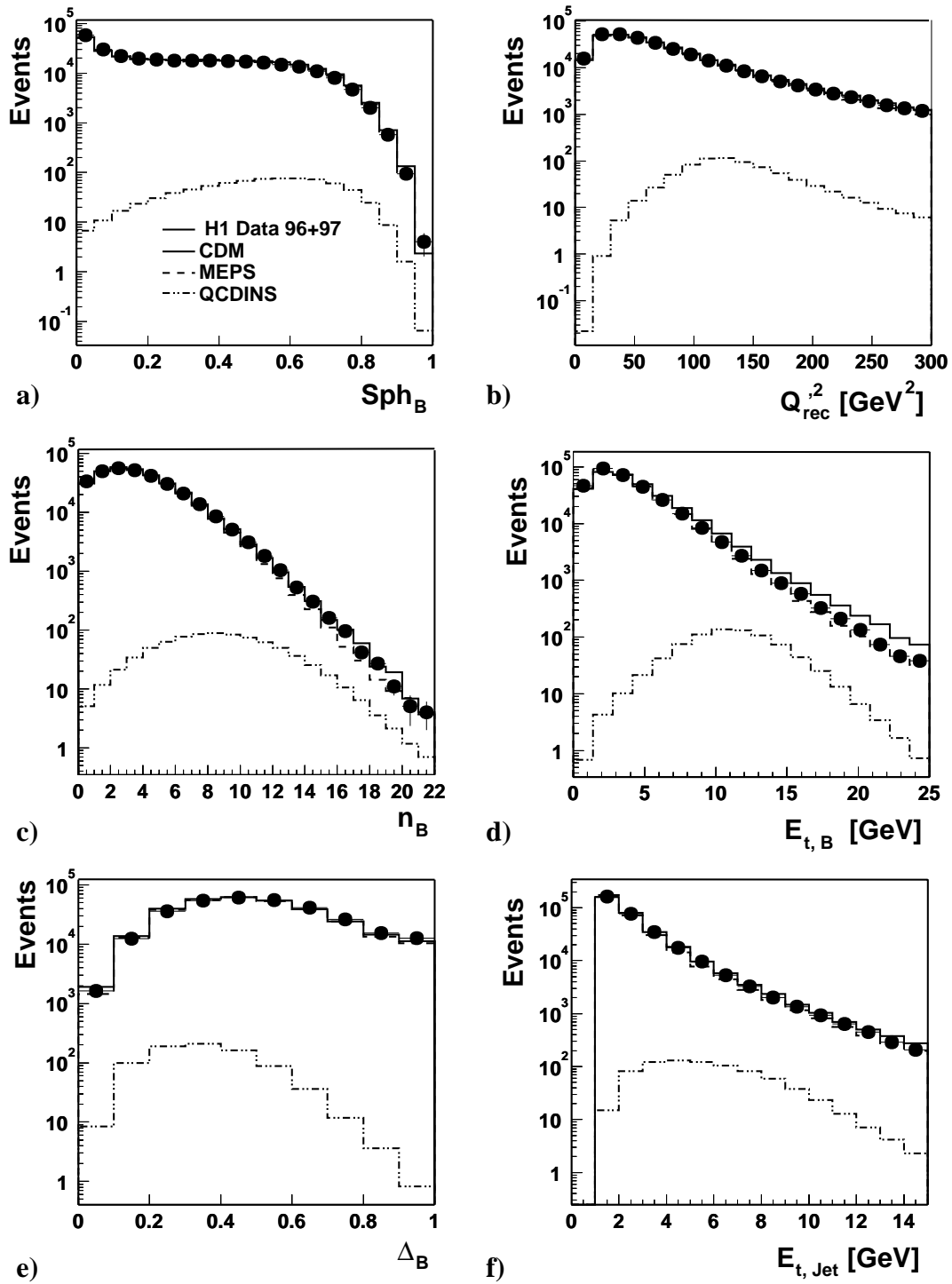


Figure 6.7: Distributions of the data, the two standard DIS background models CDM and MEPS, and the QCDINS Monte Carlo generator of the variables characteristic to instanton-induced events in logarithmic scale.

in $E_{t,\text{Jet}}$. For low $E_{t,\text{Jet}} < 10 \text{ GeV}$, CDM describes the data within 5–10%, but then exhibits an increasingly too hard spectrum towards higher $E_{t,\text{Jet}}$. This behaviour of CDM has also been observed in two-jet and three-jet production in DIS at HERA [92, 93, 94]. In the high $E_{t,B}$ -tail the discrepancy is even larger and for the highest accessible $E_{t,B}$ -values a discrepancy of 50% is seen. The overall description of the data by the MEPS Monte Carlo is better than the description by CDM.

The instanton prediction is shown as a dash-dotted line in figure 6.6 scaled up by a factor of 500 and in figure 6.7 unscaled but on a logarithmic scale. The instanton signal is about two or three orders of magnitude smaller than the standard DIS background. The distributions of the instanton-induced events are fairly distinct from the distributions of the standard DIS background. The sphericity Sph_B is peaked towards higher ($Sph_B \approx 0.6$) values, while the background distributions show a plateau and peak at 0. The reconstructed virtuality of the quark entering the instanton subprocess Q_{rec}^2 peaks towards $\approx 120 \text{ GeV}^2$, reflecting the steep rise of the instanton cross-section towards lower Q^2 , which is cut-off at $Q_{\text{min}}^2 \approx 113 \text{ GeV}^2$ due to the limits of instanton perturbation theory. Both, the transverse energy of the jet and the band, peak towards higher values compared to the background ($\langle E_{t,B} \rangle \approx 11 \text{ GeV}$ and $\langle E_{t,\text{jet}} \rangle \approx 5 \text{ GeV}$). The charged particle multiplicity as expected by the instanton model is also larger and the isotropy variable Δ_B is smaller compared to standard DIS events, due to the higher isotropy.

6.2.4 Influence of the Hadronization Model on QCDINS Events

Since the QCDINS Monte Carlo by default uses a different hadronization model than the standard DIS Monte Carlo generators, it is necessary to study what influence the hadronization has on the predictions of QCDINS. Figure 6.8 shows the variation of the three observables n_B , Sph_B and Q_{rec}^2 when using two different hadronization models, the cluster fragmentation model as implemented in HERWIG and the Lund String model as implemented by JETSET. In both cases, a simulation of the H1 detector was performed. As can be seen, the differences are small compared to the reference Monte Carlo CDM, i.e. the characteristics of the instanton process are not changed significantly. A detailed study on the effect of hadronization on the final state of QCDINS generated events with similar results was done in [15].

It needs to be noted, that it is not entirely clear, whether I-induced events actually hadronize in the same way as normal DIS events, since the energy density is very high. In the hadronic centre-of-mass frame, a transverse energy flow of up to 9 GeV per unit of rapidity is expected. This is about 4.5 times more than in standard DIS [85] (see also figure 6.3 which shows the energy flow in the laboratory frame). In addition, a large number of partons (≈ 10) is emitted from a small region of space-time of the size of the instanton [10].

It is not possible to test the other conceivable hadronization models. Possible candidates would be models used to describe heavy ion collisions. However, they are not yet available in the form of Monte Carlo simulation programs. Nevertheless, it is ensuring that the hadronization corrections to the chosen variables are not big. Therefore, it seems to be adequate to use a standard hadronization model.

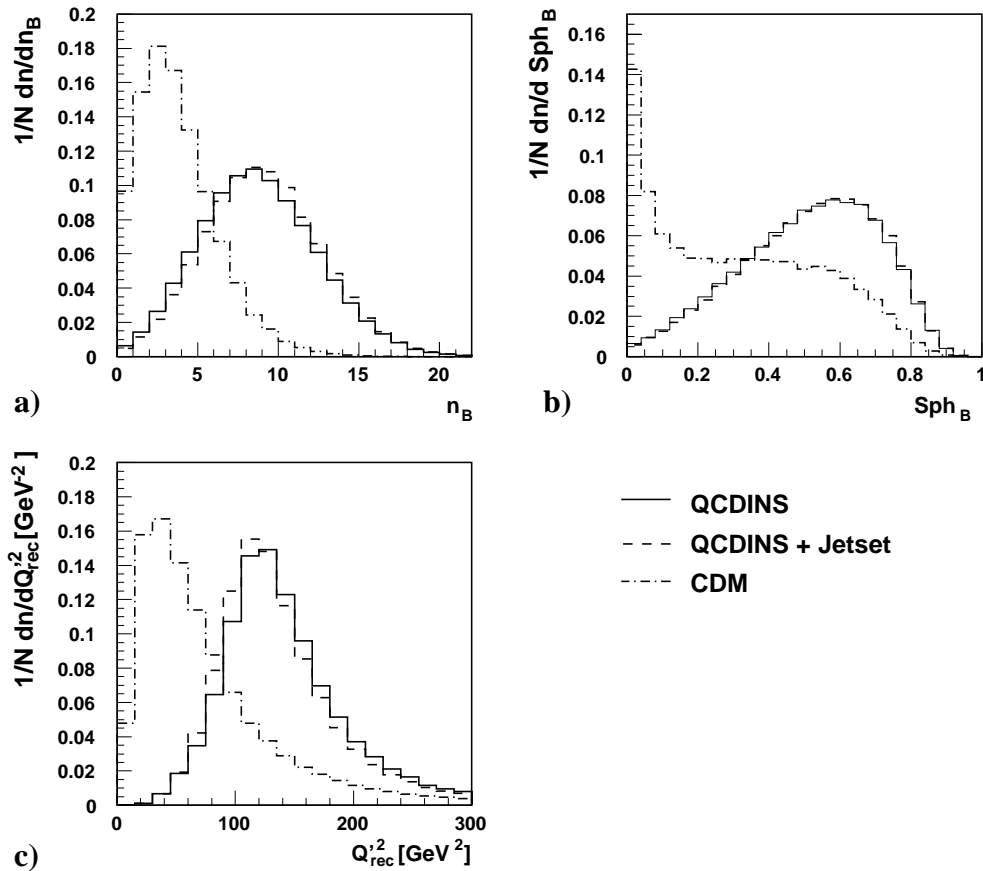


Figure 6.8: The change of three observables characteristic to instanton-induced events is shown when changing the hadronization routine in QCDINS from the default cluster fragmentation, as implemented in HERWIG to the Lund string fragmentation as implemented in JETSET. The three observables are the number of charged particles n_B in the I-band, the Sph_B and the reconstructed Q^2 of the process Q_{rec}^2 . As a reference, the CDM model is shown.

6.3 Search Strategy

In this section the strategy of the search for instanton-induced events is laid out and discussed in more detail.

Six observables characteristic for instanton-induced events have been defined in section 6.2. In the search three of these observables will be used to obtain a subsample of events which exploit different characteristics of instanton-induced events. Q_{rec}^2 , Sph_B and n_B are chosen, mainly because of the good description of the distributions of the data by the Monte Carlo simulations of the background. The other three variables ($E_{t,B}$, Δ_B and $E_{t,Jet}$) will be used to control the selection.

Using only half of the characteristic observables to extract a sample of instanton-like events, allows to use the other variables to monitor this sample. In addition, discrepancies

are seen in the description of $E_{t,B}$ and $E_{t,\text{Jet}}$ by the standard DIS Monte Carlo simulations. Moreover, the QCDINS prediction of both observables are also affected by unknown contributions of non-planar diagrams. Two other aspects shall also be mentioned. First, a cut-based method performs increasingly worse with a growing number of variables, as was pointed out in chapter 3, since the efficiency of the signal events decreases drastically. The second aspect is, that with a growing number of variables also the systematic uncertainty of the final result increases. In the extreme case, this can alleviate any gain from a higher separation power due to the increased number of variables entering the selection. This will be discussed in more detail in chapter 8.

Two different methods are used to select instanton events: a cut-based method which uses optimised cuts on the observables and a multivariate discriminant techniques as described in section 3.4. The decision to employ two independent methods was taken, because a multivariate method is expected to allow a better discrimination of events, while on the other hand multivariate methods are not yet widely used in high energy physics and therefore a cross-check by a more traditional method is requested by many physicists. The results of the method based on a combination of cuts is described in section 6.5. The search based on a multivariate discriminant employing the range searching technique is described in section 6.6.2.

The comparison of the standard DIS predictions with the data has shown, that the overall description of the three cut variables by the MEPS Monte Carlo generator is better than the description by the CDM model. Therefore, the MEPS simulation will be used to model the background in the search using the discriminant. The resulting cuts will then be applied to the CDM model and a comparison of the outcome will be done to the MEPS model.

Before the discrimination methods are employed, the systematic uncertainties of the observables used to create an instanton-enriched subsample of events are studied in the following section.

6.4 Systematic Uncertainties

In addition to the statistical error due to the limited number of events that were recorded or simulated, the search for instanton-induced events is also affected by systematic uncertainties. Systematic uncertainties can be due to model uncertainties of the employed Monte Carlo simulators, due to a bad description of the data by these model, or due to resolution effects of the measurement in the detector and limitations in the knowledge of the detector calibration. It is necessary to understand the effects of these uncertainties on the variables employed in this search in order to find the observables that are least affected and to assign a systematic error to the final result.

In the following, the effects of systematic uncertainties (to be discussed below) on the variables, characteristic for instanton-induced events and used to create the instanton-enriched sample of events, are studied. The relative variations of the observables are shown in figure 6.10 for the sphericity, figure 6.11 for the reconstructed Q_{rec}^2 , and in figure 6.12 for the number of charged particles in the band. Relative variation means the ratio of the MEPS Monte Carlo predictions where the properties of the hadronic final state objects and the tracks of the MEPS Monte Carlo after the detector simulation have been adjusted, to the

unchanged MEPS Monte Carlo simulation. In figure 6.13, the differences of the CDM and MEPS Monte Carlo Models are shown.

The following sources of systematic uncertainties were taken into account:

a) Hadronic energy scale in the LAr calorimeter: The uncertainty of the measurement of the hadronic energy scale in the LAr calorimeter is an important source for the systematic error. An estimate of the uncertainty that needs to be assigned can be obtained from the energy and momentum balance of the events. Figure 6.9 shows the $E - p_z$ and $p_{t,\text{had}}/p_{t,\text{el}}$ -distribution of the MEPS Monte Carlo and the data (see also section 5.3.3). The reconstruction of the energy by the LAr calorimeter was scaled by $\pm 4\%$ for the MEPS Monte Carlo. In most cases, the data points are contained between the two Monte Carlos, justifying the error of 4% that has been assigned to the LAr energy measurement. This is also the value used in a study on two jet [92] and three jet production in DIS [93].

Scaling the measurement of the hadronic energy has an impact of typically 5% on the reconstructed Q'^2 , since this quantity is defined using the reconstructed current jet and the hadronic objects in the I-band, both depending on hadronic objects defined with the LAr-Calorimeter.

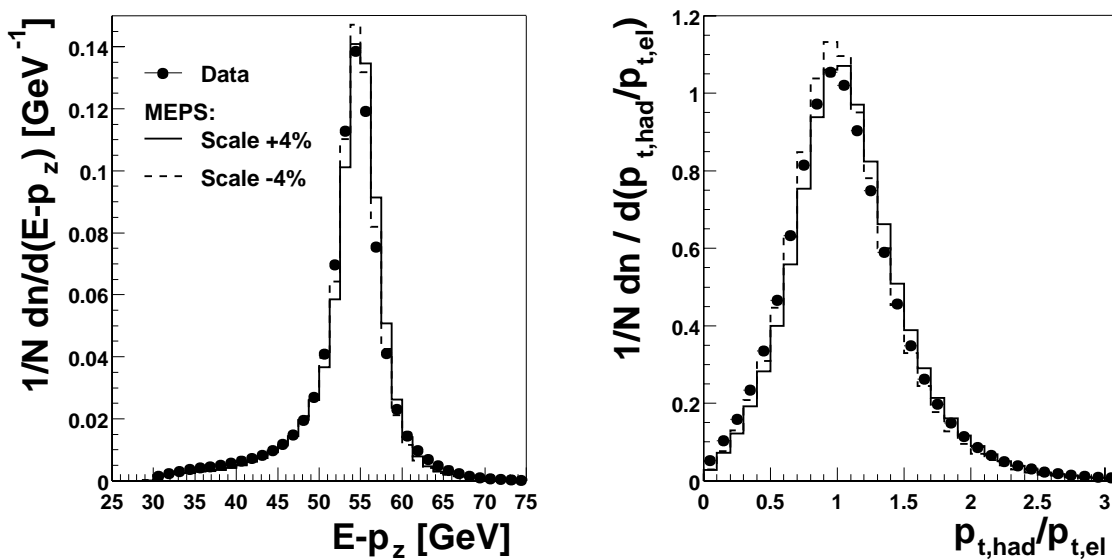


Figure 6.9: Comparison of the $E - p_z$ and $p_{t,\text{had}}/p_{t,\text{el}}$ distribution of the data with the MEPS Monte Carlo, where the energy scale of the LAr calorimeter was changed by +4% (full line) and -4% (dashed line).

b) SpaCal electron energy scale: An error of $\pm 1\%$ is assigned to the absolute energy measurement of the scattered electron in the SpaCal calorimeter. The error was obtained [95] by comparing the electron energy as measured in the calorimeter with the value

that was obtained with the double angle method, which is insensitive to the calibration of the calorimeter or an incomplete measurement of the hadronic final state [81]. All three variables used in the search are affected by 1–5%, with the sphericity being affected most, especially towards higher values.

- c) **Electron scattering angle:** The scattering angle of the electron is varied by ± 2 mrad [92]. Again, this quantity has an influence on the reconstructed kinematics of the event, which induces a change of about $\pm 3\%$ in all three instanton variables.
- d) **Track momentum scale in the hadronic final state objects:** The hadronic final state objects (FSCOMB-objects) used in this analysis are defined by track information as well as energy measurements in the calorimeters. The momentum of these tracks is rescaled by $\pm 3\%$ to account for systematic uncertainties [92], leading to a change of below 2% in all three observables.
- e) **SpaCal hadronic energy scale:** The SpaCal calorimeter not only measures the scattered electron, but in some cases also hadrons produced in the collision. This influences $E - p_z$ and the transverse energy of the particles found in the SpaCal. The hadronic energy scale is known up to $\pm 7\%$ [97]. The effects on the observables are very small and below 1%.

The following systematic uncertainties were assigned to the measurement of tracks, and only affect n_B :

- f) **Track momentum calibration:** The energy and momentum of the tracks were varied by $\pm 1\%$ [96], leading to a change of n_B of less than 3% for $n_B < 14$ and 7% for larger n_B .
- g) **Track azimuth angle:** Changing the azimuth of the tracks by up to ± 2 mrad [96] changes n_B by less than 1%.
- h) **Track polar angle:** By changing the polar angle, tracks may be moved out of the I-band, and thus the number of tracks in the band is affected by changing θ_{Track} by ± 2 mrad [96]. The induced uncertainty of n_B is less than 2% and grows towards small n_B .
- i) **Track efficiency:** The efficiency of finding a track well within the acceptance of the central tracking system of the H1 detector is known to be larger than 95% for tracks with $p_t < 250$ MeV and 98% for $p_t \geq 250$ MeV [96]. Here, the full reconstruction inefficiency is treated as systematic uncertainty. For small n_B ($n_B < 2$) this induces an uncertainty of 4%, for larger n_B the error is below 1%.

In addition to the above stated uncertainties, two further sources of systematic uncertainties need to be taken into account:

- Uncertainty of luminosity:** The luminosity is only known up to 1.5% (see section 2.2.3). To take this into account, an overall error of 1.5% was added quadratically to the systematic uncertainty.

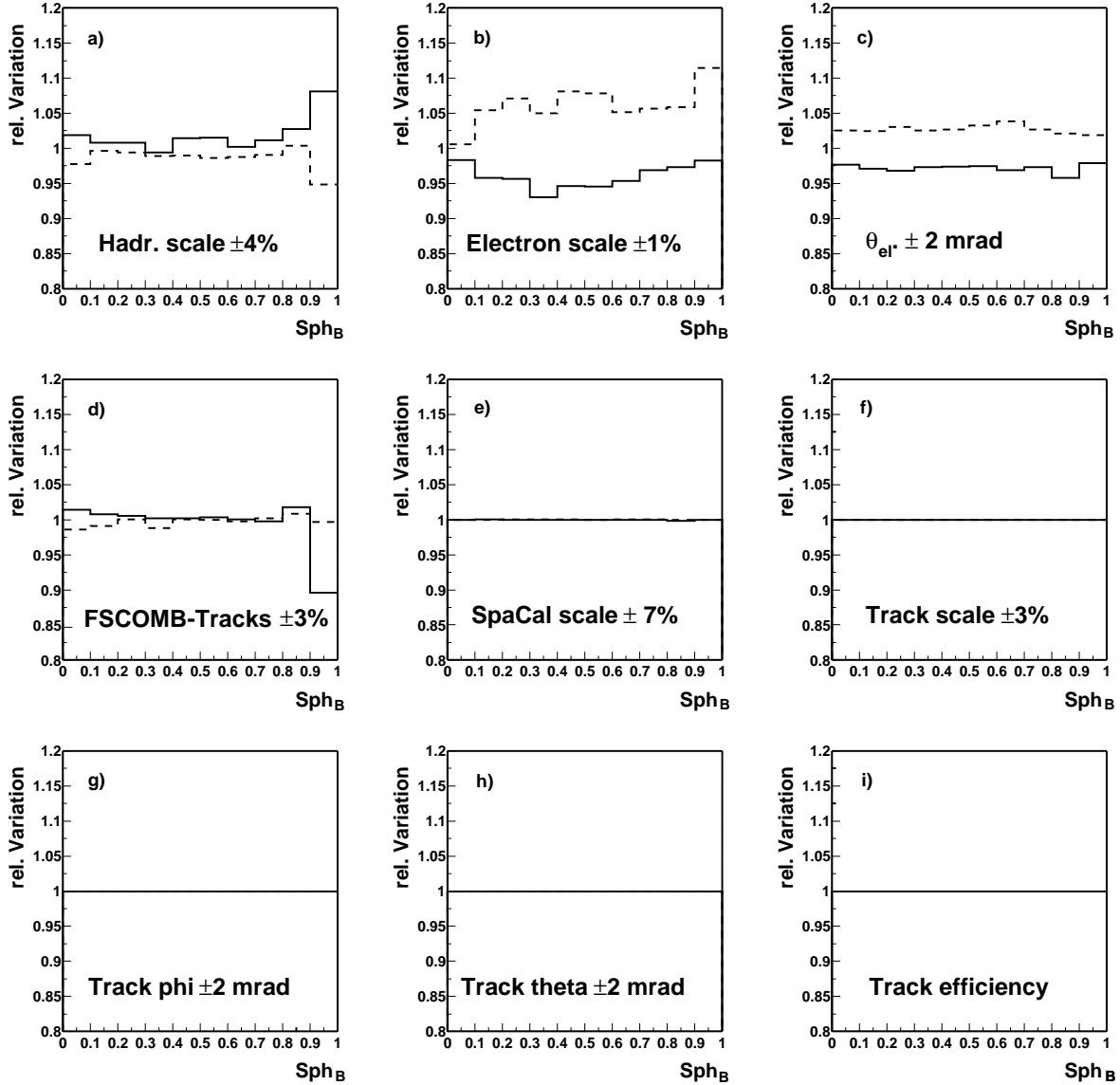


Figure 6.10: Systematic change of the sphericity Sph_B due to the property stated in the figures being changed up (full line) or down (dashed line). The relative change of the MEPS Monte Carlo is shown, i.e. the ratio of the Monte Carlo prediction with the changed reconstruction to the default prediction. The largest systematic uncertainties are induced by the electron energy scale (b) and the electron scattering angle (c), where variations of up to $\approx 5\%$ are seen. The sphericity is not affected by changes of the track reconstruction, since only hadronic final state objects enter into the definition (for FSCOMB objects the track momentum scale is changed separately, shown in d)).

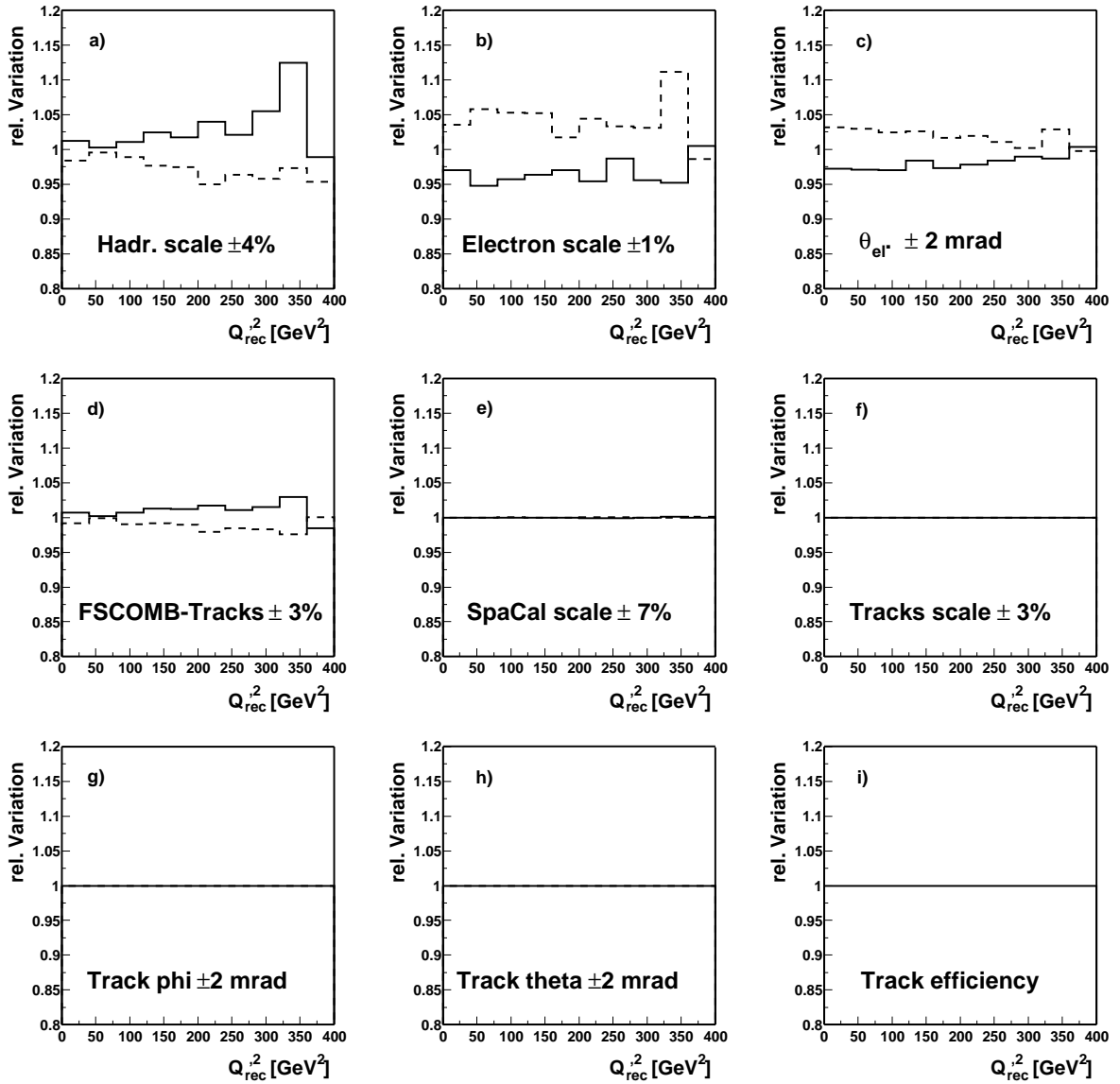


Figure 6.11: Systematic change of Q_{rec}^2 when the reconstruction of the property stated in the figures is changed up (full line) or down (dashed line). The relative change of the MEPS Monte Carlo is shown, i.e. the ratio of the Monte Carlo prediction with the changed reconstruction to the default prediction. The largest systematic uncertainties is induced by the electron energy scale (b) with variations around 5%. Q_{rec}^2 is insensitive to the track uncertainties, because in the definition only the hadronic final state objects enter (for FSCOMB objects the track momentum scale is changed separately, shown in d)).

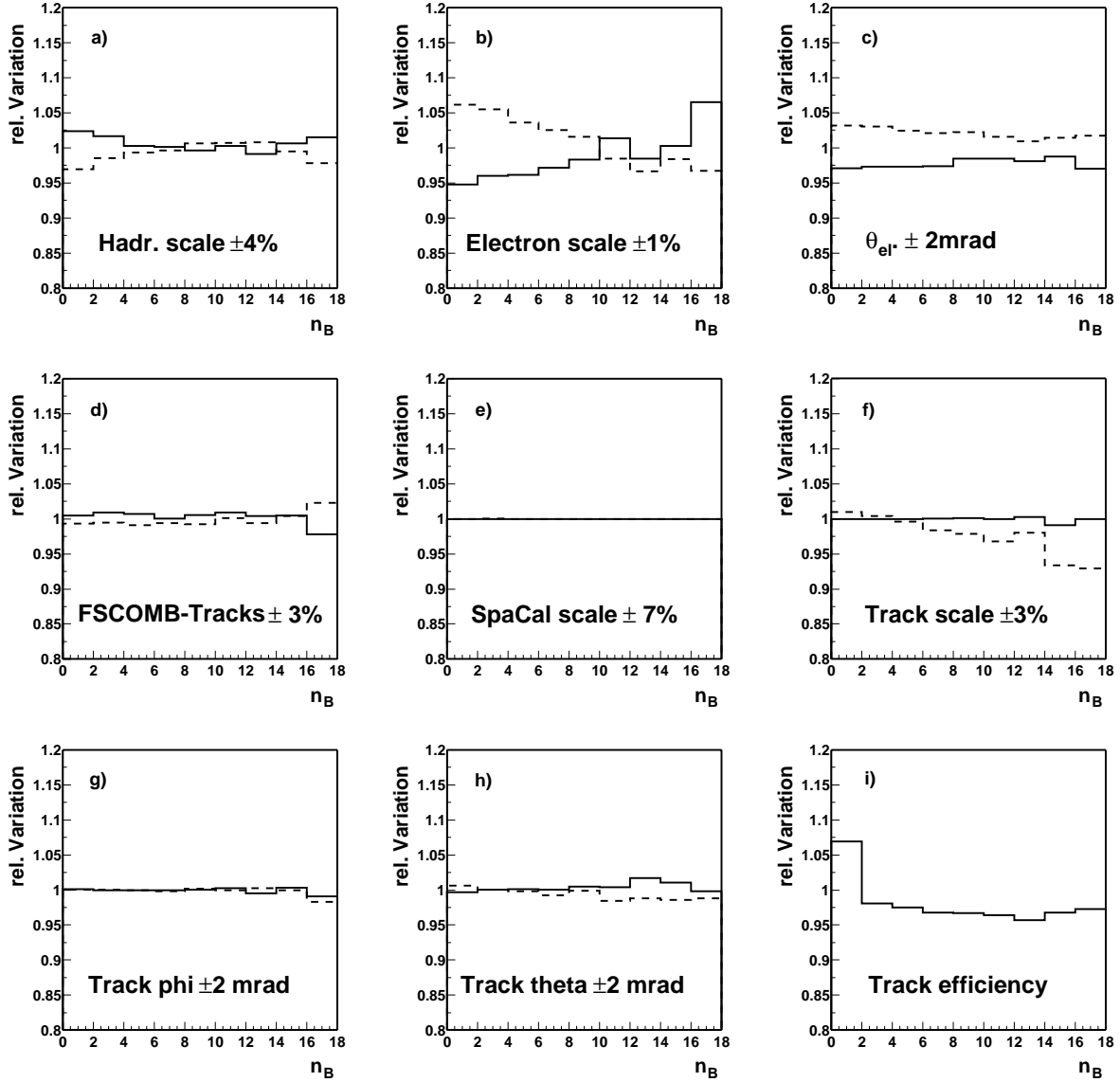


Figure 6.12: Systematic change of the multiplicity in the band n_B when the reconstruction of the property stated in the figures is changed up (full line) or down (dashed line). The relative change of the MEPS Monte Carlo is shown, i.e. the ratio of the Monte Carlo prediction with the changed reconstruction to the default prediction. The largest systematic uncertainties are induced by the electron energy scale (b) with variations around 5% and the track efficiency which induces an uncertainty of 7% in the lowest bin.

Error on F_2 : The structure function F_2 of the proton which enters into the Monte Carlo simulation is known in the kinematic range of this analysis approximately to 3%. The Monte Carlo simulations originally produced with the CTEQ4 [69] parton density functions have been reweighted by the recent H1 F_2 measurements [70]. This error of 3%, too, was added in quadrature to the overall systematic error.

Another source of systematic uncertainties is the model dependency of the standard DIS predictions. In figure 6.13 the relative variations of the predictions of the CDM and MEPS model for the three cut-variables are shown. The difference in the predicted sphericity is below 10% and the difference for Q_{rec}^2 is below 10% for $Q_{\text{rec}}^2 < 200 \text{ GeV}^2$, but only below 20% for larger values of Q_{rec}^2 . The relative difference in the predictions of the multiplicity of the instanton band is below 10% for small and medium multiplicities $n_B \leq 10$, but rises strongly towards very high multiplicities.

Since the model dependency is quite large, it will not be added to the total systematic error. Instead all calculations will be done for both models individually and the results will be compared.

6.5 Combinatorial Cuts Based Search

To create a sample of events with a reduced standard DIS background, cuts are applied to the three variables Sph_B , Q_{rec}^2 and n_B . In order to find the optimal selection of cuts, 125 combinations of reasonable cuts are applied to the distributions of the standard DIS and QCDINS models. The cuts tried are given by all combinations of the following cuts (compare with figures 6.6a–c):

$$\begin{aligned} 0.35, 0.4, 0.45, 0.5, 0.55 &< Sph_B \\ 90, 95, 100, 105, 110 &< Q_{\text{rec}}^2 < 200 \text{ GeV}^2 \\ 9, 10, 11, 12, 13 &< n_B \end{aligned}$$

From all cut combinations, the cut scenario is chosen that leads to the best separation power $S = \epsilon_{\text{INS}}/\epsilon_{\text{sDIS}}$ (see section 3.1, in particular (3.2)), where ϵ_{INS} is the instanton signal efficiency and ϵ_{sDIS} the standard DIS background efficiency, at a minimum instanton efficiency of $\epsilon_{\text{INS}} \approx 10\%$.

The best separation power S is obtained for $Sph_B > 0.4$, $95 < Q_{\text{rec}}^2 < 200 \text{ GeV}^2$ and $n_B > 11$. This combination of cuts yields $S = 125$ for the MEPS model and $S = 86$ for the CDM model representing the background. The instanton efficiency is $\epsilon_{\text{INS}} = 10.2\%$. Thus, the background was suppressed by a factor of approximately 1000. It needs to be stressed that this cut scenario was chosen not by looking at the data but only by optimising the separation power for the I-signal model and two standard DIS background models.

6.5.1 Results of the Cut-Based Method

With the cuts stated above, 484 data events were found, while the CDM model predicts 443_{-35}^{+29} events and MEPS 304_{-25}^{+21} events. These numbers are summarised in table 6.1. The errors on the Monte Carlo models include the statistical as well as the systematic error added

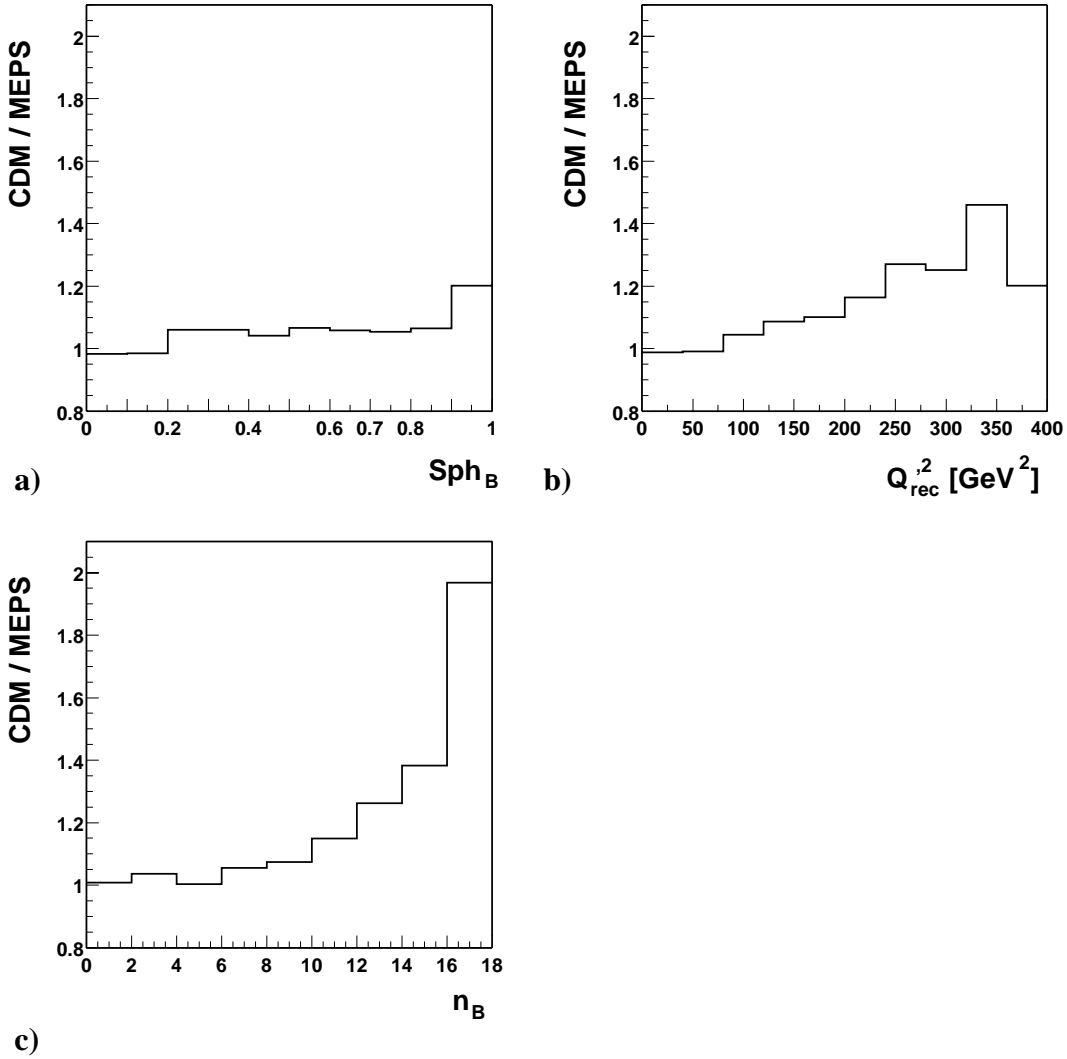


Figure 6.13: The dependency of the three observables Q_{rec}^2 , Sph_B and n_B , which are cut in order to select an instanton-enriched subsample of events, on the Monte Carlo models CDM and MEPS. Shown is the ratio of the CDM prediction over the MEPS prediction. Differences of about 20% and more are seen in the description of the high multiplicity tail and of 20 to 30% for high Q_{rec}^2 . The description of the sphericity differs by about 5–10% only.

	N	ϵ_{sDIS}	$S = \epsilon_{\text{INS}}/\epsilon_{\text{sDIS}}$
DATA	484		
CDM	443^{+29}_{-35}	0.118%	86
MEPS	304^{+21}_{-25}	0.081%	125
QCDINS	81		

Table 6.1: The table summarises the results of the cut-based method. Listed are the numbers of events in the data and the expected numbers of events of the Monte Carlo simulations, the background efficiency ϵ_{sDIS} and the separation power S after the cuts $n_B > 11$, $95 < Q_{\text{rec}}^2 < 200 \text{ GeV}$ and $Sph_B > 0.4$.

	CDM		MEPS	
	up	down	up	down
(a) LAr hadronic energy scale $\pm 4\%$	-1.22%	2.55%	0.23%	2.81%
(b) SpaCal electron energy scale $\pm 1\%$	0.07%	-0.33%	1.38%	-0.35%
(c) Electron scattering angle $\pm 2 \text{ mrad}$	-1.32%	2.64%	-1.27%	2.13%
(d) Track momentum scale (FSCOMB) $\pm 3\%$	0.93%	-0.75%	-0.56%	3.02%
(e) SpaCal hadronic energy scale $\pm 7\%$	0.00%	0.00%	-0.39%	0.00%
(f) Track momentum scale $\pm 3\%$	0.19%	-3.14%	0.22%	-3.74%
(g) Track azimuth angle $\pm 2 \text{ mrad}$	-0.21%	0.37%	-0.03%	0.18%
(h) Track polar angle $\pm 2 \text{ mrad}$	0.84%	-1.06%	0.94%	-1.65%
(i) Track efficiency 95/98%	-3.62%		-4.28%	
Luminosity uncertainty 1.5%	1.5%		1.5%	
F_2 uncertainty 3%	3.0%		3.0%	
Total syst. uncertainty (absolute # events):	19.5	-27.6	16.5	21.4
Statistical error (absolute # events)	21.5		13.0	
Total Error (absolute # events)	29	-35	21	-25

Table 6.2: The systematic errors of the cut-based discrimination method. “Up” and “down” mean, that the respective error is calculated by scaling the stated property upwards or downwards by the given percentage. The main contributions to the systematic uncertainty come from the LAr hadronic energy scale, the electron scattering angle, the track momentum scale and the track efficiency.

in quadrature. The sources for the systematic uncertainties were described in the previous section and the resulting uncertainties are listed in detail in table 6.2. The largest sources of systematic uncertainties are the hadronic energy scale in the liquid argon calorimeter, the electron scattering angle, the track momentum scale and the efficiency for track finding.

More events are found in the data than in either one of the background Monte Carlo simulations. While MEPS suggests a clear excess in the data, the prediction by the CDM model is only slightly below the data. It is surprising that CDM comes closer in the description of the data after the application of the instanton selection cuts, since it had more difficulties to describe the data prior to any cuts. The two standard DIS Monte Carlo simulations disagree considerably with each other, and the excess seen by the MEPS model is of the order of this disagreement, so that no firm conclusions can be drawn. Table 6.1 also includes the expected number of QCDINS generated events passing the cuts for a comparison.

In figure 6.14 the six observables are presented after applying all cuts. Shown are the data, the two Monte Carlo simulations and the QCDINS prediction. The shape of the excess of the data of the distributions of n_B , Q_{rec}^2 , Sph_B and Δ_B are compatible with an instanton signal, especially for the MEPS model. Since CDM is only slightly below the data, the excess seen by the data over the CDM model is too small to be explained by the instanton model, although the shape is compatible. While the shapes of the $E_{t,\text{Jet}}$ distributions neither support nor reject the instanton hypothesis, the excess in the $E_{t,B}$ variable tends to lie towards lower values than favoured by the instanton model. It should be noted, however, that these two variables are most affected by contributions of non-planar diagrams (see section 1.5) and shifts towards lower values are well possible [16].

Since this study, based on combinatorial cuts, neither rejects nor supports the instanton hypothesis, a study based on a multivariate method using range searching will be applied in the next section. The expected better discrimination between signal and background events may help to make a clearer statement.

6.6 A Discriminant Search

The same data sample as in the cut-based search will now be studied with the multivariate discriminant method based on range searching.

6.6.1 Definition of the Discriminant

To model the background and signal of the multivariate discriminant, only a fraction of the Monte Carlo events is used, to have statistically independent training and validation events. Of the 301722 weighted MEPS events, for which weights add up to a total of $1.754 \cdot 10^6$, 40% were chosen at random as training events. 70% of the 165301 QCDINS generated events, with a sum of weights of 131683, were chosen as training events for the signal. The reasons to divide the sample of events in this way is first to have nearly equal amounts of events in the two binary trees for the signal and the background, and second to have sufficiently many events left in the signal region, where the performance of the method is measured and differential distributions will be plotted. The CDM events were not used in the discriminator, they were only used as control events, due to the limited statistics of only 163930 real events

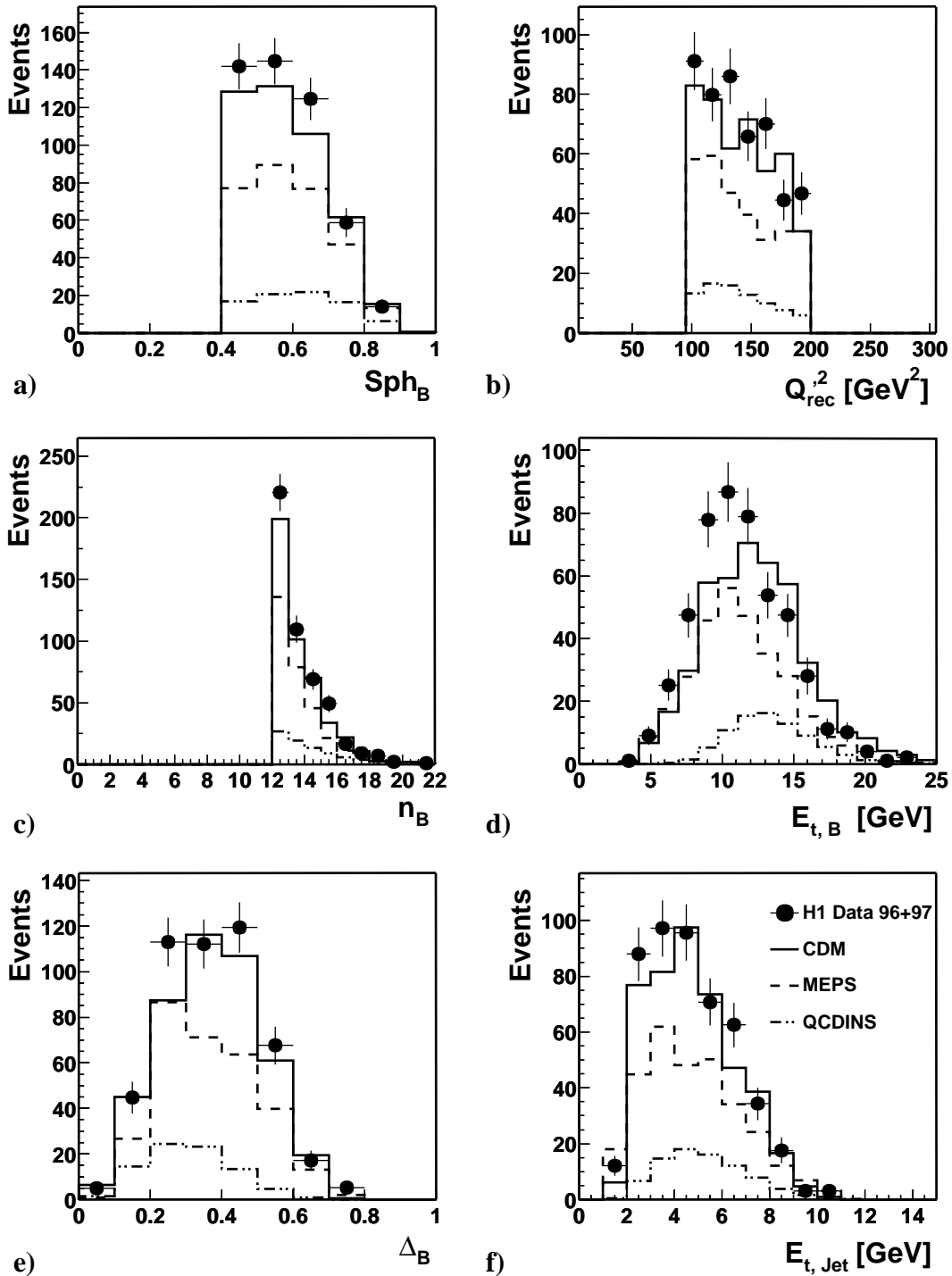


Figure 6.14: The observable distributions a) of the sphericity Sph_B , b) the reconstructed virtuality Q_{rec}^2 , c) the charged particle multiplicity in the band n_B , d) the transverse energy in the band $E_{t,B}$, e) the isotropy variable Δ_B and f) the transverse energy of the current jet $E_{t,Jet}$ after the cuts ($Sph_B > 0.4$, $Q_{rec}^2 < 200 \text{ GeV}^2$, $n_B > 11$) to enrich instanton-induced events. Data (filled circles), the two standard DIS background models CDM and MEPS (full and dashed line) and the prediction of the QCDINS model (dash-dotted) are shown.

with a sum of the weights of 834000. It was checked, however, that the results obtained do not significantly change when the CDM model was used in the discriminant.

Several different box-sizes were studied, where also the relative length of the edges of the box was varied. However, this did not change the resulting separation power by more than about 10%. Nevertheless, the box with the best separation power was chosen.

The lengths of the edges of the box, in which events are counted around the event to be classified, is 65 GeV^2 for $Q_{\text{rec}}'^2$ and 0.0875 for Sph_B . The n_B distribution is special since only integer values of n_B occur. The possible values of the box-size in the n_B -direction is thus restricted. Not centring the box around the value n_B of the event to be classified yielded the best results. Since this distribution has a long tail with increasingly few events per bin, the size of the box in n_B is 6 with only 1 downward and 5 bins towards larger values of n_B . That is, events with numbers of charged particles $n_B \geq n_{B,0} - 1$ and $n_B \leq n_{B,0} + 5$ were counted, with $n_{B,0}$ the charged particles multiplicity in the I-band of the event to be classified. To limit the statistical error of the discriminant, at least 20 signal and background events each were required in the box, otherwise the event was classified as background. The induced error on the separation power can be estimated to be about 10% using the above studied different box-sizes.

6.6.2 Results of the Discriminant Search

The resulting discriminant is shown in figure 6.15. The shape normalised signal and background distributions are shown along with the H1 data. The data are well described by the two Monte Carlo models except in the leftmost bin at $D = 0$, where a discrepancy of 12% is seen in the CDM model. The data and background distributions peak towards $D = 0$, while the QCDINS simulated distribution peaks towards $D = 1$. For $D > 0.988$ an instanton efficiency of 10.0% is obtained, the same efficiency as for the I-enriched sample of the combinatorial cut-based method.

The discriminant achieves a separation power of 126 in case of the MEPS model and 106 in the case of the CDM model at an instanton efficiency of 10%. While the increase in separation power is more than 20% for the CDM model, only a small increase is obtained in case of the MEPS model when compared to the result of the combinatorial cut method. Thus, although only the MEPS model was used to model the background events in the discriminant, the two background models do not disagree as much as in the case of the combinatorial cut method.

Interestingly, calculating the separation power of the cuts of the combinatorial cut method for the validation events only, with the CDM model $S = 84$ is achieved, and for the MEPS model $S = 118$. It seems that picking the best cut scenario out of 125 will also pick a scenario that profits slightly from statistical fluctuations. In fact, at least a 2σ deviation is expected from the actual separation power of the cuts.

Applying the cut $D > 0.988$, 410 events are observed in the data, while 354^{+40}_{-26} are predicted by the CDM model and 299^{+25}_{-37} events are expected by the MEPS model (see table 6.3). The Monte Carlo errors are obtained by adding the statistical and systematic uncertainties added in quadrature. The sources of the systematic uncertainties are summarised in table 6.4. The largest sources of systematic uncertainties are the hadronic energy scale of the liquid argon calorimeter, the energy scale of the electron in the SpaCal calorimeter, and the

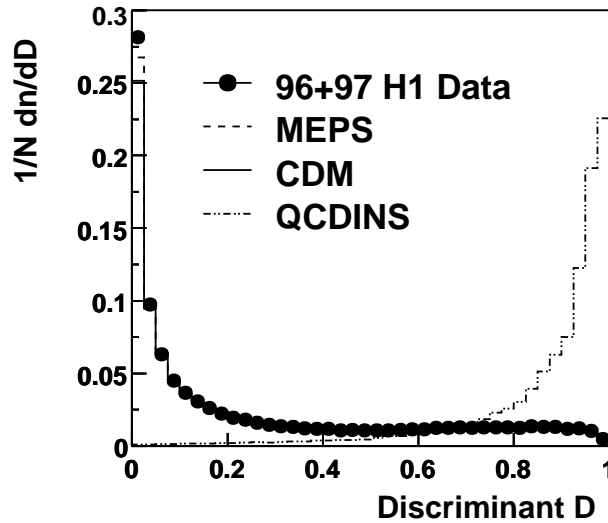


Figure 6.15: The shape normalised discriminant D of the 1996 and 1997 H1 data along with the standard DIS background models CDM and MEPS. The background models and the data peak sharply towards $D \approx 0$, while the QCDINS model peaks towards $D \approx 1$.

	N	ϵ_{sDIS}	$S = \epsilon_{\text{INS}}/\epsilon_{\text{sDIS}}$
DATA	410		
CDM	354^{+40}_{-26}	0.095%	106
MEPS	299^{+25}_{-37}	0.080%	126
QCDINS	81		

Table 6.3: The table summarises the results of the multivariate discriminant method based on range searching. Listed are the numbers of events, the background efficiency ϵ_{sDIS} and the separation power S for the cut $D > 0.988$.

track momentum scale and track finding efficiency. The obtained number of events after the cut on D are compatible with the result obtained by the cut-based method.

A closer look at table 6.4 reveals that, e.g. for the track momentum uncertainty, the resulting estimated error is very asymmetric. Figure 6.16 shows the influence of the systematic uncertainties on the discriminant D . Large values of D are blown up by plotting D with a scale according to $-\log_{10}(1-D)$. As can be seen, the asymmetry seems to be a feature of the discriminant.

6.6.3 Observable Distributions of the I-Enriched Sample

Comparing the systematic uncertainties of the discriminant method and the cut-based method, one sees that the overall systematic uncertainty is larger for the discriminant method. In par-

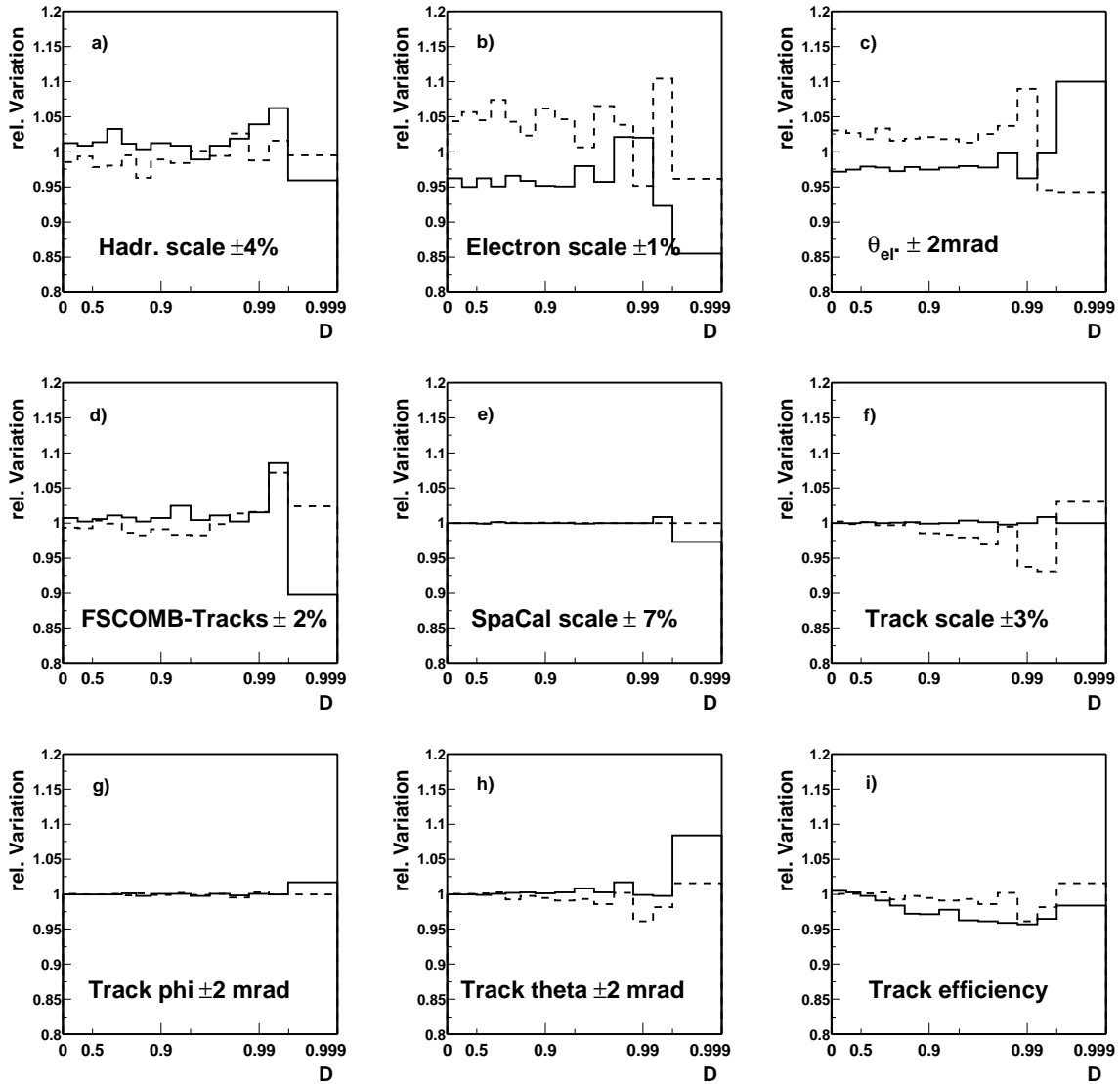


Figure 6.16: Systematic change of the discriminant D when the parameters stated in the figures are changed up (full line) or down (dashed line). The relative change of the MEPS Monte Carlo is shown. The largest systematic uncertainty is induced by the electron energy scale (b) with variations around 5%, except for the rightmost bin where a change of 15% is observed.

ticular, the SpaCal energy scale which makes only a minor contribution to the systematic uncertainty of the result of the cut method has a big influence on the result of the discriminant search. The reason for this behaviour is unclear. However, it should be noted that only $\approx 2/3$ of all data events selected by the discriminant method are also selected by the cut-based method. We will also see in the following section, that the selected events come from different regions of the phase space.

All discriminating variables after a cut on $D > 0.988$ are shown in figure 6.17. One advantage of the multivariate discriminator technique over the cut-based method is that the full distribution of the three observables used to discriminate the instanton signal from the background can be inspected. It is interesting to note, that the largest drops in the three cut variable distributions are seen there, where the cut-based method placed the cuts. The n_B distribution also reveals that the excess of the data over the background Monte Carlos, which seems to come only from the bin with 12 charged particles in the case of the cut-based method, actually also extends towards lower values of n_B .

The shape of the excess of the data in the n_B , Q_{rec}^2 and Sph_B distribution is similar to the shape of the instanton contribution. While by definition of the discriminant the shape of background and signal distribution have to be similar (unless the full potential of the method is exploited), the shape of the excess of the data over the background Monte Carlo is not an artifact of the method and therefore significant. For $E_{t,B}$ and $E_{t,\text{Jet}}$ the shape of the QCDINS expectation does not fit in well in the gap between data and the CDM model, while the shape of the MEPS model is compatible with the data. Since both observables are most affected by the theoretical uncertainties due to non-planar diagrams, the shape can not rule out the

	CDM		MEPS	
	up	down	up	down
(a) LAr hadronic energy scale $\pm 4\%$	2.73%	4.60%	3.80%	-1.42%
(b) SpaCal electron energy scale $\pm 1\%$	4.98%	4.70%	-6.29%	-1.07%
(c) Electron scattering angle $\pm 2\text{mrad}$	-1.32%	2.64%	-1.27%	2.13%
(d) Track momentum scale (FSCOMB) $\pm 3\%$	2.78%	2.00%	-0.55%	1.13%
(e) SpaCal hadronic energy scale $\pm 7\%$	0.09%	0.09%	0.00%	0.00%
(f) Track momentum scale $\pm 3\%$	0.09%	-3.04%	0.20%	-5.88%
(g) Track azimuth angle $\pm 2\text{ mrad}$	-0.32%	0.08%	-0.22%	0.20%
(h) Track polar angle $\pm 2\text{ mrad}$	0.80%	-0.61%	0.61%	-2.99%
(i) Track efficiency 95/98%	-3.53%		-4.05%	
Luminosity uncertainty 1.5%	1.5%		1.5%	
F_2 uncertainty 3%	3.0%		3.0%	
Total syst. uncertainty (absolute # events)	35.6	-18.4	15.7	-31.5
Statistical error (absolute # events)	17.9		18.9	
Total Error (absolute # events)	39.9	-25.7	24.6	-36.8

Table 6.4: The systematic uncertainties of the multivariate discrimination method. The main contributions to the systematic error come from LAr energy scale, the SpaCal electron energy scale, the track momentum scale and the track efficiency.

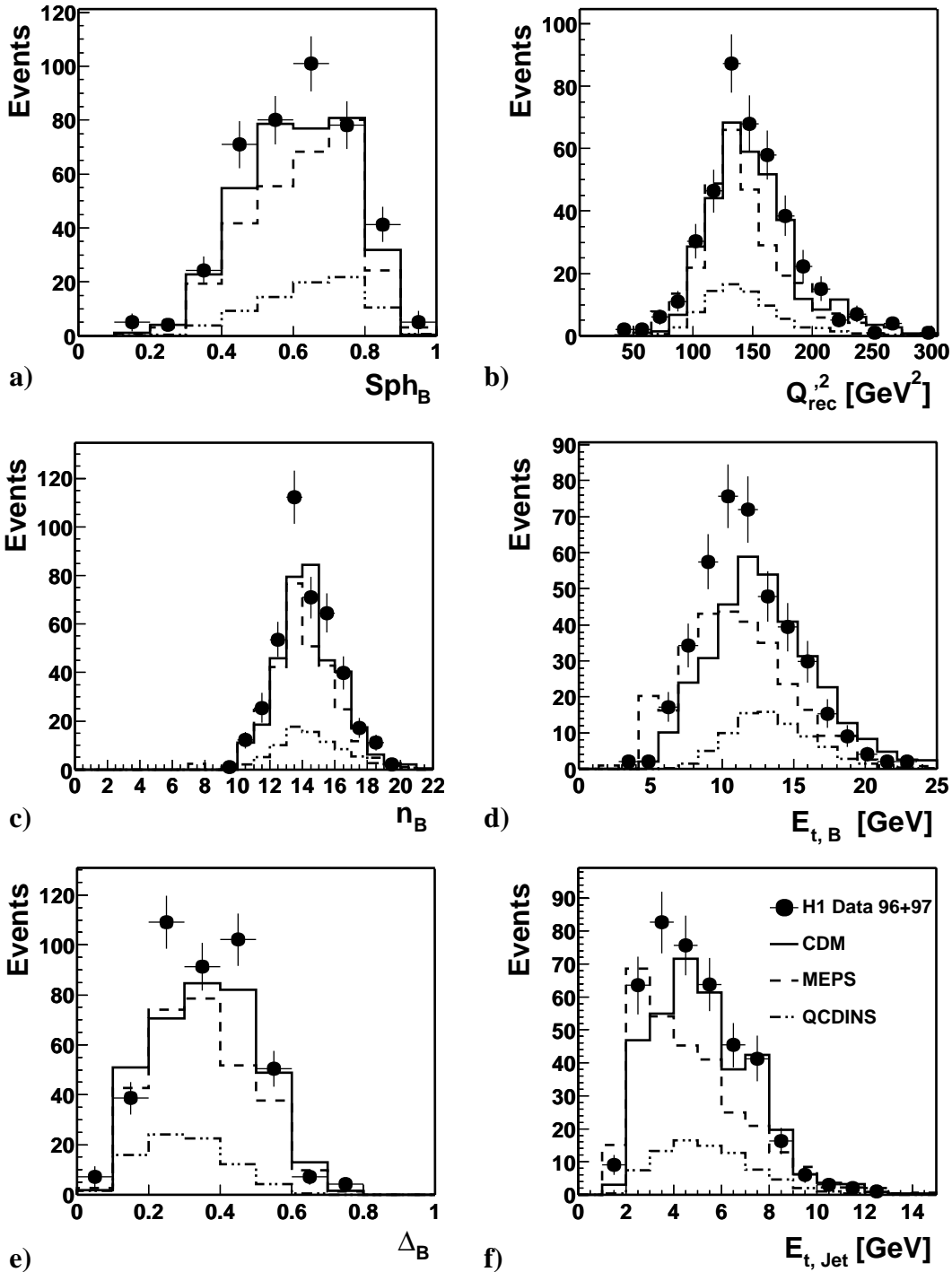


Figure 6.17: The observable distributions of a) the sphericity Sph_B , b) the virtuality Q_{rec}^2 , c) the multiplicity in the band n_B , d) the transverse energy in the band $E_{t,B}$, e) the isotropy variable Δ_B and f) the transverse energy of the current jet $E_{t,Jet}$ after the cut $D > 0.988$ to enrich instanton-induced events. Data (filled circles), the two standard DIS background models CDM and MEPS (full and dashed line) and the prediction of the QCDINS model (dash-dotted) are shown.

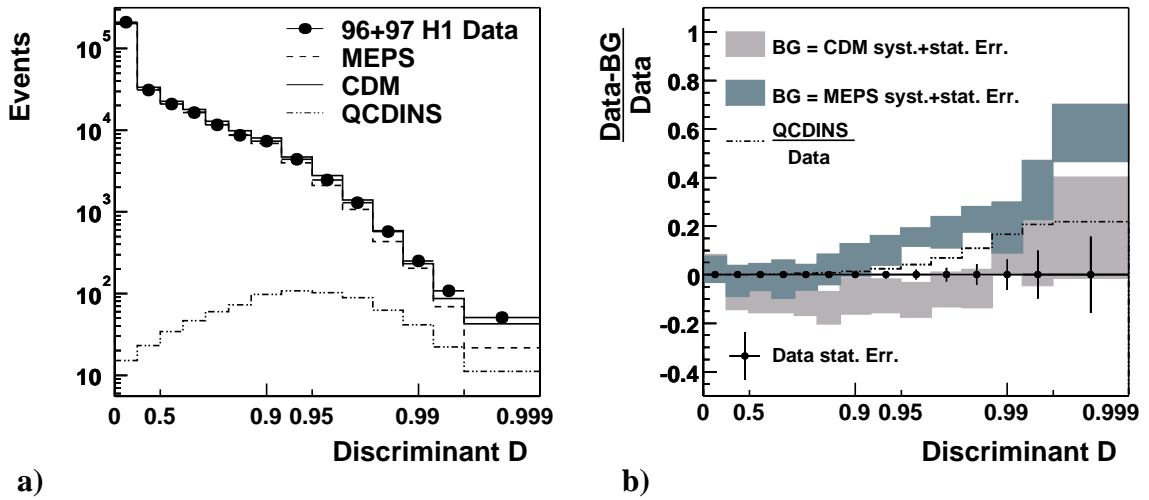


Figure 6.18: In a) the distribution of the discriminant is shown for the data, and the MEPS, CDM and QCDINS models. On the x -axis D is drawn with a scale according to $-\log_{10}(1-D)$. b) shows the ratio of the difference of data and the CDM or MEPS model to the data including systematic and statistical uncertainties. Also shown is the respective statistical error of the data and the ratio of expected events from QCDINS to measured data events.

instanton hypothesis. The difference seen in the isotropy variable Δ_B between the data and the standard DIS Monte Carlo simulations is in case of the MEPS model compatible with the instanton hypothesis.

6.6.4 A Close-Up of the Discriminant

The multivariate discrimination technique offers furthermore the possibility to study the complete information from the region, where no instanton contribution is expected in the data up to the instanton-enriched region, by inspecting the distribution of the resulting discriminant. Figure 6.18a shows the absolutely normalised discriminant double logarithmically, where on the x -axis a scale according to $-\log_{10}(1-D)$ is used to make the $D \approx 1$ region visible. The overwhelming fraction of the standard DIS background events is concentrated at $D \ll 1$. Towards larger values of D , the background falls by three orders of magnitude, while the instanton distribution peaks at $D \approx 0.95$ and falls off slowly towards higher D . In the last three bins, which correspond to the cut value of $D > 0.988$, an instanton contribution of 20% is expected.

The description of the data by the background Monte Carlo simulations is illustrated in more detail in figure 6.18b, where the ratio of the difference of background and data to data is shown. Here, the statistical and systematic uncertainties are shown as a band. Within the errors, the MEPS Monte Carlo gives an excellent description of the data up to $D < 0.95$. With increasing separation a growing excess of events is seen in the data. The largest discrepancy of 60% is seen in the bin with largest D . The increasing excess of data is qualitatively similar

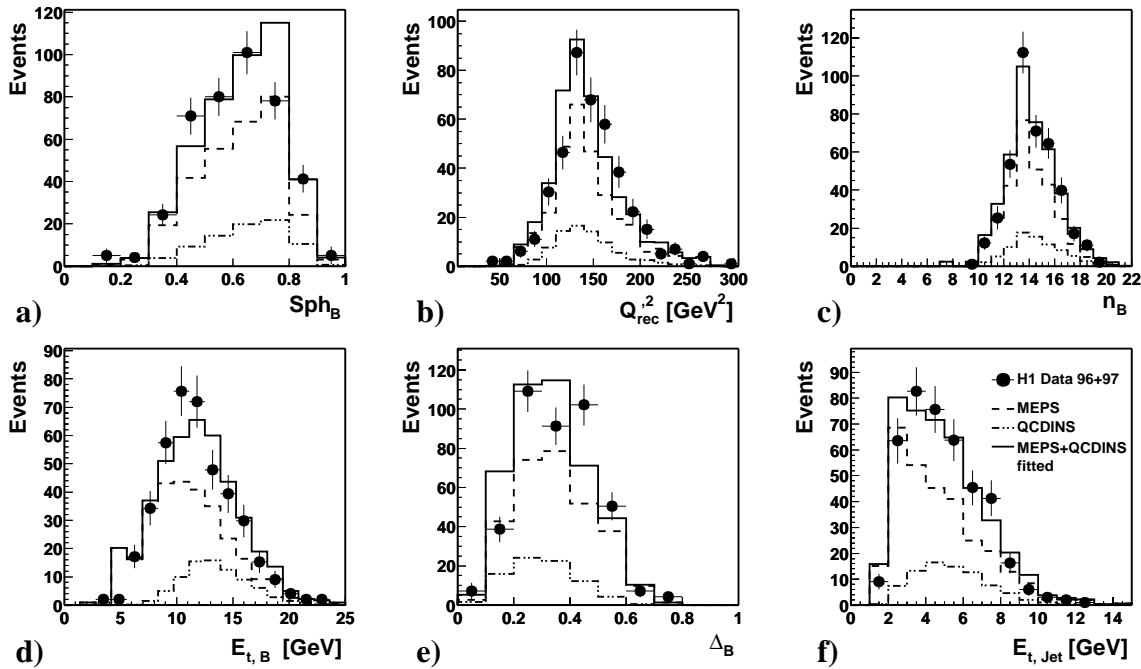


Figure 6.19: The distributions of the discriminating instanton observables of the MEPS Monte Carlo simulation plus the fitted fraction of I-induced events (full line) together with the data. As a reference the MEPS (dashed line) and the default QCDINS (dash-dotted line) predictions by themselves are also shown.

to the expected instanton contribution, which becomes important at large values of D . This contribution is shown as the ratio of the expected instanton signal over the data (dotted line). The CDM Monte Carlo describes the data only in the lowest bin of D where most of the events are located. For medium values of D , CDM lies below the data but comes closer to it with growing D . In the last three bins of D , CDM slightly overshoots the data, although this excess is not significant taking the errors into account.

Within the given accuracy of the standard DIS background models, no firm conclusions can be drawn. While both standard DIS simulations predict an increasing excess towards high values of the discriminant and thereby high likelihoods for instanton-induced events, a large discrepancy between the Monte Carlo simulations is seen.

A Fit of the Instanton Fraction

By fitting the shape of the ratio of the QCDINS expectations to the data to the ratio of the difference of data and MEPS to data (see figure 6.18b), one can derive the possible instanton contribution to the data. In this way, the knowledge of the characteristic final state only of the QCDINS simulated events and the prediction of the MEPS Monte Carlo for the expected standard DIS background are exploited. The fit results in a 1.6 times larger cross-section for instanton-induced events than is expected by the QCDINS simulation. A similar fit using the CDM prediction is not possible, since in this case a negative contribution of instanton-

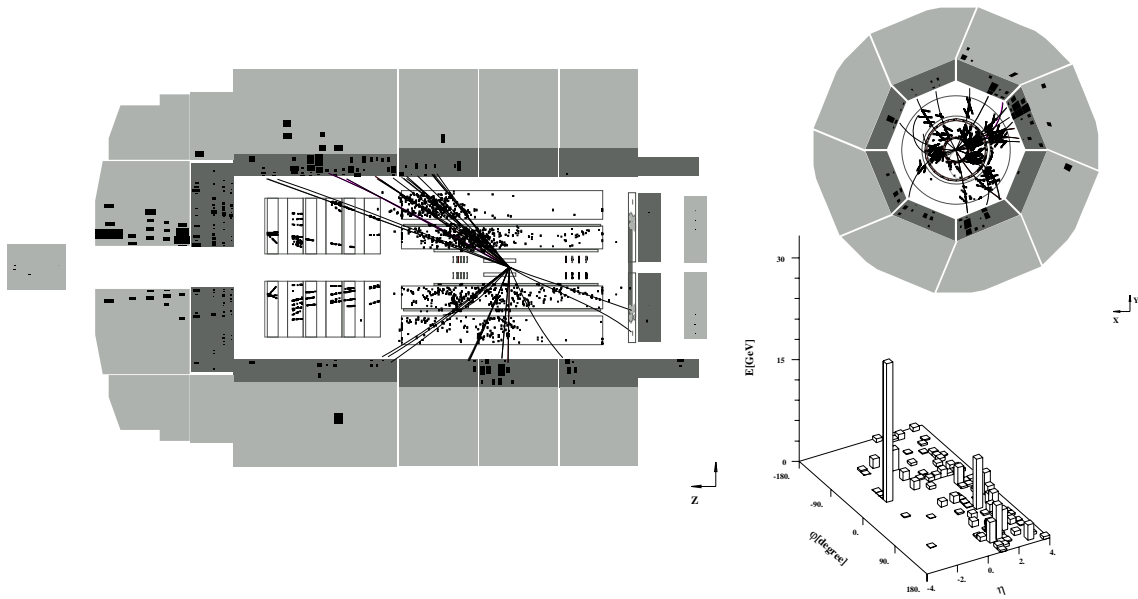


Figure 6.20: The $r-z$ - and $x-y$ -views of the H1 detector show one of the selected events of the 1997 data sample. Also shown is E_t versus the $\eta - \phi$ -plane in the laboratory frame including the scattered electron. The kinematics of the DIS event are $x = 2.5 \cdot 10^{-3}$ and $Q^2 = 62 \text{ GeV}^2$ at $y = 0.27$. The following instanton characteristic variables have been calculated: $Sph_B = 0.41$, $n_B = 15$, $Q_{\text{rec}}^2 = 119 \text{ GeV}^2$ and $E_{t,\text{jet}} = 4.7 \text{ GeV}$.

induced processes would be expected over a large range of the discriminant, which does not make sense. Because of this discrepancy, also the fit using the MEPS model should be regarded with great caution.

With the known expected instanton contribution to the MEPS modelled background, it is possible to compare the predicted background plus the fitted signal contribution with the data. Figure 6.19 shows the MEPS prediction with the addition of the 1.6-fold default prediction of QCDINS as a full line together with the standard MEPS and QCDINS simulations and the data. Both contributions together, the one from the MEPS model and the one from the fitted QCDINS model, describe the data rather well. For all distributions this fit is compatible within statistical errors with the data. However, it needs to be stressed, that since with the CDM model such a fit would not succeed and the CDM model cannot so far be disqualified, no firm conclusions can be drawn.

6.6.5 Examples of Selected Events

An example of an event selected by the cut on the discriminant is shown in figure 6.20. If interpreted as an instanton-induced event as modelled by the QCDINS generator it is quite a typical event with relatively low $Q_{\text{rec}}^2 \approx 119 \text{ GeV}^2$ and a high multiplicity of $n_B = 15$. In the E_t versus the $\eta - \phi$ -map in the laboratory system² a densely populated band is seen around

²In the lab-frame positive η is in the direction of the proton (forward direction).

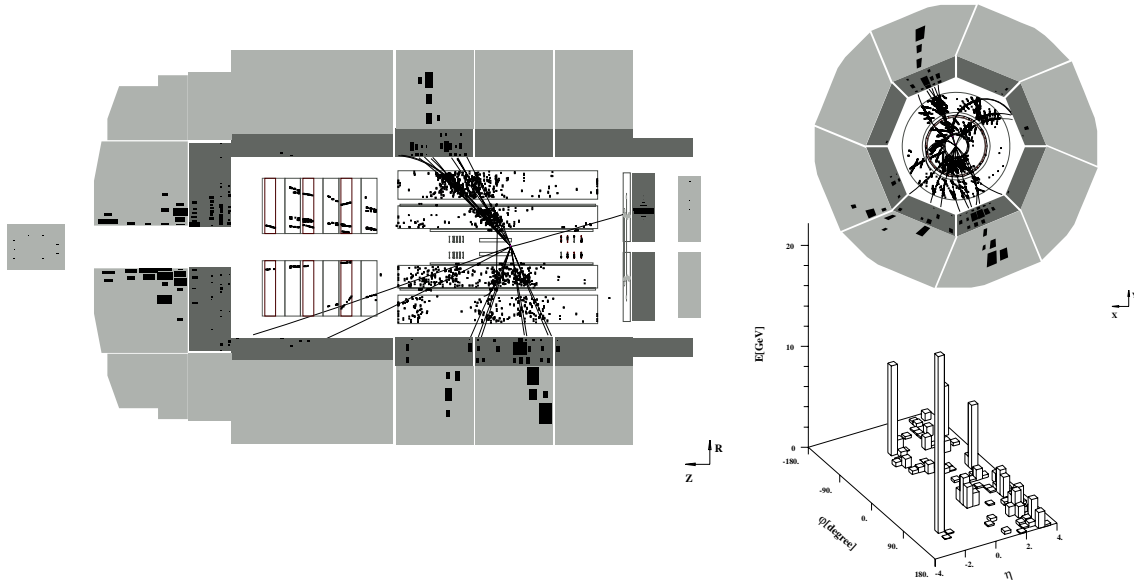


Figure 6.21: The $r-z$ - and $x-y$ -views of the H1 detector show another one of the selected events of the 1997 data sample. Also shown is E_t versus the $\eta-\phi$ -plane in the laboratory frame including the scattered electron. The kinematics of the DIS event are $x = 1.1 \cdot 10^{-3}$ and $Q^2 = 35 \text{ GeV}^2$ at $y = 0.37$. The following instanton characteristic variables have been calculated: $Sph_B = 0.56$, $n_B = 12$, $Q_{\text{rec}}^2 = 137 \text{ GeV}^2$ and $E_{t,\text{jet}} = 8.2 \text{ GeV}$.

$\eta \approx 2$. The reconstructed current jet has a transverse energy of 4.7 GeV .

A possible standard DIS background event is shown in figure 6.21. This event has a higher $E_{t,\text{jet}}$ of 8.2 GeV and while there exists a densely populated band of particles, three or four jets with relatively high transverse momenta stick out, so that this event can also be explained as a multi jet event in standard QCD. Since only about a quarter of the events selected by the cut on the discriminant are expected to be instanton-induced, three quarters of the events are actually standard DIS events.

6.7 Cross-Section Exclusion Limits

Since no evidence for instanton-induced events in deep-inelastic scattering has been found in the H1 data given the large uncertainties of the standard DIS background, limits on the instanton-induced cross-section are derived in this section. Because the hadronic final state of instanton-induced events strongly depends on the centre-of-mass energy squared $W_f^2 = Q^2(1-x')/x'$ available for the partons emerging from the instanton subprocess, the topology of the events is crucially influenced by the minimal cut values, above which instanton perturbation theory is believed to be valid and is used. In addition, the topology of the hadronic final state depends on the assumed x' and Q^2 distributions, which are under theoretical control only for large enough x' and Q^2 . To be independent of this theoretical input,

the cross-section limits will be calculated in small ranges of these variables in section 6.7.2. The result will be compared to recent lattice data in section 6.7.3. However, first the limit on the cross-section for instanton-induced event in the fiducial region is calculated.

6.7.1 Cross-Section Limits in the Fiducial Region

A limit³ on the maximum number of allowed instanton-induced events n_{lim} at 95% confidence level (CL) is derived by first calculating the probability density function of finding n_{obs} observed events, if n_{bg} background and $n_s = \varepsilon_s \tilde{n}_s$ signal events are expected in the region selected by the cut. The probability density is then given according to Bayes theorem by the Poisson distribution

$$P(n_{\text{obs}}; \mu = n_{\text{bg}} + n_s) = \frac{e^{-(n_{\text{bg}} + n_s)} (n_{\text{bg}} + n_s)^{n_{\text{obs}}}}{n_{\text{obs}}!} . \quad (6.10)$$

Here, no uncertainties of the background and the efficiency of the signal have yet been taken into account. To do this, the distribution is convoluted with the uncertainty of the background and the signal efficiency, both modelled by Gaussians $G_{\text{bg}}(x; \mu = n_{\text{bg}}, \sigma_{\text{bg}})$ and $G_s(x; \mu = n_s = \varepsilon_s \tilde{n}_s, \sigma_{n_s} = \sigma_{\varepsilon_s} \tilde{n}_s)$ to obtain the probability density $g(n_s)$ of finding n_s instanton-induced events in the fiducial region

$$g(\tilde{n}_s) = c \int_0^\infty dn_{\text{bg}} \int_0^\infty dn_s P(n_{\text{obs}}; n_{\text{bg}} + n_s) G_s(n_s) G_{\text{bg}}(n_{\text{bg}}) , \quad (6.11)$$

where c is an appropriate normalisation constant.

The limit on the maximum number of signal events in the fiducial region can be then derived by requiring the probability of finding more than n_{lim} events to be 1-CL:

$$\int_{n_{\text{lim}}}^\infty g(\tilde{n}_s) d\tilde{n}_s \stackrel{!}{=} 1 - CL \quad (6.12)$$

The maximum number of allowed signal events n_{lim} is obtained by solving (6.12) numerically using an algorithm from [99].

With the maximum possible number n_{lim} of instanton-induced events in the sample after the instanton-enriching cuts, the cross-section limit is given by

$$\sigma_{\text{lim}} = \frac{n_{\text{lim}}}{L} , \quad (6.13)$$

where L is the total integrated luminosity.

In the fiducial region $x' > 0.35$ and $Q'^2 > 113 \text{ GeV}^2$, an instanton cross-section of 109 pb (47 pb) can be excluded by the MEPS (CDM) model using the combinatorial cut method (see table 6.5) at a confidence level of 95%. Applying the method to the multivariate discriminant, allows to exclude an instanton-induced cross-section of 80 pb using the MEPS Monte Carlo as a background model and 55 pb using the CDM Monte Carlo. Both discrimination techniques lead to similar results. The limits are not far from the predicted cross-section in this region which is calculated to be approximately 43 pb.

³The method used here, follows closely the ideas in [98].

	N_{DATA}	CDM		MEPS		Bg. Independent
		N_{CDM}	σ_{lim}	N_{MEPS}	σ_{lim}	σ_{lim}
Combinatorial cuts	484	443^{+29}_{-35}	47 pb	304^{+21}_{-25}	109 pb	255 pb
Discriminant method	410	354^{+40}_{-26}	55 pb	299^{+25}_{-37}	80 pb	221 pb

Table 6.5: The table shows the limits derived on the instanton-induced cross-section in the fiducial region at a confidence level (CL) of 95%. The background independent limit was calculated by setting the expected background contribution to zero.

It has been said before, that it is questionable, whether the two DIS Monte Carlo models are able to describe the standard DIS background in this extreme corner of the phase space, where only about 0.1% of the events of the whole data sample of DIS events are expected. It is therefore desirable to provide a cross-section limit independent of these Monte Carlo predictions. This is achieved by deriving an upper limit where the standard DIS background is set to zero. Whatever the “true” number of DIS background events in this region of phase space is, which is selected only by exploiting the QCDINS predictions on the hadronic final state, the number of instanton-induced events can certainly not be larger than the number of events found in the data. By this, a very conservative limit can be extracted which only depends on the topology of instanton-induced events as modelled by the QCDINS Monte Carlo. At 95% confidence level, an instanton-induced cross-section of 255 pb can be excluded by the combinatorial cut-method and of 221 pb by the discriminant method.

6.7.2 Instanton Model Independent Cross-Section Limits

To further reduce the influence on an assumption on the x' and Q'^2 distribution of the events, it is necessary to become independent of the distribution of these variables. If the cross-section limits are derived in small bins of x' and Q'^2 , the dependence on the predicted behaviour of these distributions vanishes, and the only theoretical input left is that the topology is correctly described for fixed x' and Q'^2 .

The limits are derived for 25 bins in x' and Q'^2 , which form a grid of bins with equal size in the $x' - Q'^2$ -plane. The bins divide the range between $x' = 0.2$ and $x' = 0.45$ into five equidistant bins and the range between $Q'^2 = 60 \text{ GeV}^2$ and $Q'^2 = 160 \text{ GeV}^2$ also in five equidistant bins. For each bin separately, the combinatorial cut method is used to find the best combination of cuts which gives the highest separation power at an instanton efficiency of $\epsilon_{\text{INS}} \gtrsim 10\%$ for the type of instanton-induced event corresponding to the given kinematics. The results are shown in figure 6.22 and the detailed numerical values are collected in Appendix B as table B.3. Like in the fiducial region, the CDM model predicts a larger number of background events as compared to the MEPS model which leads to cross-section limits which are in general a factor of two smaller. Because of the large disagreement between the two standard DIS models, background model independent cross-section limits are extracted by setting the number of background events to zero. This is shown as the filled area in figure 6.22. Depending on the kinematical region, cross-sections between 65 pb and 1100 pb can be excluded.

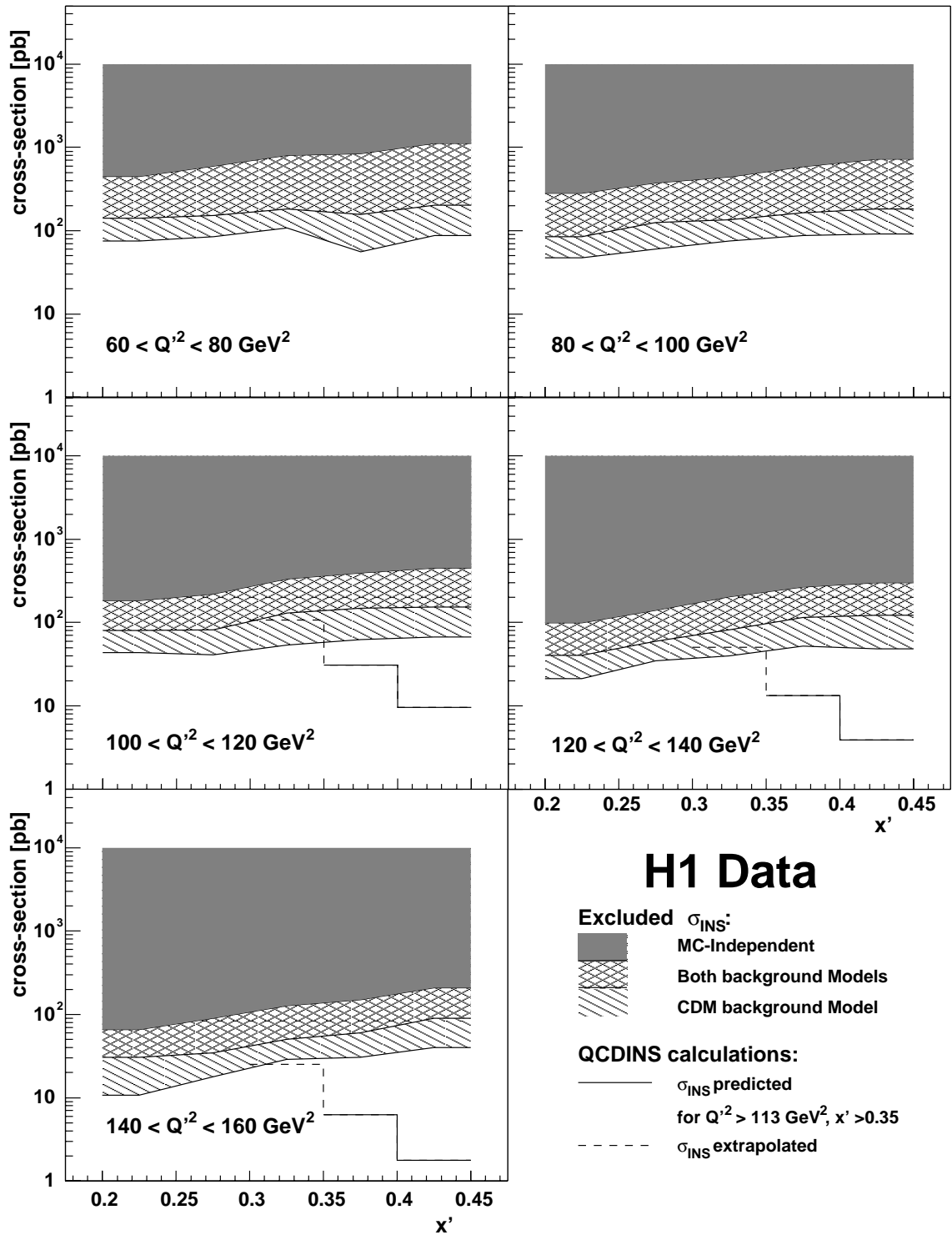


Figure 6.22: 95% confidence limits on the instanton-induced cross-section derived from the H1 data in bins of x' and Q'^2 .

Figure 6.22 also shows the QCDINS calculations as a full line in the fiducial region and, assuming all assumptions of the calculation are approximately valid, extrapolated toward smaller x' as a dashed line. The upper limits are above the predicted instanton cross-section in the fiducial region $x' > 0.35$ and $Q'^2 > 113 \text{ GeV}^2$, even when only the Monte Carlo model with the smaller upper limits is taken into account. However, the data can exclude the steep rise of the instanton cross-section towards lower values of x' and Q'^2 , which is expected from a naive extrapolation of instanton perturbation theory (dashed line). This is the first experimental hint that the steep rise towards larger instanton sizes and smaller instanton distances predicted by instanton perturbation theory has to be attenuated. A confrontation of this observation with non-perturbative QCD simulations on a lattice will be presented in the next section.

6.7.3 Confrontation With Lattice Data

The limits that have been derived above in bins of x' and Q'^2 can be transformed into the $\rho^* - R/\langle\rho\rangle$ -plane in order to confront them with lattice data. Remember, that ρ^* is the effective instanton size which determines the integral in the instanton cross-section calculation (1.38) and R is the instanton- anti-instanton distance. Since the variables x' and Q'^2 are conjugate to $R/\langle\rho\rangle$ and ρ^* (see equation (1.41)), the limits can be directly mapped into the $\rho^*-R/\langle\rho\rangle$ -plane. However, the transformation is numerically very demanding. Fortunately, the QCDINS Monte Carlo generator calculates the mapping to the conjugated variables for every event. Modifying the QCDINS program such that for every event the effective ρ^* and $R/\langle\rho\rangle$ values are made available, allows to map the bins in x' and Q'^2 to the conjugate variables by sampling the bins with Monte Carlo generated events.

The result and the comparison with the lattice data of the UKQCD collaboration [13, 23] are shown in figure 6.23. Figures 6.23a and 6.23b show the instanton density in the vacuum, as calculated on the lattice using a zero flavour approximation, depending on ρ and $R/\langle\rho\rangle$. Shown as curves are the same variables as obtained by the two-loop perturbative QCD calculations [21]. By calculating the χ^2 of the perturbative calculations to the lattice data points, the limits of the validity of the I-perturbation theory $\rho \lesssim 0.35 \text{ fm}$ and $R/\langle\rho\rangle \gtrsim 1.05$ are derived [16]. Figure 6.23c is a zoom into the ρ -distribution to make the growing discrepancy between the perturbative calculations and the lattice data visible. Towards larger values of ρ , the perturbative calculation predicts a larger instanton density than is found in the lattice calculation. This reflects the expectation that for larger instanton sizes the perturbation theory is not reliable. The H1 data can exclude this rise as is shown in figure 6.23d, where the HERA cross-section limits are shown for two bins of $R/\langle\rho\rangle$, one just within the fiducial region, and one just outside of it: The limits for $1.06 < R/\langle\rho\rangle < 1.12$, which is in the fiducial region of perturbation theory, are shown in dark gray together with the QCDINS prediction, which is depicted as a full line. For $\rho^* > 0.36 \text{ fm}$, which is outside of the fiducial region, the data can exclude the predicted cross-section. However, in the fiducial region, i.e. $\rho < 0.35 \text{ fm}$, the QCDINS prediction cannot be excluded. The cross-section is also shown in the $0.99 < R/\langle\rho^*\rangle < 1.06$ range, slightly below the fiducial range $R/\langle\rho\rangle > 1.05$. Here, the large instanton cross-section can be excluded for $\rho^* > 0.34 \text{ fm}$.

6.8 Discussion and Summary

The main problem of the presented search for instanton-induced events in deep-inelastic scattering is, that due to the small cross-section of the instanton-induced events a very high background reduction of ≈ 1000 is necessary, so that after the instanton-enriching cuts only about one per mill of the events are left. Although an increasingly good knowledge of the hadronic final state of DIS events at HERA has been gathered in the past ten years, this understanding is far away from being able to explain such a small fraction of the phase space. The large differences of the two employed standard DIS models in the cut regions underline this. It remains an open question, whether higher order effects not included in the present simulations of the background could account for the excess of events seen in the data when using the MEPS Monte Carlo model. This is not contradicted by the fact that CDM seems to describe the data rather well without higher order effects, since the colour dipole model has many adjustable parameters, which were tuned to the data and could already simulate these higher order contributions.

While the large uncertainty of the background makes it impossible to find any clear evidence for instanton-induced events in the given phase space, nevertheless limits on the instanton-induced cross-section can be derived that are independent of the predictions of the standard DIS background models and only depend on the hadronic final state of instanton-induced events as described by the QCDINS Monte Carlo simulation. Assuming that in the small region of phase space that is selected by the combinatorial cut method and the multivariate discriminant at most all events found in the data are instanton-induced events, an upper limit for the instanton cross-section of 221 pb can be excluded in the fiducial region of perturbative QCD at a confidence level of 95%.

Another aspect of the search is the dependence on the x' and Q'^2 distribution, calculated by instanton perturbation theory, for the simulation of instanton-induced events in DIS. To reduce this dependence, events were simulated in small bins in the kinematic variables of the instanton subprocess x' and Q'^2 and cross-section limits in these small bins calculated. These cross-section limits depend only on the final state of the instanton-induced event and not on the perturbative calculations of the x' and Q'^2 dependence, allowing to exclude instanton-induced cross-sections between 60 and 1000 pb, when using the MEPS model for the background.

One may also question, whether the hadronization of instanton-induced events can be described by the same fragmentation algorithms used in standard DIS, since the energy density of the instanton is much higher. While this might very well affect the expected multiplicities, it is expected that the current jet and the sphericity of the events are not affected. Therefore, at least some confidence in the robustness of the variables $Q_{\text{rec}}'^2$ and Sph_B appears justified.

The key to find evidence for instanton-induced events lies in understanding standard DIS better. Hopefully, better Monte Carlo simulations will be available in some years. Possible progress may result from the inclusion of higher order matrix elements matched to parton showers. It may also be possible to find instanton-induced events at higher values of Q^2 , where the understanding of the hadronic final state should be better, since low x effects and effects due to higher order QCD processes are less pronounced. An outlook on the prospects of such a search is given in chapter 8.

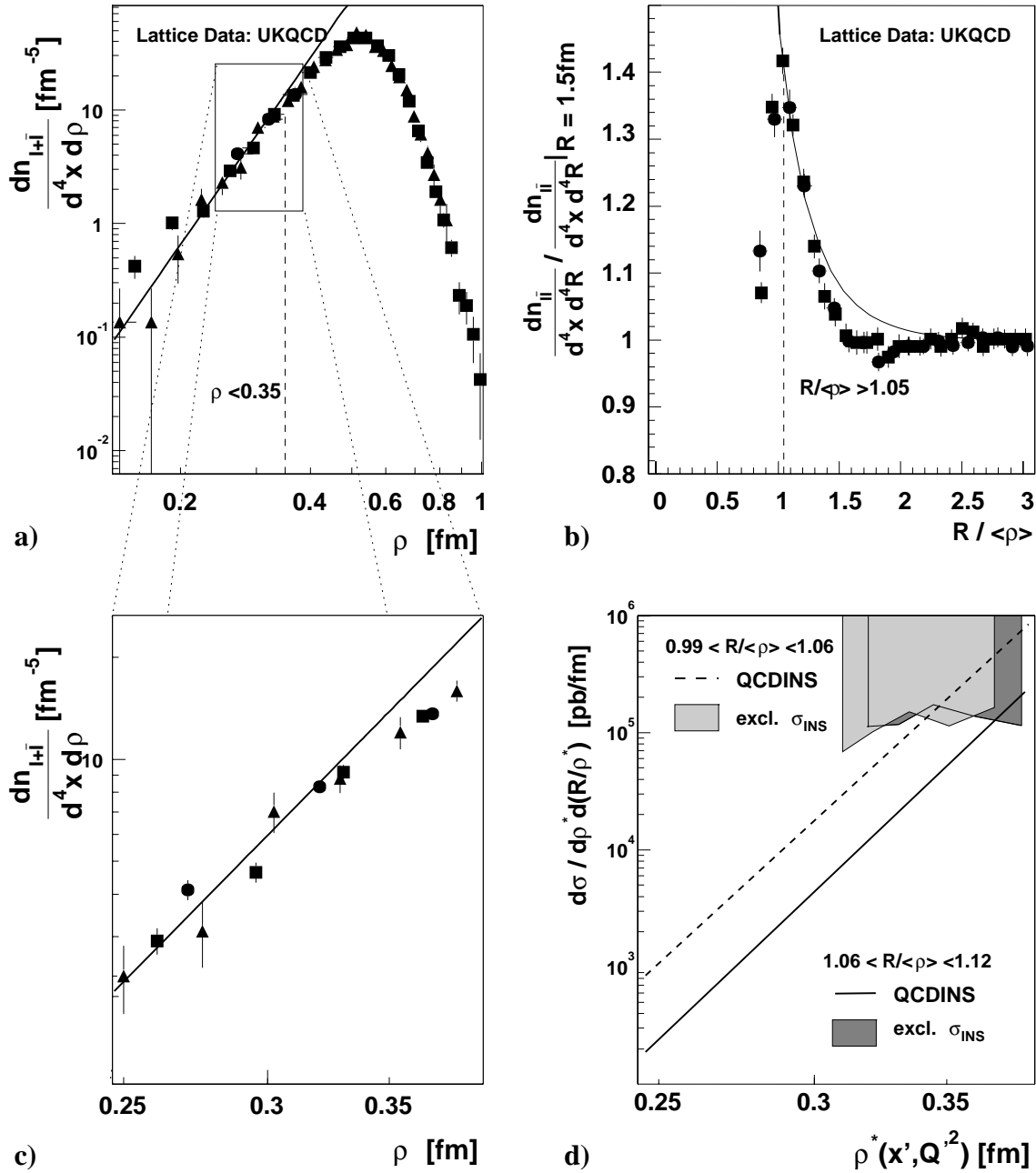


Figure 6.23: In a) the instanton density distribution as a function of the instanton size ρ and in b) the distribution in $R/\langle\rho\rangle$ as simulated on a lattice by the UKQCD collaboration [13, 23] are shown together with the 2-loop QCD-prediction [21]. In c) a zoom of the region in ρ is shown, where the perturbative QCD-prediction and the lattice simulation start to diverge. Note that these three distributions refer to calculations of the QCD vacuum. Finally, in d) the double differential cross-section limits of the H1 data, assuming the DIS background is described by the MEPS model, are shown together with the corresponding instanton cross-section as calculated by QCDINS in two bins of $R/\langle\rho\rangle$.

Chapter 7

Reconstruction of Instanton Kinematics

The importance of the kinematic variables Q'^2 and x' for the phenomenology of instanton was already mentioned in chapter 1. These variables relate the instanton transitions in deep-inelastic scattering to the instanton size ρ and the instanton anti-instanton distance distribution $R/\langle\rho\rangle$, which appear in calculations and simulations of the QCD vacuum. These are the variables that are naturally introduced by non-Abelian field theories in space-time coordinates.

In this chapter, the reconstruction of these crucial variables will be studied in more detail. First, the reconstruction of the variables as used in the search for instantons presented in the previous chapter is investigated. However, the reconstruction of the kinematics of the instanton subprocess performed for the purpose of finding observables that have a high discriminating power against standard DIS background events is not optimal as we will see in the second section (section 7.2). Here, a more refined strategy to reconstruct the kinematics will be presented, which will also use the range searching algorithm in an innovative way to search for the correct current jet.

7.1 Reconstruction of x' and Q'^2

The reconstruction of Q'^2 is straightforward and was already described in section 6.2.1. By finding the current jet and determining its four-momentum, Q'^2 is given by

$$Q_{\text{rec}}'^2 = -q_{\text{rec}}'^2 := -(q - q_{\text{rec}}'')^2 \quad , \quad (7.1)$$

where $Q_{\text{rec}}'^2$ is the reconstructed virtuality of the quark entering the instanton subprocess and q_{rec}'' the four-momentum of the current jet.

The problem is to find the correct jet and to reconstruct its four-momentum, under the circumstance that the jet has a high probability to lie in the same region as the instanton band. Therefore, the jet algorithm, which collects hadronic final state objects into a jet (see section 6.2.1), will pick up more objects than actually belong to the jet and thus will overestimate the jet energy. This problem has been intensively studied in [84] and was solved by using a relatively small cone size for the CDF-CONE jet algorithm. The cone size gives the maximum distance in the $\eta - \phi$ -plane an object is allowed to have with respect to the jet-axis in order to be collected into the jet. The definition used for the current jet

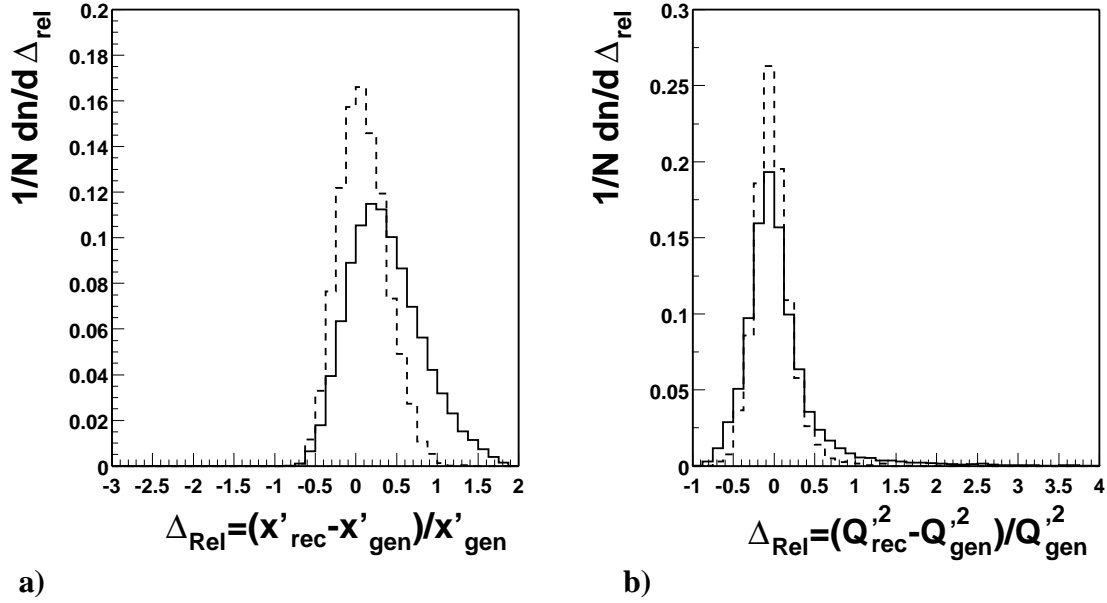


Figure 7.1: a) shows the quality of the reconstruction of x' for all events (full line) and the events selected by the cut on the discriminant $D > 0.988$ (dashed line). b) shows the same for the reconstruction of Q^2 , before and after a cut on the discriminant D .

in the experimental search described in the previous chapter, was to take the highest E_t jet in the hadronic CMS with a cone-radius of $R = 0.5$ as proposed in [84]. In section 7.2 another, improved method will be presented to find the current jet and to reconstruct its four-momentum.

The reconstruction of x' is not as easy as the reconstruction of Q^2 . If one inserts into the definition of x'

$$x' := \frac{Q^2}{2g \cdot q'} \quad (7.2)$$

the term $2g \cdot q'$, which can be expressed in terms of Q^2 and the invariant instanton mass squared W_I^2 , which is given by definition

$$W_I^2 := (g + q')^2 \approx -Q^2 + 2g \cdot q' \quad , \quad (7.3)$$

one obtains for x' :

$$x' = \frac{Q^2}{W_I^2 + Q^2} \quad . \quad (7.4)$$

Thus, reconstructing the virtuality of the current jet and the invariant mass of the objects belonging to the instanton subprocess allows to reconstruct x' .

The invariant mass of the instanton is given by the invariant mass of all particles belonging to the instanton band. It is defined as a band of 2.2 units of pseudo-rapidity with a mean $\bar{\eta}$, which is given by the iterative procedure defined by (6.3) and (6.4).

Figure 7.1a shows the distribution of the relative error of the reconstruction of x'

$$\Delta_{\text{Rel}} x' = \frac{x'_{\text{rec}} - x'_{\text{gen}}}{x'_{\text{gen}}} \quad (7.5)$$

for the sample of all instanton-induced events generated by QCDINS. The generated events have been processed with the H1 detector simulation and are the same as used in the previous chapter. For the full set of events (shown as a dashed line) $\Delta_{\text{Rel}}x'$ has a mean of 0.36 and an RMS of 0.45, which is a very bad reconstruction. The relative error

$$\Delta_{\text{Rel}}Q'^2 = \frac{Q'^2_{\text{rec}} - Q'^2_{\text{gen}}}{Q'^2_{\text{gen}}} \quad (7.6)$$

of the reconstruction of Q'^2 is shown in figure 7.1b. Here, the reconstruction of Q'^2 for the full data set is much better than in the case of x' ; the mean relative error is only 0.06 and the RMS is given by 0.49.

Shown as full lines in figures 7.1a and 7.1b are the reconstruction of x' and Q'^2 after the cut on the discriminant $D > 0.988$. In both cases the reconstruction improves:

$$\langle \Delta_{\text{Rel}}x' \rangle = 0.09 \quad \text{RMS}(\Delta_{\text{Rel}}x') = 0.29 \quad (7.7)$$

and

$$\langle \Delta_{\text{Rel}}Q'^2 \rangle = -0.02 \quad \text{RMS}(\Delta_{\text{Rel}}Q'^2) = 0.25 \quad (7.8)$$

However, the reconstruction of Q'^2 is still better than the reconstruction of x' since in addition to finding and reconstructing the kinematics of the current jet also the correct reconstruction of the instanton mass is necessary. Because in a detector particles can always escape, this is a much more difficult task. The improvement due to the cut on D shows that only instanton-like events have been selected by the discriminant, which share the expected kinematics of instanton-induced events. For these events a reconstruction of x' and Q'^2 is therefore possible with a sufficient resolution.

In the next section, an improved reconstruction of the current jet is investigated, from which both kinematic variables of the instanton subprocess can possibly profit.

7.2 Improvements in Reconstruction

The key to reconstruct the kinematics of the instanton subprocess is to correctly identify the current jet and measure its four-momentum. The correct identification of the jet and its properties can be checked by studying Monte Carlo generated events with the simulated response of the H1 detector as well as the information on the partons generated in the instanton-induced deep-inelastic scattering. By matching the direction of the jet-axis in pseudo-rapidity η and azimuth ϕ to the direction of the current quark, the correct jet can be identified.

In figure 7.2 the information obtained by such a matching of the jet to the current quark is shown. In figure 7.2a the reconstructed over the true transverse energy of the jet (taken to be the transverse energy of the current quark) $\frac{E_{t,\text{jet.rec}}}{E_{t,q}}$ is shown as a function of the pseudo-rapidity of the reconstructed jet η_{jet} in the hCMS¹. The distribution falls slowly towards large values of η_{jet} until $\eta_{\text{jet}} \approx 2.7$, where the slope becomes much steeper. This corresponds

¹Since the pseudo-rapidity of the jet is matched to the pseudo-rapidity of the current quark, for simplicity η_{jet} will be written for both in the following.

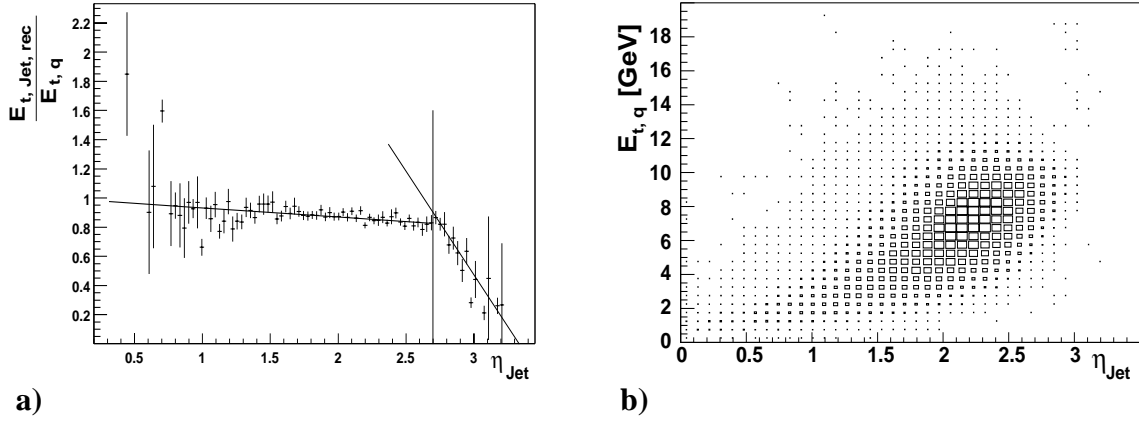


Figure 7.2: a) shows the ratio of the reconstructed transverse energy $E_{t, \text{jet, rec}}$ of the jet to the generated transverse energy $E_{t, q}$ of the current quark versus the pseudo-rapidity of the jet in the hCMS. b) shows the correlation of $E_{t, q}$ and the pseudo-rapidity of the true jet η_{jet} .

to the degraded acceptance of the detector in the very backward part of the liquid Argon calorimeter. Here, the backward end-cap of the LAr calorimeter has no hadronic section and the SpaCal is only two interaction lengths λ deep. Such an event, where the current jet seems to punch through the LAr calorimeter is shown in figure 7.3. Also shown (in figure 7.2) are two fitted lines to the ratio of the reconstructed transverse energy of the jet and the generated transverse energy of the current quark

$$\frac{E_{t, \text{jet, rec}}}{E_{t, q}}(\eta_{\text{jet}}) = \begin{cases} 1.0 - 0.06\eta_{\text{jet}} & , \eta_{\text{jet}} < 2.7 \\ 4.7 - 1.4\eta_{\text{jet}} & , \eta_{\text{jet}} \geq 2.7 \end{cases} . \quad (7.9)$$

The four-momentum of the current jet has to be rescaled (divided by the ratio) to obtain a better measurement in the backward region.

Figure 7.2b shows that the transverse energy of the generated current quark is correlated to the pseudo-rapidity of the quark in the hCMS. This correlation can be exploited by calculating the transverse energy and pseudo-rapidity of all jets found in the event by the jet-algorithm and take the most probable one according to the density of current quarks in the $E_{t, q} - \eta_{\text{jet}}$ -plane as shown in figure 7.2b. Instead of parametrising the two-dimensional distribution, the range searching algorithm is used. Only one binary tree is used to store the $E_{t, q}$ and η_{jet} values of 45000 QCDINS generated events. Then, for all current jet candidates of an event, the number of events found in the vicinity of the event in the $E_{t, q} - \eta_{\text{jet}}$ -plane is calculated. The box used had edges of 0.2 units in rapidity and 1 GeV in $E_{t, q}$. Before matching, the transverse energy of the jet is scaled by (7.9). The jet candidate with the most matched current jets in its vicinity as predicted by the QCDINS Monte Carlo becomes the current jet.

The improvement in the reconstruction of the jet only pays off slightly in the reconstruction of Q'^2 , as can be seen in figure 7.4, where the large tail towards larger $\Delta_{\text{Rel}}Q'^2$ can be

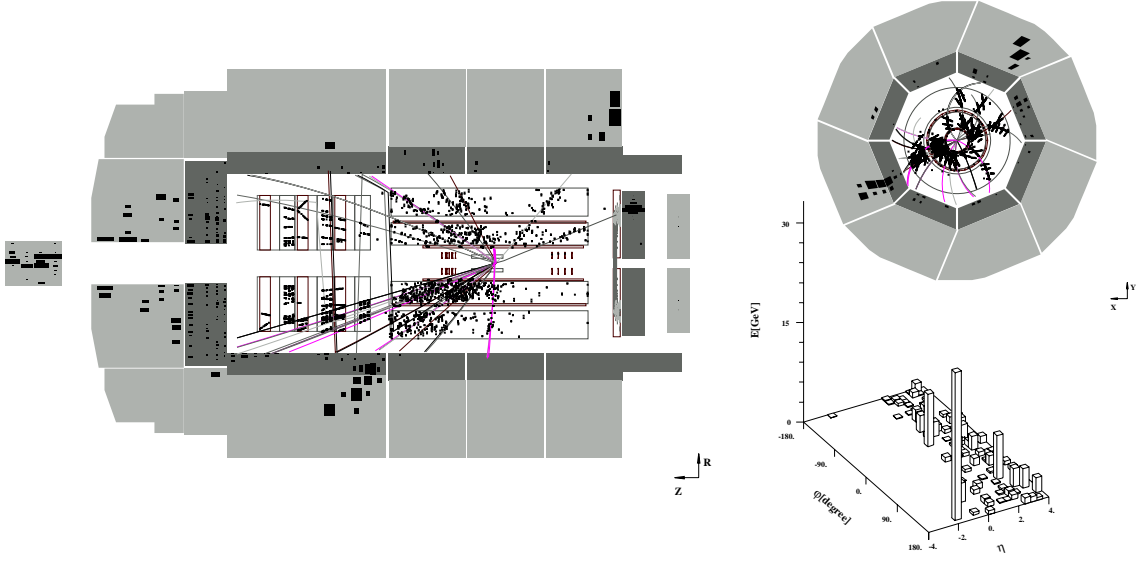


Figure 7.3: A data event selected by the cut on the discriminant $D > 0.988$, where a jet punches through the backward part of the liquid argon calorimeter. In such a case not all the energy of the jet is measured.

	Δ_{rel} (default)	Δ_{rel} (default, $D > 0.985$)	Δ_{rel} (improved jet selection)
x'	0.36 ± 0.45	-0.09 ± 0.29	0.37 ± 0.48
Q'^2	0.006 ± 0.49	-0.02 ± 0.25	0.0 ± 0.33

Table 7.1: Comparison of the reconstruction of x' and Q'^2 using the default method, the default method with the selection cut on the discriminant $D > 0.985$ and the improved jet selection scheme.

suppressed. The quality of the reconstruction of x' does not change, since here the measurement of all the particles in the instanton band are necessary which was not improved.

A comparison of the reconstruction of x' and Q'^2 is given in table 7.1. As can be seen, only the cut on the discriminant is able to improve the reconstruction of x' , while the reconstruction of Q'^2 improves also by employing the improved jet-selection. A successful reconstruction of x' therefore remains a problem which has not yet been solved. The key to this problem is the correct identification of all hadrons belonging to the instanton band, which is more difficult than the measurement and identification of the particles belonging to the jet. However, because x' is related to the instanton anti-instanton distance R , which is crucial to the properties of the instanton process, this task will need more attention in the future.

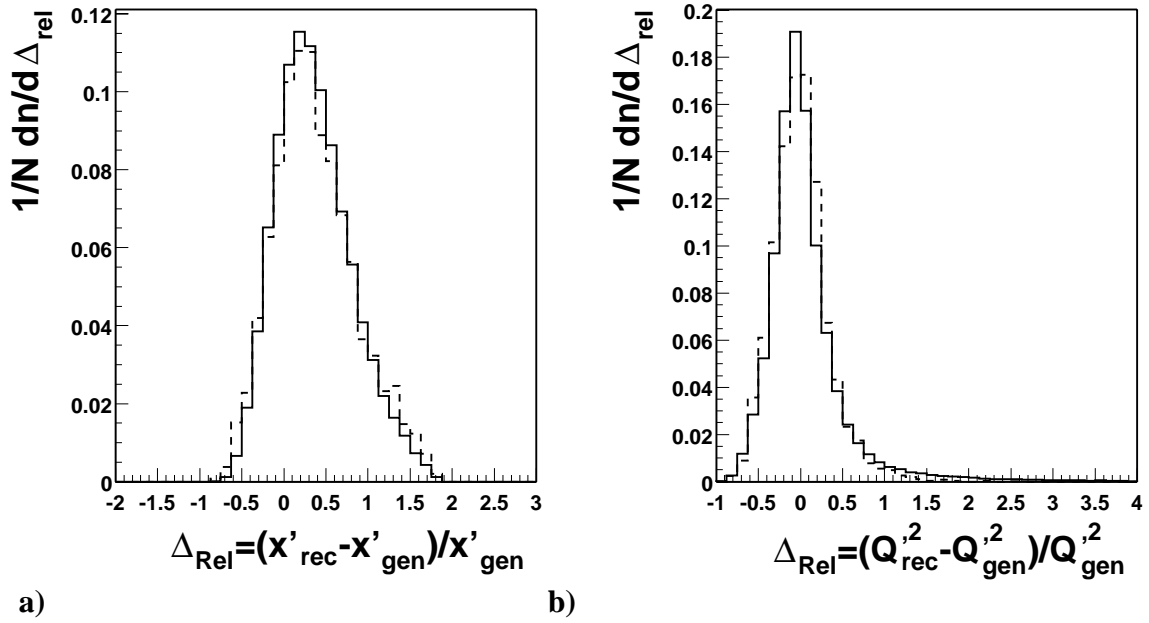


Figure 7.4: a) shows the reconstruction of x' without (full line) and with (dashed line) the improved jet-selection scheme. In figure b) the same is shown for the reconstruction of Q'^2 . Only the Q'^2 reconstruction improves when using the enhanced jet-selection scheme: Without improved jet-selection: $\langle \Delta_{\text{Rel}} x' \rangle = 0.36$, $\text{RMS}(\Delta_{\text{Rel}} x') = 0.45$ and $\langle \Delta_{\text{Rel}} Q'^2 \rangle = 0.06$, $\text{RMS}(\Delta_{\text{Rel}} Q'^2) = 0.48$. With improved jet-selection: $\langle \Delta_{\text{Rel}} x' \rangle = 0.37$, $\text{RMS}(\Delta_{\text{Rel}} x') = 0.49$ and $\langle \Delta_{\text{Rel}} Q'^2 \rangle = 0.0$, $\text{RMS}(\Delta_{\text{Rel}} Q'^2) = 0.33$. The improvement in the reconstruction of Q'^2 is mainly due to a smaller tail at higher $\Delta_{\text{Rel}} Q'^2$, since the variance of a Gaussian fit in the range -1 to 1 only improves from 0.28 to 0.27.

Chapter 8

Outlook on Searching for Instantons at High Q^2

The experimental search, which was presented in the previous two chapters neglected a cut on a minimum value of $Q^2 \approx Q_{\min}^2 = 113 \text{ GeV}^2$, which was advocated [11, 16] to reduce the theoretical uncertainties due to non-planar diagrams (see section 1.5). It was argued in [16] that the variables chosen in the experimental search are unaffected by this additional cut. However, to be able to reject or confirm the most recent cross-section prediction (1.45), it is necessary to also include this cut. Unfortunately, the change to higher values of Q^2 requires an entirely new experimental analysis, since the electron is scattered in this kinematical regime into the liquid Argon calorimeter of the H1 experiment and not into the SpaCal. This entails different requirements for the triggering conditions, a different event selection and the inclusion of the forward tracking system of the H1 detector, because of the boost of the instanton final state into the forward region.

In this chapter an outlook¹ on such a comprehensive search is given, where hadron level Monte Carlo simulations will be used to study the instanton final state and the expected standard DIS background. Because the final states of instanton-induced processes and standard DIS processes are expected to be more similar, more or different observables characteristic for instanton processes will be necessary to increase the separation power. A comprehensive search for such variables will be described in the first section of this chapter. The prospects of an experimental search using the data so far collected with the H1 detector are studied in section 8.2. The screening of suitable observables in the high Q^2 regime will also serve as a means to study the properties of the range searching method with a complex problem, and comparisons will be made to the result obtained with a neural network (section 8.3). Finally, section 8.2 summarises the prospects of a search for instantons at $Q^2 > 100 \text{ GeV}^2$ at HERA.

8.1 Screening of Suitable Variables

As a first step in this analysis for $Q^2 > 100 \text{ GeV}^2$, suitable variables have to be found, which allow the discrimination of instanton-induced events from standard DIS background events. Suitable means here that the variables should have a high separation power and result in a

¹This work was first presented in [100].

minimal model uncertainty of the instanton model as well as of the standard DIS background Monte Carlo simulations. The uncertainty of the background was modelled by four different Monte Carlo simulations. These are the ARIADNE generator (referred to as CDM in the previous sections), the LEPTO generator implementing the MEPS model, the RAPGAP Monte Carlo generator (which also implements the MEPS model and was therefore referred to as MEPS in the previous sections) and finally HERWIG that also implements the MEPS model². All generators were used in versions tuned to describe representative hadronic final state quantities in the range $Q^2 > 100 \text{ GeV}^2$ at HERA [94]. As the default background model, which is used to define the discriminant, the ARIADNE model is employed, which gives a good description of the H1 data at high Q^2 [94].

As in the case of the detector-level study at low Q^2 , prior to defining instanton discriminating variables, the kinematics of the instanton-induced events have to be reconstructed. Again, first the current jet is reconstructed. It is defined to be the highest E_t jet in the hCMS, where the cone radius of the employed CONE algorithm is $R = 0.5$ and the minimum transverse energy of the jet is $E_{t,\text{min}} = 1 \text{ GeV}$. The band is defined by $\bar{\eta} \pm 1.1$, where $\bar{\eta}$ is the E_t weighted mean pseudo-rapidity of all hadronic final state particles not associated to the current jet. In the forward region a cut at $\theta > 4^\circ$ is applied on the hadronic final state objects as well as the charged particle tracks to simulate a typical detector acceptance.

8.1.1 Definition of Observables

Using the above definitions of the current jet and the instanton band in the hadronic CMS, instanton discriminating observables are defined. Q_{rec}^2 is defined as in section 6.2 and the reconstructed x' as in section 7. Also the transverse energy and the multiplicity of the band $E_{t,b}$ and n_b as well as the transverse energy of the jet $E_{t,\text{Jet}}$ are treated as discriminating variables.

Several variables were used to study the shape of the hadronic final state. They are all used in more than one frame of reference and for different selections of the hadronic final state objects. The exact definitions for a particular choice can be found in section 6.2.2 and shall not be repeated here. The definitions of the frames of reference and the selection of hadronic objects will be given further down.

The sphericity S_{ph} has also been used in the search at low Q^2 and is defined in (6.6) and (6.7).

The isotropy variables E_{in} and E_{out} as defined by (6.8). These variables, too were already introduced in the experimental search, but only used to define the isotropy variable Δ_B (6.8) and not considered individually as discriminating observables. An interpretation of these variables is given in figure 6.9.

The isotropy variable Δ was used already in the search at low Q^2 and is defined in (6.8). For an interpretation see figure 6.5.

The normalised Fox-Wolfram moments H_{l0} have been introduced in [101] by G. Fox and St. Wolfram. The Fox-Wolfram moments are defined with the help of the LEGENDRE-

²See chapter 4 for a description of the Monte Carlo generators and the appropriate references.

polynomials P_l as

$$H_l := \sum_{i,j}^N \frac{|\vec{p}_i||\vec{p}_j|}{E_{\text{tot}}^2} P_l(\cos\phi_{ij}) \quad , \quad (8.1)$$

where the sum runs over all pairs (i, j) of hadronic final state objects with momenta $\vec{p}_{i,j}$. ϕ_{ij} is the angle between these objects and E_{tot} the sum of the energies of the final state objects.

In contrast to the variables E_{in} and E_{out} defined above, the Fox-Wolfram moments are independent of an axis which makes the calculation easier. The moments have values between 0 and 1 due to the normalisation of the LEGENDRE-polynomials and the overall normalisation by E_{tot} . If the sum of all outgoing momenta vanishes $\sum \vec{p}_i = 0$, which requires that the event is entirely contained in the detector, it can be shown that $H_0 = 1$ [101]. For events where not all outgoing particles are measured, it is recommended to use the ratio with the zeroth Fox-Wolfram moment:

$$H_{l0} := \frac{H_l}{H_0} \quad (8.2)$$

In the screening of observables the first four normalised Fox-Wolfram moments were considered.

All of the above variables were calculated within several frames of reference for different selections of hadronic final state objects:

- All particles in the hadronic CMS.
- All particles, except for the particles associated with the current jet in the hCMS within a band with a width of 2.2 units of rapidity around $\bar{\eta}$.
- All particles not associated with the current jet in their centre of mass system.
- All particles, except for the particles associated with the jet, within a band of 2.2 units of rapidity around $\bar{\eta}$. The calculation of the shape variables is performed in the centre-of-mass system of these particles.

In addition to the event-shape variables and the reconstructed kinematic variables of the instanton subprocess, other variables, which are readily available to a hadron-level study, like the number of charged K^\pm and neutral K_s^0 found in the band-region were studied. In total more than 60 variables were defined and investigated.

8.1.2 Screening of the Variables

Of the variables defined above, 35 were chosen because of their potential to discriminate against the background or due to physics considerations. The discriminants based on all combinations of two of these variables were calculated. The discriminant was defined using 10000 events each of the background and signal. The size of the box, in which events were counted around an event that is to be classified, was fixed by assigning to every observable a typical scale — the range one would normally use to plot this variable — and by setting

the box-size to be one tenth of this scale. As was shown in section 3.4.2, the box-size is not critical to obtain a discrimination close to the optimum. This allowed an automatic calculation of the 595 discriminants.

After comparing the average performance of the variables in the discriminants, twelve variables were chosen to be studied further. The selection criteria for these variables were their average separation power as well the requirement to have different variables, which describe the characteristic shape and kinematics of instanton-induced events. For example, an observable defined in more than one frame of reference was taken only once.

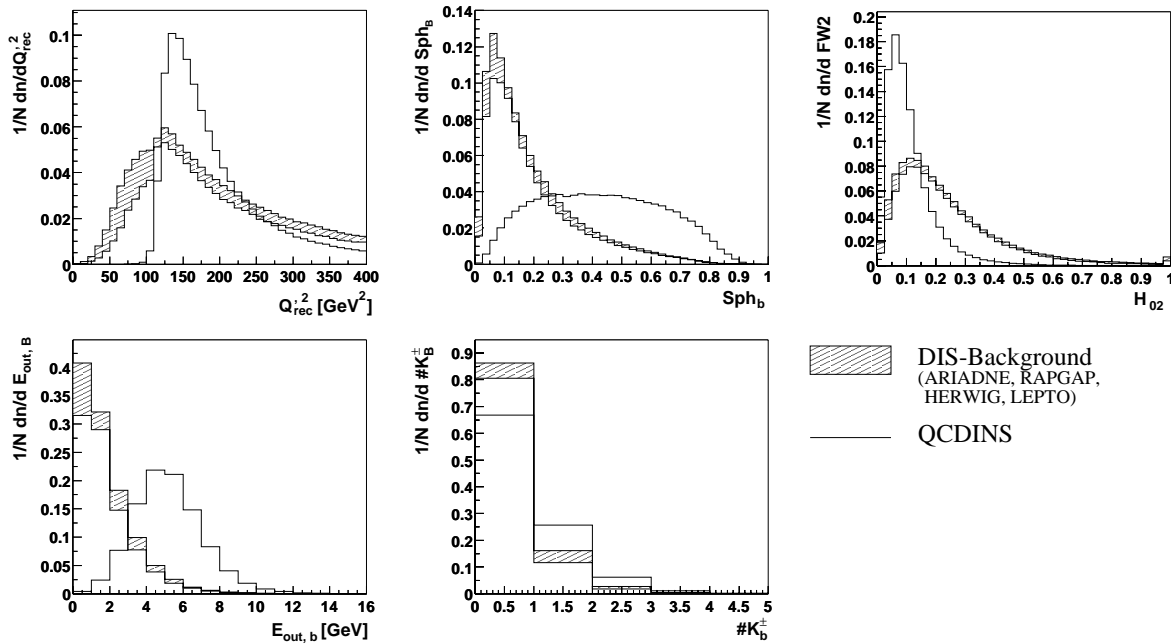


Figure 8.1: The five discriminating variables at high Q^2 : The reconstructed virtuality squared of the quark entering the instanton subprocess Q_{rec}^2 , the sphericity Sph_b , the second Fox-Wolfram moment H_{02} and $E_{\text{out},b}$ of the instanton band (in the rest-system of the band), and the number of charged kaons in the band $\#K_b^\pm$.

The selected variables were the transverse energy $E_{t,\text{Jet}}$ of the current jet and of the instanton band $E_{t,b}$ in the hCMS and Q_{rec}^2 , x'_{rec} as defined in (7.4), the sphericity Sph_b , the isotropy variables $E_{\text{in},b}$, $E_{\text{out},b}$, Δ_b , the second Fox-Wolfram moment H_{20} defined in the rest system of the instanton band, the charged particle multiplicity n_b , and the charged kaon multiplicity $\#K_b^\pm$ in the instanton band. As an additional shape-variable, the sphericity Sph of all hadronic final state particles except the current jet in the hCMS was chosen. The last observable is the instanton mass, which is given by the invariant mass of the sum of all hadronic final state objects found in the instanton band.

To find the combination of variables with the highest separation power, and which is in addition based on observables characterising different features of instanton-induced events, all combinations of five of the variables were used to define discriminants employing the

range searching method. The separation power of all $\binom{12}{5} = 792$ combinations at a minimum instanton efficiency of $\epsilon_{\text{ins}} > 10\%$ was calculated and the uncertainty in the background modelling of the most promising combinations was studied further with the help of all four standard DIS Monte Carlo generators.

The distributions of the instanton-induced events and standard DIS background events of the selected combination of five discriminating variables is shown in figure 8.1. The selected variables are the reconstructed virtuality of the quark entering the instanton subprocess $Q_{\text{rec}}^{\prime 2}$, the sphericity Sph_b , the second Fox-Wolfram moment H_{02} , $E_{\text{in},b}$ of the band in its rest frame, and finally the number of charged kaons in the band $\#K_b^{\pm}$. Figure 8.2 shows the resulting discriminant. The instanton efficiency of $\epsilon_{\text{INS}} = 10\%$ is achieved by a cut $D > 0.985$, which provides a separation power of $S = 126$.

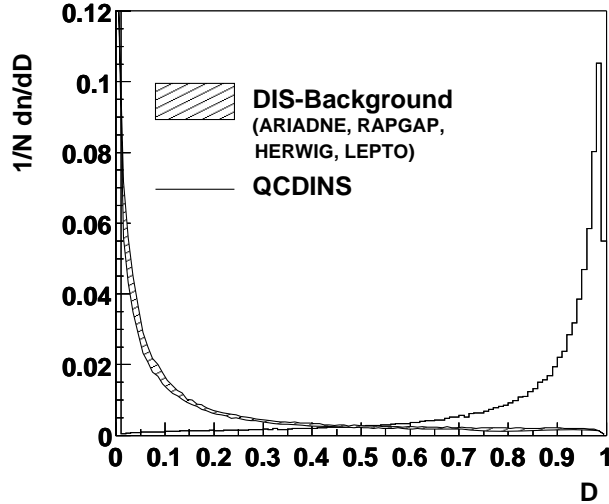


Figure 8.2: The figure shows the shape normalised distributions of the discriminant defined by the observables $Q_{\text{rec}}^{\prime 2}$, H_{02} , Sph_b , $E_{\text{in},b}$ and $\#K_b^{\pm}$ as explained in the text. The shaded area represents the uncertainty induced by the four standard DIS models ARIADNE, LEPTO, HERWIG and RAPGAP. The full line shows the distribution of QCDINS generated events.

It was also studied, whether any sixth variable could improve the separation power further. The most promising candidate is the transverse energy of the jet, shown in figure 8.3a. After a cut on the discriminant formed by the five chosen observables, the distribution of the instanton signal is still different from the background models (figure 8.3b). However, large discrepancies in the predictions of the background models are seen, which diminish the significance of the discriminant.

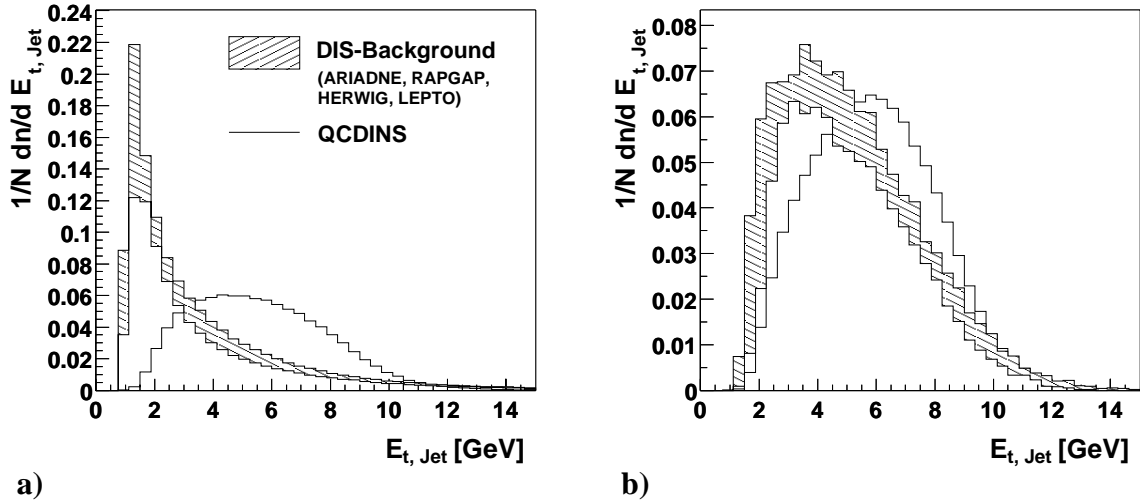


Figure 8.3: The distribution of $E_{t,Jet}$ shape normalised before instanton-enriching cuts in a) and after the cut on the discriminant in b). The distribution of the background shows a large model uncertainty.

8.2 Results

In this section, the prospects of a search in a kinematic region of $Q^2 > 100 \text{ GeV}^2$ will be studied, taking into account the luminosity collected by the H1 experiment so far.

Figure 8.4a shows the discriminant as defined in the previous section for the standard DIS background and for instanton-induced events. The plot is normalised to a luminosity of 100 pb^{-1} and indicates the region $D > 0.9$. The full line shows the QCDINS prediction. Cutting at $D > 0.985$ an instanton efficiency of $\epsilon_{\text{INS}} = 10\%$ is achieved, so that 178 instanton-induced events are expected in the cut-region. The hatched region shows the model uncertainty given by the standard DIS models ARIADNE, LEPTO, RAPGAP and HERWIG. Towards larger D , the predicted background contribution becomes smaller and the relative uncertainty decreases. This behaviour is achieved by choosing variables for the discriminant, which introduce only a minimum of model uncertainty of the background. The dashed curve is the sum of the mean background and the instanton signal distribution. Although the instanton-signal is located at a strongly decreasing part of the background distribution, a bump in the discriminant is predicted in the distribution of data events, if the predicted amount of instanton-induced events is found in the data. For $D > 0.985$ an instanton-contribution of roughly 50% is expected.

In figure 8.4b the expected significance of a possible instanton-signal in the high Q^2 regime is shown as a function of the cut value D_{cut} . The significance³ $S_I = n_I / \sqrt{n_{\text{BG}}}$ is given as the number of the expected instanton-induced events (n_I) over the square root of the number of background events (n_{BG}) in the cut region, which gives a measure of the statistical

³Other definitions of the significance exist, in particular one, which adds the number of signal events N_I in the square root to include the statistical error of the signal. For an overview and a comparison of the different definitions of the significance, see e.g. [102].

uncertainty of the background. The model dependency of the background is shown as the hatched area. The highest significance is expected at values of $D \approx 0.9$ where $S_I \approx 15$. Such a high significance would allow a clear statement on observing evidence for instanton-induced events. The large significance of more than three at a cut value of $D_{\text{cut}=0}$ can be explained by the lack of a systematic uncertainty assigned to the limited detector resolution. The expected instanton cross-section σ_{INS} of approximately 16pb is 0.5% of the neutral current standard DIS cross-section of $\approx 3000\text{pb}$ in the selected kinematical region. Given the luminosity of 100pb^{-1} , more than a three sigma effect is expected. However, the H1 experiment only measures the luminosity within 1.5% (see section 2.2.3), so that without any instanton-enriching cuts, no effect would be visible.

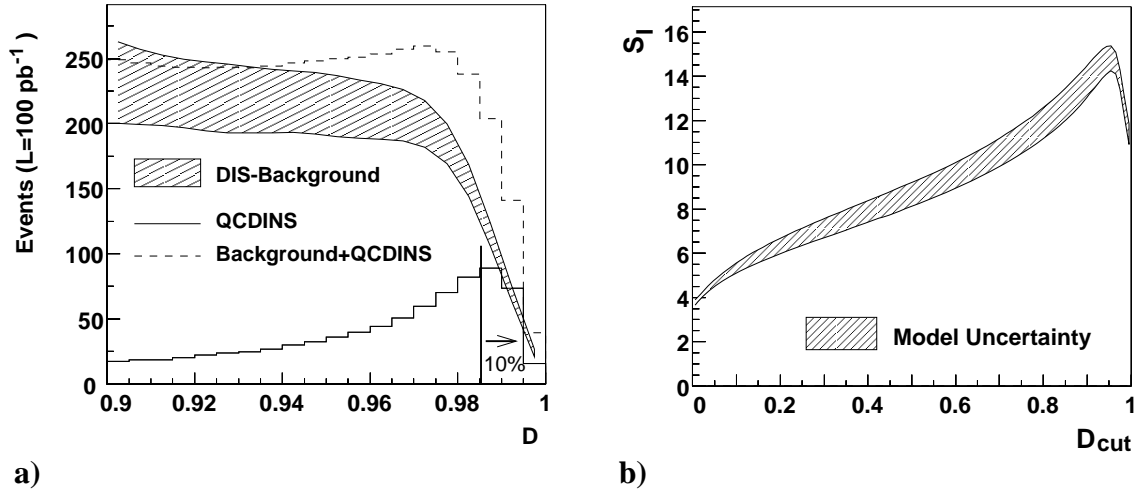


Figure 8.4: a) shows the $D > 0.9$ region of the discriminant distributions of the background (hatched region), the instanton-induced events (full line) and the sum of the mean background and instanton events (dashed line). The plot is normalised to a luminosity of 100pb^{-1} . In b) the expected significance S_I (see text) of a possible instanton-signal is shown as a function of D_{cut} .

In chapter 7, the reconstruction of x' and Q'^2 has been studied extensively for the low Q^2 detector-level QCDINS Monte Carlo. Figure 8.5 shows the reconstruction of the instanton kinematics in the high Q^2 case on hadron-level. As in the low Q^2 case, the reconstruction improves strongly if a cut on the discriminant is applied. Before the cut on D is applied, the mean of the relative errors is $\langle \Delta_{\text{Rel}} x' \rangle = (x'_{\text{rec}} - x'_{\text{gen}}) / x'_{\text{gen}} = 0.34$ and $\langle \Delta_{\text{Rel}} Q'^2 \rangle = 0.29$, with an RMS of 0.43 and 0.44. After the cut on $D > 0.985$, the relative error of the reconstruction of x' has a mean of 0.05 and an RMS of 0.20. The mean of the relative error of the reconstruction of Q'^2 is 0.13 and the RMS is 0.17.

The cut on the discriminant selects preferentially instanton-like events such that the assumption in the reconstruction that the kinematics of the event is instanton-like is valid leads to a good reconstruction of the kinematics. When comparing with the results from the previous chapter, it is necessary to point out that detector effects have not been simulated.

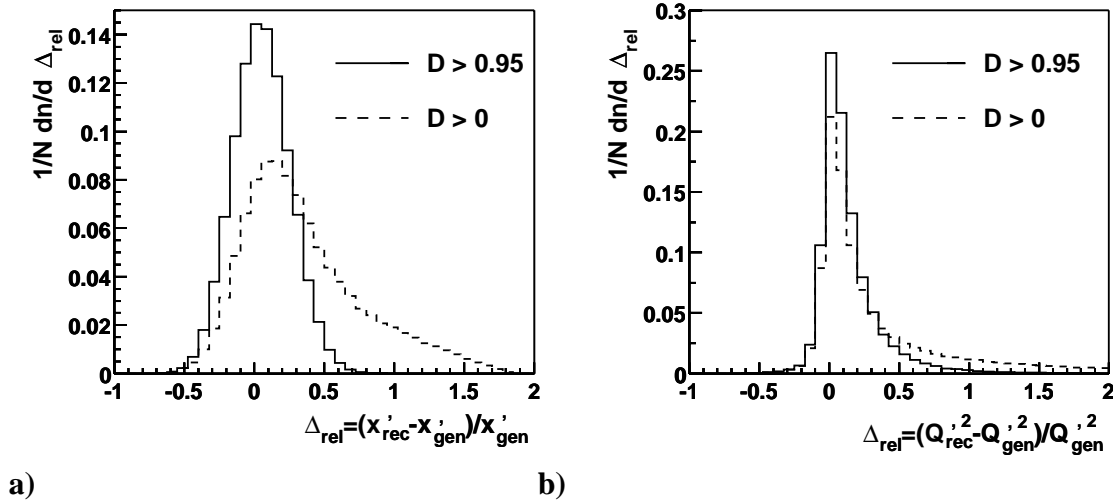


Figure 8.5: The reconstruction of x' (a) and Q'^2 (b) strongly improves, if a cut on the discriminant is applied. The relative errors of the reconstruction are shown as a full line after the application of the cut and without the cut as a dashed line. With a cut $D > 0.9$, the RMS of the reconstruction of x' is 0.20 and 0.17 for Q'^2 .

8.3 Study of Discriminant and Comparison with Neural Networks

The screening for appropriate observables with a high discrimination power for instanton-induced events and standard DIS background events at high Q^2 , offers also the opportunity to study the properties of the range searching algorithm and to compare the outcome with artificial neural networks. Five variables is a large enough number and the distribution of the events in variable space is complex enough for a comparison using a complex “real world” example. Only hadron-level Monte Carlo simulations are used, for which a large number of events can be generated in a short time. In addition, this large number of generated events can also be used to study the dependency of the range searching algorithm on the number of events in the binary trees.

In figure 8.6 the separation power of the discriminant is shown for an instanton efficiency of at least $\epsilon_{\text{INS}} = 10\%$ for 75, 150 and 300 thousand events in the binary trees and for different relative box widths. Relative box width means that the size of all the edges of the box are a fraction of the typical scales of the observable distributions as shown in figure 8.1. Towards small and large box-sizes, the separation power falls off, but has a plateau of a width of about half a magnitude, where the separation power does not change by more than 20%. The width of the plateau grows with the number of events in the binary trees for the classification of the events, because the larger number of events allows to use smaller box-sizes for classification, while retaining a sufficiently large number of events in the box. At large box-sizes, the separation power is independent of the number of events in the binary trees, because here, the resolution of the box-size limits the separation.

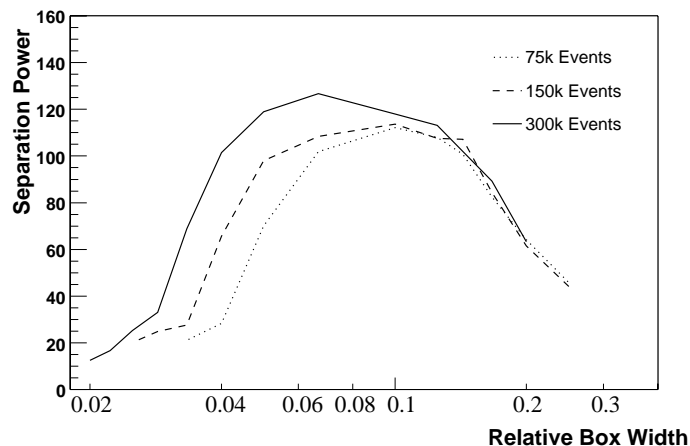


Figure 8.6: The separation power S at $\epsilon_{\text{INS}} = 10\%$ for different box-sizes and different numbers of events in the binary trees. Increasing numbers of events allow to reduce the size of the vicinity around an event leading to a larger maximum separation power.

For a comparison of the performance of the range searching algorithm to the performance of an artificial neural network, the same neural network simulator as described in section 3.3 is used. The high number of available training events allows to use a very large neural network. The network performing best is a single hidden layer network with five input nodes corresponding to the five input variables, 100 hidden nodes and a single output node. Different parameters of the back-propagation algorithm⁴ were tried and the best network selected.

The average output errors of the neural network during the training phase, which needed 600 cycles for the network to stabilise are shown in figure 8.7a. The large number of training cycles is made necessary by the size of the network. No sign of over-learning is visible, since the training and validation curves do not diverge. Thus, the number of events available for training is sufficient to adjust the large number of weights in the network. The background rejection of the trained network versus the signal efficiency is shown in figure 8.7b.

The distribution of the output of the neural network for the instanton-induced and the normal DIS background events is shown in figure 8.8 and looks similar to the distribution of events obtained by the range searching method (figure 8.2). However, the separation power at an instanton efficiency of 10% is only $S = 116$, which is smaller than in the case of the range searching algorithm. For a sufficiently large number of events such an outcome is expected, because a neural network only fits the phase space densities of the signal and background events while the range searching algorithm directly measures it.

Another aspect of event classification to be mentioned concerns the time consumption of the task. In the given example, the time to train the neural network using 300 thousand training and 300 thousand validation events took approximately four hours on a normal PC

⁴The momentum parameter, which enhances convergence, and a parameter that controls the jitter of the gradient vector to escape local minima were varied, see e.g. [54] for a detailed discussion on enhancements of the back-propagation algorithm.

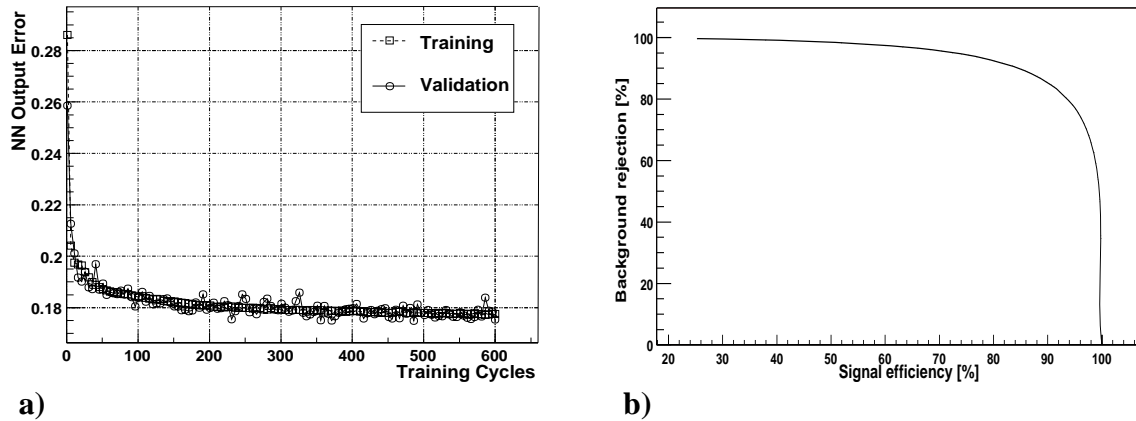


Figure 8.7: In a) the change of the average output error of the neural network during training is shown for the training and validation events. The training events are marked with boxes, the validation events are marked by circles. In b) the achieved background rejection is shown versus the signal efficiency.

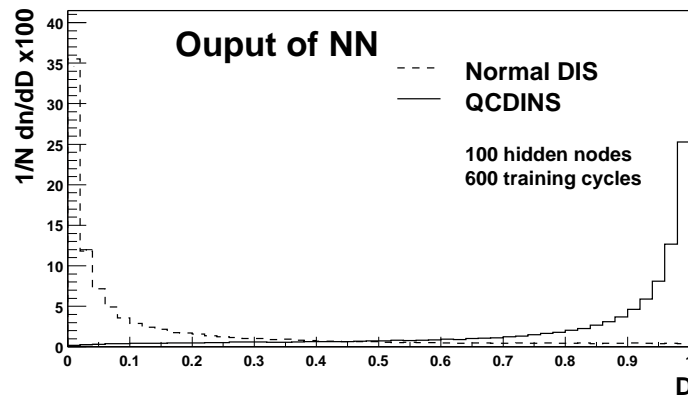


Figure 8.8: Output distributions of the best neural network for the normal DIS (dashed line) and QCDINS generated events (full line). The distributions are shape normalised.

workstation computer⁵. The same was achieved by the range searching algorithm within 20 minutes.

8.4 Conclusions

The exploratory study on finding instanton-induced events with the cross-section predicted by Ringwald and Schrempp in at HERA shows that such a discovery may be possible given the accumulated luminosity of the ZEUS or H1 experiments. By choosing a good combi-

⁵A standard Pentium III type system at a speed of 800MHz and a memory of 512Mb.

nation of observables, the model uncertainty of the expected background can be minimised, while maintaining a high separation power of the discriminant. In a region where the instanton efficiency is still 10%, a sample of events can be extracted, where 50% of the events are expected to be instanton-induced.

Due to the large number of Monte Carlo generated events and a sufficiently high complexity, the problem is also ideal to further study the properties of the range searching algorithm for a “real world” problem. The algorithm is stable with respect to the box-size for sufficiently high statistics. In general, a better separation can be achieved, if more events are stored in the binary trees for classification purposes.

When compared to an artificial neural network, the performance of the range searching algorithm is better, even for very large networks. In addition the computation time is more than an order of magnitude lower, which allows to search for better observables.

Chapter 9

Conclusions and Outlook

This analysis presents for the first time a dedicated search for QCD instanton-induced processes. For the search, data taken with the H1 detector at the HERA electron-proton collider in the years 1996 and 1997 was used. The data corresponded to an integrated luminosity of 21.1 pb^{-1} , and the kinematical range studied was limited by the Bjorken scaling variables $x > 0.001$, $0.1 < y < 0.6$ and $Q^2 < 100 \text{ GeV}^2$, and the scattering angle of the electron $\theta_e > 156^\circ$. Three observables were used to separate the instanton-induced events from the standard DIS background: the reconstructed virtuality of the quark entering the instanton subprocess Q_{rec}^2 , the sphericity Sph_B and the charged particle multiplicity n_B of the hadronic final state of the instanton subprocess. The separation between instanton signal and standard DIS background events was done using two different discrimination methods, one based on optimised cuts on the three observables and another which combined the observables into an innovative multivariate discriminant by employing a range searching algorithm.

With either of the two methods, a typical background reduction by a factor of 1000 was achieved, while 10% of the instanton-induced events were kept. After cutting on the three observables, 484 events are observed in the data, while 443_{-35}^{+29} events are predicted by the colour dipole model (CDM) simulation and 304_{-25}^{+21} by the more conventional leading-order matrix elements matched to parton showers (MEPS) model. By cutting on the multivariate discriminant, 410 events are observed in the data, while 354_{-26}^{+40} (299_{-37}^{+25}) events are expected by the CDM (MEPS) Monte Carlo. The results obtained by the two different discrimination methods are compatible. In both cases, a significant excess is observed when estimating the background with the MEPS model, while with the CDM model only a slight excess is seen. Since the differences of the two standard DIS background models are of the order of the excess seen by the MEPS model, no firm conclusions can be drawn.

The multivariate discriminant method allows to investigate the transition from the instanton-free, background dominated region to the instanton-enriched region. The MEPS model describes the data in the background region quite well. With increasing sensitivity to the instanton process an increasingly large excess is seen in the data. The shape of the excess is qualitatively comparable to the expected instanton signal. The colour dipole model does not describe the data well in the background region but also sees a slight excess there, where the sensitivity to the instanton process is highest. Altogether, despite some excess of events in the instanton signal region, the uncertainties of the background are too high to draw a clear conclusion. It must be noted, that the standard DIS models are known to have deficiencies

and fail to describe various aspects of the hadronic final state of DIS data in the HERA regime. A better understanding of the formation of the hadronic final state in general and in the phase space relevant for instanton searches will be needed to make further progress.

Assuming all events seen in the data are instanton-induced, a cross-section limit of 221 pb at 95% confidence level can be derived in the fiducial region of instanton perturbation theory $x' > 0.35$ and $Q'^2 > 113 \text{ GeV}^2$. This limit is independent of the modelling of the standard DIS background. It is about a factor of five above the cross-section predicted by Ringwald and Schrempp. To be independent of the assumptions entering the calculation of the x' and Q'^2 distributions, limits are derived based only on the instanton final state topology for fixed x' and Q'^2 . These limits cannot exclude the predicted instanton cross-section in the fiducial region, but exclude a steep rise of the cross-section towards decreasing x' , i.e. towards large instanton sizes, as would be obtained by a naive extrapolation of instanton perturbation theory.

Given today's understanding of the limitations of current instanton perturbation theory, it appears necessary to look for evidence for instanton-induced events in the region of high Q^2 ($Q^2 > 100 \text{ GeV}^2$). Here, a better understanding of the standard DIS background is expected. In an exploratory study, using hadron level Monte Carlo events but without simulation of detector effects, suitable observables could be identified which allow a reduction of the background by a factor of over 1200, while keeping 10% of the expected instanton-induced events. In addition, the identified observables minimised the model uncertainties of the background in the expected signal region. Assuming an integrated luminosity of 100 pb^{-1} of collected data, a clear instanton signal was visible, despite the uncertainties of the background.

Another objective of the thesis was to study the classification of events using an innovative method based on range searching. The method estimates the phase space density of signal and background events by counting the number of Monte Carlo simulated events in a small box. By employing a range searching algorithm, this can be done in a relatively short time. It was shown that the method can be easily and automatically used due to the insensitivity to the only free parameters of the algorithm, i.e. the size of the multi-dimensional box in which for a given data event, Monte Carlo events are counted. This property makes the method particularly suitable to screen large numbers of observables for those offering the best separation power. By using high statistics samples of the background and signal events, smaller box-sizes can be used leading to higher separation power of the discriminant. The performance of the method in terms of separation power is at least comparable to the performance of artificial neural networks. The algorithm promises to be an interesting classification method applicable also in other high energy physics analyses.

Instantons in QCD have a signature not present in perturbative QCD: they violate chirality. This has so far not been exploited, although proving the existence of a violation of chirality would offer unique evidence for the existence of instantons. An opportunity to find evidence for chirality violation may be provided by the self-analysing decays of Λ baryons, which allow to measure the chirality of the constituent strange quarks. Λ and $\bar{\Lambda}$ baryons would need to be identified, which are products of the hadronization of s and \bar{s} quarks from the instanton subprocess. With the help of powerful discrimination techniques, which provide data samples with a high contribution of instanton-induced events, finding such evidence for instantons could be within reach.

Appendix A

Implementation of the Range Searching Algorithm

The implementation of the range searching algorithm listed below uses two binary trees to store signal and background events in a pre-sorted way. It has a memory requirement of $4(d+5)n$ bytes on a 32 bit computer system, if n events with d observables are stored. Two pointers are necessary to link the daughter nodes to the parent node, where the observables and the weight of the event are stored. Two additional pointers, which are only used to simplify the implementation, store links to the Vector and Point objects storing the event data. As an example, the algorithm uses 240 megabyte of memory to store the 300000 signal and background events as used in the search at high values of Q^2 described in chapter 8.

The time consumption of the algorithm is roughly half an hour on an 800MHz Pentium type system, if 300000 events are classified. Most of the time is spent to count the events in the box, after the tree has already been descended to the region, where only candidates for the events in the box are found and an explicit test is necessary. The test whether an event is in the box is $2d$ times more time consuming than descending down the tree, because a comparison with all $2d$ boundaries of the box is necessary. Interestingly, this entails that the algorithm is nearly independent of the number of dimensions (the number of observables) and the number of events stored in the binary trees, since always a certain number of events is necessary in a box to have a sufficiently large statistics on which the classification is based. In practice, therefore, the time to classify one event is more or less independent of the dimension and the number of training events, but only depends on the required statistical uncertainty. Neglecting the statistical error, the algorithm is faster for higher dimensions, if the number of events is kept constant, because then fewer candidates for events in the box need an explicit check.

In the following, the source code is documented, starting with the C++ header file containing the definitions of the data structures:

```
// Definition of a point in the phase space
struct Point{
    Vector *v;                // A vector that can contain a point in
                            // the phase space
    float weight;           // The weight of the point/event
```

```

};

// Definition of a rectangle in which to search
struct Rectangle{
    Vector *lower;           // lower left edge
    Vector *upper;          // upper right edge
};

// The definition of the class of the multi-dimensional Binary
// Range sorter
class BinaryRangeSorter{
private:
    int numVars;            // Dimensionality of the phase space

    struct node{           // The node in the binary tree
        struct Point *p;
        struct node *l,*r; // left and right daughters
    };

    struct node *z, *head;
    Point dummy;
    bool insideRectangle(Point *p, Rectangle *range);
    void destroyNode(struct node *node);

public:
    float searchr(struct node *t, Rectangle *range, int d);
    BinaryRangeSorter(int n=0);
    ~BinaryRangeSorter();
    void insert(Point *p);
    float search(Rectangle *r);
};

```

A part of the code; first the user callable routines:

```

// The constructor, n is the dimension of the problem
BinaryRangeSorter::BinaryRangeSorter(int n){
    numVars=n;

    // Initialize head with a zero left daughter and a right dummy
    // daughter, the head is filled with the leftmost possible point
    // This decreases effort later significantly
    Vector *dp=new Vector(numVars);
    dummy.weight=1.;dummy.p=dp;
    for(int i=0;i<numVars;i++)
        (*dp)(i)=-FLT_MIN;

    z=new node();

```

124 APPENDIX A. IMPLEMENTATION OF THE RANGE SEARCHING ALGORITHM

```

z->p=0; z->l=z; z->r=z;

head=new node();
head->p=&dummy; head->l=0; head->r=z;
}

void BinaryRangeSorter::insert(Point *p){
    struct node *f=0,*t;
    int d,td=0;

    for(d=0,t=head; t!=z; d=(++d)%numVars){ // search where to insert node
        td=(*(p->v))(d) < (*(t->p->v))(d);
        f=t; // remember the current head
        t=td? t->l : t->r;
    }
    t=new node; // create the new node,
               // l,r pointing to tail z
    t->p=p;t->l=z;t->r=z;
    if(td)
        f->l=t;
    else
        f->r=t;
}

float BinaryRangeSorter::search(Rectangle *range){
    return searchr(head->r, range, 1);
}

```

The following code is the actual implementation of the algorithm:

```

bool BinaryRangeSorter::insideRectangle(Point *p,
                                         Rectangle *range){
    bool result=true;

    for(int i=0; i< numVars; i++){
        result = result && *(range->lower)(i) < *(p->v)(i);
        result = result && *(p->v)(i) <= *(range->upper)(i);
    }
    return result;
}

float BinaryRangeSorter::searchr(struct node *t,
                                 Rectangle *range, int d){
    float count=0.;
    bool tl, tr;

    if(t==z) return 0; // Are we at an outer leaf?

    tl=*(range->lower)(d) < *(t->p->v)(d); // Should we descend left?

```

```
tr=*(t->p->v))(d) <= (*(range->upper))(d); // or right?

// Sum up all points in the rectangle
if(tl) count += searchr(t->l, range, (d+1)%numVars);
if(insideRectangle(t->p, range)) count +=t->p->weight;
if(tr) count += searchr(t->r, range, (d+1)%numVars);
return count;
}
```

Appendix B

Exclusions Limits

	N	ϵ_{sDIS}	$S = \epsilon_{\text{INS}}/\epsilon_{\text{sDIS}}$	σ_{lim}
DATA	484			
CDM	443^{+29}_{-35}	0.118%	86	47 pb
MEPS	304^{+21}_{-25}	0.081%	125	109 pb
BG-Independent	BG=0			255 pb

Table B.1: The table summarises the results of the cut-based method including the instanton-induced cross-section limits at 95% confidence level.

	N	ϵ_{sDIS}	$S = \epsilon_{\text{INS}}/\epsilon_{\text{sDIS}}$	σ_{lim}
DATA	410			
CDM	354^{+40}_{-26}	0.095%	106	55 pb
MEPS	299^{+25}_{-37}	0.080%	126	80 pb
BG-Independent	BG=0			221 pb

Table B.2: The table summarises the results of the multivariate discriminant method based on range searching including the instanton-induced cross-section limits at 95% confidence level.

$60 < Q^2 < 80 \text{ GeV}^2$					
	$.2 < x' < .25$	$.25 < x' < .3$	$.3 < x' < .35$	$.35 < x' < .4$	$.4 < x' < .45$
N_{Data}	868	1230	1569	1669	2320
N_{CDM}	828^{+49}_{-88}	1196^{+71}_{-117}	1525^{+89}_{-138}	1784^{+113}_{-167}	2411^{+160}_{-211}
$\sigma_{\text{lim,CDM}}$	75 pb	85 pb	107 pb	56 pb	88 pb
N_{MEPS}	656^{+36}_{-65}	1031^{+56}_{-110}	1350^{+69}_{-132}	1533^{+75}_{-160}	2105^{+102}_{-196}
$\sigma_{\text{lim,MEPS}}$	142 pb	151 pb	183 pb	156 pb	204 pb
$\sigma_{\text{lim,BG=0}}$	447 pb	598 pb	807 pb	842 pb	1125 pb
$80 < Q^2 < 100 \text{ GeV}^2$					
	$.2 < x' < .25$	$.25 < x' < .3$	$.3 < x' < .35$	$.35 < x' < .4$	$.4 < x' < .45$
N_{Data}	534	715	808	1093	1312
N_{CDM}	520^{+38}_{-61}	704^{+44}_{-84}	769^{+51}_{-85}	1041^{+62}_{-95}	1272^{+68}_{-111}
$\sigma_{\text{lim,CDM}}$	47 pb	60 pb	75 pb	87 pb	92 pb
N_{MEPS}	409^{+29}_{-38}	518^{+40}_{-43}	607^{+37}_{-52}	860^{+52}_{-77}	1070^{+53}_{-98}
$\sigma_{\text{lim,MEPS}}$	85 pb	125 pb	136 pb	164 pb	181 pb
$\sigma_{\text{lim,BG=0}}$	280 pb	377 pb	443 pb	589 pb	721 pb
$100 < Q^2 < 120 \text{ GeV}^2$					
	$.2 < x' < .25$	$.25 < x' < .3$	$.3 < x' < .35$	$.35 < x' < .4$	$.4 < x' < .45$
N_{Data}	334	381	576	757	847
N_{CDM}	286^{+22}_{-28}	355^{+33}_{-36}	543^{+36}_{-49}	710^{+48}_{-63}	812^{+50}_{-77}
$\sigma_{\text{lim,CDM}}$	44 pb	41 pb	54 pb	63 pb	67 pb
N_{MEPS}	203.9^{+15}_{-19}	261^{+21}_{-23}	381^{+23}_{-32}	505^{+35}_{-39}	605^{+35}_{-53}
$\sigma_{\text{lim,MEPS}}$	81 pb	82 pb	130 pb	148 pb	153 pb
$\sigma_{\text{lim,BG=0}}$	183 pb	221 pb	337 pb	393 pb	451 pb
$120 < Q^2 < 140 \text{ GeV}^2$					
	$.2 < x' < .25$	$.25 < x' < .3$	$.3 < x' < .35$	$.35 < x' < .4$	$.4 < x' < .45$
N_{Data}	172	244	366	521	550
N_{CDM}	167^{+15}_{-22}	216^{+17}_{-28}	331^{+24}_{-28}	466^{+30}_{-38}	516^{+30}_{-43}
$\sigma_{\text{lim,CDM}}$	21 pb	35 pb	40 pb	52 pb	48 pb
N_{MEPS}	118^{+11}_{-14}	157^{+12}_{-16}	240^{+16}_{-21}	322^{+24}_{-27}	354^{+21}_{-30}
$\sigma_{\text{lim,MEPS}}$	40 pb	59 pb	82 pb	115 pb	122 pb
$\sigma_{\text{lim,BG=0}}$	100 pb	140 pb	205 pb	267 pb	300 pb
$140 < Q^2 < 160 \text{ GeV}^2$					
	$.2 < x' < .25$	$.25 < x' < .3$	$.3 < x' < .35$	$.35 < x' < .4$	$.4 < x' < .45$
N_{Data}	111	161	230	295	393
N_{CDM}	121^{+13}_{-14}	$159^{+14.8}_{-18}$	211^{+20}_{-25}	274^{+25}_{-28}	360^{+25}_{-32}
$\sigma_{\text{lim,CDM}}$	11 pb	18 pb	29 pb	31 pb	40 pb
N_{MEPS}	69^{+16}_{-8}	115^{+9}_{-12}	158^{+11}_{-17}	197^{+13}_{-18}	246^{+16}_{-20}
$\sigma_{\text{lim,MEPS}}$	31 pb	34 pb	50 pb	60 pb	89 pb
$\sigma_{\text{lim,BG=0}}$	66 pb	90 pb	128	149 pb	207 pb

Table B.3: The table shows limits at a confidence level of 95% of the instanton-induced cross-section in 25 bins in x' and Q^2 derived under different assumptions concerning the standard DIS background.

Bibliography

- [1] M. E. Peskin and V. Schroeder, *An Introduction to Quantum Field Theory* (Addison Wesley, 1995).
- [2] C. N. Yang and R. Mills, *Phys. Rev.* **96** (1954) 191.
- [3] A. I. Vainshtein, V. I. Zakharov, V. A. Novikov and M. A. Shifman *Sov. Phys. Usp.* **25** (1982) 195.
- [4] M. A. Shifman, *Instantons in Gauge Theories* (World Scientific, 1994) pp 1–18.
- [5] T. Schäfer and E.V. Shuryak, *Rev. Mod. Phys.* **70** (1998) 323.
- [6] A. Polyakov, *Phys. Lett.* **B59** (1975) 82.
- [7] A. Belavin, A. Polyakov, A. Schwarz and Yu. Tyupkin, *Phys. Lett.* **B59** (1975) 85.
- [8] G. 't Hooft, *Phys. Rev. Lett.* **37** (1976) 8; *Phys. Rev.* **D14** (1976) 3432; *Phys. Rev.* **D18** (1978) 2199 (Erratum).
- [9] I. Balitsky and V. Braun, *Phys. Lett.* **B314** (1993) 237.
- [10] A. Ringwald and F. Schrempp, in the proceedings of *Quarks '94*, volume 1 (Vladimir, Russia, 1994), V. Matveev *et al.*, Eds., (World Scientific, Singapore, 1995) pp 170–193; hep-ph/9411217.
- [11] S. Moch, A. Ringwald and F. Schrempp, *Nucl.Phys.* **B507** (1997) 134.
- [12] A. Ringwald and F. Schrempp, *Phys. Lett.* **B438** (1998) 217.
- [13] A. Ringwald and F. Schrempp, *Phys. Lett.* **B459** (1999) 249.
- [14] A. Ringwald and F. Schrempp, *Comp. Phys. Commun.* **132** (2000) 267.
- [15] T. Carli, J. Gerigk, A. Ringwald and F. Schrempp, in the proceedings of the workshop on *Monte Carlo Generator for HERA Physics* (Hamburg, Germany, 1999), A. Doyle, H. Jung, G. Ingelman and G. Grindhammer, Eds., 329; hep-ph/9906441.
- [16] A. Ringwald and F. Schrempp, *Phys. Lett.* **B503** (2001) 331.

- [17] A. Ringwald and F. Schrempp in the proceedings on *Workshop on New Trends in HERA Physics 1999*, Lecture Notes in Physics, Springer (Tegernsee, Germany, 1999), G. Grindhammer, B. Kniehl and G. Kramer, Eds., pp. 203; DESY 99-136; hep-ph/9909338.
- [18] F. Schrempp, in the proceedings on *New Trends in HERA Physics 2001* (Tegernsee, Germany, 2001), G. Grindhammer, B. Kniehl G. Kramer and W. Ochs, Eds., DESY-01-125; hep-ph/0109032, to be published in *J. Phys G*.
- [19] V. V. Khoze and A. Ringwald, *Phys. Lett.* **B259** (1991) 106;
J. Verbaarschot, *Nucl. Phys.* **B362** (1991) 33.
- [20] C. Bernard, *Phys. Rev.* **D19** (1979) 3013.
- [21] T. Morris, D. Ross and D. Sachradja, *Nucl. Phys.* **B255** (1985) 115.
- [22] A. Ringwald, *Nucl. Phys.* **B330** (1990) 1; O. Espinoza, *Nucl. Phys.* **B343** (1990) 310.
- [23] D. A. Smith and M. J. Teper, UKQCD Collaboration, *Phys. Rev.* **D58** (1998) 014505.
- [24] A. Ringwald and F. Schrempp, in the proceedings of the *8th Int. Workshop on Deep-inelastic scattering, DIS 2000* (Liverpool, England, 2000), J. Dainton, J. A. Gracey and T. Greenshaw, Eds., pp. 318; hep-ph/00063215.
- [25] Particle Data Group, C. Caso *et al.*, *Eur. Phys. J.* **C3** (1998) 1.
- [26] D. R. C. Kelly *et al.*, in the proceedings of the *1995 Particle Accelerator Conference PAC95*, (Hamburg, Germany, 1995).
- [27] http://www-h1.desy.de/h1/www/h1det/lumi/summary_tables/summary.html
- [28] I. Abt *et al.* [H1 Collaboration], *Nucl. Instr. and Meth.* **A386** (1997) 310.
- [29] I. Abt *et al.* [H1 Collaboration], *Nucl. Instr. and Meth.* **A386** (1997) 348.
- [30] D. Pitzl *et al.* [H1 CST Group], *Nucl. Instr. and Meth.* **A545** (2000) 334;
E. Peppel, *Nucl. Instr. and Meth.* **A409** (1998) 201;
M. Keller *et al.* *Nucl. Instr. and Meth.* **A409** (1998) 604;
M. Fleischer, *DESY-Report* 98-005 (1997);
R. Maraček *et al.*, Upgrade of the H1 LAr calorimeter trigger, in the proceedings of the *Calorimetry in High Energy Physics Conference — CALOR 99*, (Lisbon, Portugal, 1999) 583.
- [31] J. Bürger *et al.*, *Nucl. Instr. and Meth.* **A279** (1989) 217.
- [32] S. Egli *et al.*, *Nucl. Instr. and Meth.* **A283** (1989) 487.
- [33] H. Bärwolff *et al.*, *Nucl. Instr. and Meth.* **A283** (198) 467.

- [34] J. Prell, *Dissertation: Entwicklung des Steuer- und Auslesemoduls für die Siliziumstreifendetektoren des H1-Detektors*, University of Hamburg (1992), DESY FH1-96-02;
M. zur Nedden, *Dissertation: Photoproduction of open charm in ep-collisions at HERA*, University of Zurich (1998).
- [35] P. Marage *et al.*, *Nucl. Phys. Proc. Suppl.* **16** (1990) 518.
- [36] K. Müller *et al.*, *Nucl. Instr. and Meth.* **A312** (1992) 457.
- [37] S. Burke *et al.*, *Nucl. Instr. and Meth.* **A373** (1992) 457.
- [38] G. A. Beck *et al.*, *Nucl. Instr. and Meth.* **A283** (1989) 471.
- [39] B. Schwab, *Dissertation: Das Rückwärtsdriftkammersystem des H1-Experiments*, University of Heidelberg (1996).
- [40] B. Andrieu *et al.* [H1 Calorimeter Group Collaboration], *Nucl. Instr. and Meth.* **A336** (1993) 460.
- [41] R. Wigmans, *Nucl. Instr. and Meth.* **A259** 389.
- [42] B. Andrieu *et al.* [H1 Calorimeter Group Collaboration], *Nucl. Instr. and Meth.* **A350** (1994) 57.
- [43] B. Andrieu *et al.* [H1 Calorimeter Group Collaboration], *Nucl. Instr. and Meth.* **A336** (1993) 499.
- [44] H.-P. Wellisch *et al.*, *MPI-Report MPI-PhE/94-03* (1994).
- [45] R. D. Appuhn *et al.* [H1 SpaCal Group Collaboration], *Nucl. Instr. and Meth.* **A386** (1997) 397.
- [46] R. D. Appuhn *et al.* [H1 SpaCal Group Collaboration], *Nucl. Instr. and Meth.* **A374** (1996) 149.
- [47] R. D. Appuhn *et al.* [H1 SpaCal Group Collaboration], *DESY-Report 95-250* (1995).
- [48] H. Bethe and W. Heitler, *Proc. Roy. Soc.* **A146** (1934) 83.
- [49] N. Gogitidze and S. Levonian, *H1 Internal Note H1-01/96-471* (1996).
- [50] E. Elsen, *H1 internal note H1-09/92-239* (1992).
- [51] J. Köhne *et al.*, *Nucl. Instr. and Meth.* **A389** (1997) 128.
- [52] J. C. Bizot *et al.*, *H1 Internal Note H1-02/92-212* (1992);
H1 Internal Note H1-09/92-240 (1992).
C. Beigbeider *et al.*, *H1 Internal Note H1-07/98-547* (1998).
- [53] E. Barrelet *et al.*, *H1 Internal Note H1-12/88-100* (1988).

- [54] R. Brause, *Neuronale Netze* (Teubner, Stuttgart, 1991).
- [55] C. Peterson and T. Rognvaldsson, *An Introduction to Artificial Neural Networks*, Lectures given at the 1991 CERN School of Computing, University of Lund preprint LU TP 91–23 (1991).
- [56] L. Holmström, S. R. Sain and H. E. Miettinen, *Comp. Phys. Comm.* **88** (1995) 195.
- [57] G. Cybenko, *Math. Contr. Sign. Syst.* **2** (1998) 303.
- [58] R. Brun and F. Rademakers *Nucl. Inst. and Meth. in Phys. Res.* **A389** (1997) 81; see also <http://root.cern.ch/>.
- [59] J. L. Bentley, *Comm. of the ACM*, **18**, (1975) 9.
- [60] J. L. Bentley and J. H. Friedman, *Computing Surveys* **11** (1979) 4.
- [61] R. Sedgewick, *Algorithmen in C++* (Addison-Wesley, Bonn, 1992) pp. 427.
- [62] H. Jung, *Comp. Phys. Comm.* **86** (1995) 147.
- [63] L. Lönnblad, *Comp. Phys. Comm.* **71** (1992) 15.
- [64] G. Gustafson and U. Petterson, *Nucl. Phys.* **B306** (1988) 741; B. Andersson and G. Gustafson, *Phys. Lett.* **B241** (1988) 604; *Z. Phys.* **C49** (1991) 79; *Nucl. Phys.* **B392** (1993) 251; B. Andersson *et al.*, *Z. Phys.* **C43** (1989) 625; G. Gustafson, *Phys. Lett.* **B175** (1986) 453.
- [65] B. Andersson, G. Gustafson, G. Ingelman and T. Sjöstrand, *Phys. Rep.* **97** (1983) 33; B. Andersson, G. Gustafson and B. Söderberg, *Z. Phys.* **C20** (1983) 317.
- [66] B. Webber, *Nucl. Phys.* **B238** (1984) 492.
- [67] G. Altarelli and G. Parisi, *Nucl. Phys.* **B126** (1977) 298; V. N. Gribov and L. N. Lipatov, *Sov. J. Nucl. Phys.* **15** (1972) 438.
- [68] G. Ingelman, in the proceedings of the *1991 Physics at HERA Workshop*, Eds. W. Buchmüller and G. Ingelman, volume 3, (Hamburg, Germany, 1992), pp 1366.
- [69] H. L. Lai *et al.*, *Phys. Rev.* **D55** (1997) 1280.
- [70] C. Adloff *et al.* [H1 Collaboration], *Eur. Phys. J.* **C21** (2001) 33.
- [71] T. Carli, H. Küster and M. Lindström, *H1 internal software note 58-5/98*
- [72] G. Marchesini *et al.*, *Comp. Phys. Commun.* **67** (1992) 465.
- [73] T. Sjöstrand, *Comp. Phys. Commun.* **82** (1994) 74.
- [74] T. Sjöstrand, *Lectures at the XVIII International Meeting on Fundamental Physics, CERN-TH 590290* (1990).

- [75] D. Amato and G. Veneziano, *Phys. Lett.* **B83** (1997) 87.
- [76] J. Meyer, *H1 Software Note* 03-11/89 (1991).
- [77] CERN Application Software Group, *CERN Program Library* W5013.
- [78] S. Eichenberger *et al.*, *Nucl. Instr. and Meth.* **A323** (1992) 532.
- [79] T. Wolff *et al.*, *Nucl. Instr. and Meth.* **A323** (1992) 537.
- [80] R. Mohr, *Dissertation: Messung von 3-Jet-Ereignissen in tief- unelastischer e-p-Streuung mit dem H1-Detektor bei HERA*, University of Hamburg (2000), MPI-PhE/00-06.
- [81] S. Bentvelsen *et al.*, in the proceedings of the *1991 Physics at HERA Workshop*, Eds. W. Buchmüller and G. Ingelman, volume 1, (Hamburg, Germany, 1992), pp 23–40.
- [82] G. Bernardi and W. Hildesheim *et al.*, in the proceedings of the *Physics at HERA Workshop*, Eds. W. Buchmüller and G. Ingelman, volume 1 (DESY, Hamburg, 1992), pp 79–99.
- [83] C. Adloff *et al.* [H1 Collaboration], *Z. Phys.* **C74** (1997) 221.
- [84] J. Gerigk, *Diploma Thesis: QCD-Instanton-induzierte Prozesse in tiefunelastischer $e^\pm p$ -Streuung*, University of Hamburg (1998); MPI-PhE/98-20.
- [85] S. Aid *et al.* [H1 Collaboration], *Phys. Lett.* **B356** (1995) 118.
- [86] G. White, *Dissertation: Tests of Perturbative and Non-Perturbative QCD from Identified Proton, Kaon and Pion Studies in Deep Inelastic Scattering ep Interactions at HERA*, University of Lancaster (2000).
- [87] D. Milstead, *Dissertation: The production of neutral kaons and lambdas in deep-inelastic scattering at H1 and an upper limit on the production of instantons*, University of Liverpool (1996).
- [88] B. Koblitz, in the proceedings on *New Trends in HERA Physics* (Tegernsee, Germany, 2001), G. Grindhammer, B. Kniehl, G. Kramer and W. Ochs, Eds.; hep-ex/0110042, to be published in *J. Phys.* **G**.
- [89] L. del Pozo, *Dissertation*, University of Cambridge, **RALT-002** (1993).
- [90] M. Seymour, *Z. Phys.* **C62** (1994) 127.
- [91] M. Gibbs *et al.*, in the proceedings of *Future Physics at HERA* (Hamburg, Germany, 1996), G. Ingelman, A. deRoeck and R. Klanner, Eds., vol 1, p. 509
- [92] C. Adloff *et al.* [H1 Collaboration], *Eur. Phys. J.* **C19** (2001) 289.
- [93] C. Adloff *et al.* [H1 Collaboration], *Phys. Lett.* **B515** (2001) 17.

- [94] N. Brook *et al.*, in the proceedings of the workshop on *Monte Carlo Generators for HERA Physics* (Hamburg, Germany, 1999), A. Doyle, G. Grindhammer, G. Ingelman and H. Jung, Eds., pp 10; hep-ex/9912053.
- [95] T. Schörner-Sardenius, *Dissertation: Messung inklusiver Jet-Wirkungsquerschnitte in tiefunelastischer ep-Streuung mit dem H1-Detektor bei HERA*, Ludwig-Maximilians-Universität Munich (2001); MPI-PhE/2001-10.
- [96] B. Heinemann, *Dissertation: Measurement of Charged Current and Neutral Current Cross Sections in Positron-Proton Collisions at $\sqrt{s}=300$ GeV*, University of Hamburg (1999);
W. Erdmann, *Diploma Thesis*, University of Zurich.
- [97] C. Adloff *et al.* [H1 Collaboration], *Eur. Phys. J.* **C13** (2000) 609.
- [98] O. Helene, *Nucl. Instr. and Meth.* **212** (1983) 319.
- [99] C. Adloff *et al.* [H1 Collaboration], *Z. Phys.* **C74** (1997) 191.
- [100] T. Carli and B. Koblitz, in the proceedings of *Advanced Comp. Analysis Techniques in Physics Research* (Batavia, USA, 2000), P. Bath and M. Kasemann, Eds., pp 110; hep-ph/0011224
- [101] G. Fox and St. Wolfram, *Nucl. Phys.* **B149** (1979) 413.
- [102] S. I. Bitjukov and N. V. Krasnikov *physics/9811025*.

List of Figures

1.1	Vertices of QCD	9
1.2	Double Well and Double Hump Potential	10
1.3	Instanton Solution in Imaginary Time	11
1.4	Lagrange Density of an Instanton	13
1.5	Topology of the QCD Vacuum	14
1.6	Deep-Inelastic Scattering	15
1.7	DIS Processes at Tree Level	17
1.8	QCD Instanton-Induced Process in DIS	18
1.9	Confrontation of Instanton-Perturbation Theory with Lattice Calculations	21
1.10	Cross-Section of the Instanton Subprocess	22
2.1	The HERA Collider	24
2.2	H1 Coordinate System	25
2.3	The H1 Detector	26
2.4	The H1 Tracking System	27
2.5	The H1 Liquid Argon Calorimeter	29
2.6	The Backward Calorimeter SpaCal	30
2.7	The H1 Luminosity System	31
2.8	The H1 Trigger System	32
3.1	Classification by Cuts on Observables	37
3.2	Neural Networks	38
3.3	Neural Network Performance	40
3.4	How Binary Trees store Events	43
3.5	Dependence of Separation on Box-Size	44
3.6	Classification with a Discriminant Based on Range Searching	45
4.1	Matrix Element plus Parton Shower	47
4.2	The Colour Dipole Model	48
4.3	The Lund String Model	49
4.4	Cluster Fragmentation	50
5.1	Trigger Efficiencies	55
5.2	Selected Kinematic Region	56
5.3	Description of $E - p_z$ Before and After Reweighting	57
5.4	Description of Track Distributions by Standard DIS Models	60
5.5	Description of Electron Kinematics	61

5.6	Description of $E - p_z$ and $p_{t,\text{had}}/p_{t,\text{el}}$	63
6.1	The Topology of an I-induced Event	65
6.2	Detector Simulation of a QCDINS Generated I-Event	66
6.3	Description of the E_t Distribution	68
6.4	Distribution of ξ	70
6.5	Visualisation of the Shape Variable Δ	72
6.6	Characteristic Instanton Observables Before Cuts	73
6.7	Characteristic Instanton Observables (Logarithmic Scale)	74
6.8	QCDINS with JETSET Hadronization	76
6.9	Description of $E - p_z$ and $p_{t,\text{had}}/p_{t,\text{el}}$	78
6.10	Systematic Effects on the Sphericity	80
6.11	Systematic Effects on $Q_{\text{rec}}'^2$	81
6.12	Systematic Effects on the Multiplicity	82
6.13	Model Dependencies	84
6.14	The Observables after Cuts to Enrich the Instanton Contribution	87
6.15	Shape Normalised Distribution of the Discriminant	89
6.16	Systematic Effects on the Discriminant	90
6.17	Observable Distributions After Cut on Discriminant	92
6.18	Results of the Discriminant Search	93
6.19	Distribution of MEPS plus the Fitted Fraction of I-Events	94
6.20	Selected Event 1	95
6.21	Selected Event 2	96
6.22	Limits on Instanton Cross-Section in Bins of x' and Q'^2	99
6.23	Comparison of Instanton Cross-Section Limits with Lattice Data	102
7.1	Reconstruction of x' and Q'^2	104
7.2	Jet-Selection Scheme	106
7.3	Event: Jet Punches Through Backward Part of Calorimeter	107
7.4	Enhanced Reconstruction of x' and Q'^2 with Improved Jet Selection	108
8.1	The Five Discriminating Variables at High Q^2	112
8.2	Discriminant Distribution of Signal and Background	113
8.3	The Distribution of $E_{t,\text{Jet}}$	114
8.4	Result of High Q^2 Study	115
8.5	Reconstruction of x' and Q'^2	116
8.6	Dependence of Separation Power on the Box-Size (High Q^2 Study)	117
8.7	Training and Performance of the Neural Network	118
8.8	Output Distributions of Neural Network	118

List of Tables

6.1	Results of the Cut-Based Method	85
6.2	Systematic Errors of Cut-Based Method	85
6.3	Results of the Discriminant Method	89
6.4	Systematic Uncertainties of the Discriminant Method	91
6.5	Limits on the Instanton Cross-Section in the Fiducial Region	98
7.1	Comparison of the Reconstruction of x' and Q'^2	107
B.1	Summary of the Results of the Combinatorial Cut Method	126
B.2	Summary of the Results of the Discriminant Method	126
B.3	Limits on the Instanton Cross-Section in bins of x' and Q'^2	127

Acknowledgements

The results presented in this thesis would not have been obtained without the collaboration of many people here at DESY and at the MPI in Munich. First, I would like to express my gratitude towards my fellow instanton hunters Tancredi Carli and Stanisław ‘Staszek’ Mikocki for three years of fruitful and enjoyable collaboration. Moreover, I am very much indebted to Tancredi for his guidance through the world of physics at H1 and the supervision of my thesis.

For many enlightening and delighting discussions on the theory of instantons I would like to thank A. Ringwald and F. Schrempp. In many hours they finally managed to give me a hint on what instantons really are.

V. Blobel I would like to thank for taking over the responsibility to supervise my thesis and for providing many helpful hints, especially for pointing me to Sedgewick’s book on algorithms.

Many people in Hamburg and at the MPI in Munich have made me feel “at home” in the MPI group here in Hamburg. They are G. Buschhorn, A. Dubak, G. Grindhammer, L. Janauschek, Chr. Kiesling, K. Preuss, B. Reisert, Chr. Risler, S. Schmidt, T. Schörner-Sardenius, E. Tzamariudaki and M. zur Nedden. In particular, I would like to thank Christiane, Sebastian, Katerina, Martin and Günter for many funny hours in our offices and at lunch.

For their careful proof-reading I would like to thank V. Blobel, T. Carli, G. Grindhammer, R. Klanner, S. Mikocki, F. Schrempp and P. D. Thompson. Of course, any remaining mistakes are entirely attributed to me.

Finally, I would like to thank my parents for supporting me during the time I studied and for stimulating my interest in natural sciences in the first place. And eventually, I owe Susanne a big and loving “thank you” for suffering with me through the time when this thesis was written.